ADVANCED LECTURES

SATELLITE METEOROLOGY

Lecture 1. (Morgan)

AN INTRODUCTION TO SATELLITE METEOROLOGY

1. Introduction

The purpose of this series of lectures is to discuss ways in which satellite techniques can be applied to meteorology. The aim is to provide an appreciation of potential applications of satellite data, including their strengths and shortcomings.

Satellite meteorology is a young subject. The first meteorological observations were made from a satellite only 25 years ago. The subject is already wide ranging. Satellites are the basic vehicle for space research and have become the major source of observations of the upper atmosphere. This series of lectures will concentrate on applications of satellite techniques to studies of the lower atmosphere, the realm of operational meteorology. Useful review papers on satellite meteorology can be found in the list of references.

Before describing the satellite techniques it is of interest to consider the basic motivation for using observation platforms in space. Typical meteorological satellites orbit the earth at elevations of either 36000 km or about 850 km, and yet we expect them to give us useful quantitative information about surface features and about a region of the atmosphere (the troposphere) extending only 10 km from the surface of the earth. At first glance successful remote sensing from this altitude would appear to be a highly unlikely undertaking, so why try?

The imaging capability of meteorological satellites provides part of the justification. Cloud images provide invaluable diagnostic information which assists in the analysis of meteorological features. This benefit can be extended by the use of time lapse image sequences of the type which you have just seen, and use of such material has transformed our understanding of atmospheric processes. However, this information is not quantitative and not of obvious use for numerical models. These models need precise measurements of atmospheric parameters at frequent time intervals, for many levels and at close intervals over the surface of the earth. The spacing of the observations depends on the nature of the model, but for synoptic scale global modelling the Global Atmospheric Research Programme (GARP) planning documents suggest the observational requirements summarised in Table 1.

TABLE 1

Parameters		Accuracies
Surface Pressure	p_s	1 mb
Horizontal wind	V	3 m sec^{-1}
Temperature	T	1°C
Relative humidity	r	5%
Horizontal resolution	500 km	
Vertical resolution	1 km	
Time resolution	6 hr	
Representation	100 km (horizontal), 0.5 km (vertical), 1 hr (time)	

This requirement could be met by an adequate network of about 5,000 conventional stations, preferably regularly distributed all over the globe, each measuring the pressure at the surface as well as the wind, temperature, and humidity at many levels, from the surface to 50 mb, 2 to 4 times each day. The cost of such a network would be of the order of $\$10^{10}$ per year. If the network could be implemented by some miracle of international co-operation, and if the UK financial contribution would be as low as 1% of the global programme cost, then this would still exceed the present total annual budget of the Meteorological Office by a substantial margin.

By contrast, the entire globe can be observed by a system of 7 meteorological satellites. A global programme to launch 2 new satellites each year and to operate the total system could cost less than $\$2 \times 10^8$ per year, excluding development costs, and a UK financial contribution of even 10% to this global system would amount to a more realistic 25% of the present Meteorological Office budget.

Similar arguments can be advanced concerning the denser observational networks required for regional and local scale forecasting. Additional conventional stations will be needed to satisfy these observational requirements whereas the same global system of satellites could, if appropriately specified, also provide the increased density of observations without additional cost.

Therefore the satellites, although individually expensive, provide more observations per £ and hence the main motivation for our interest in quantitative uses of meteorological satellites is financial. They appear to offer cost effective solutions to the problem of acquisition of observational data with useful resolution and accuracy. It is the purpose of this series of lectures to demonstrate to what extent satellites are able to satisfy the general observational requirements.

2. General

Most conventional meteorological observations are made by in-situ techniques, in which the measuring instrument is in direct contact with the atmosphere. Instruments may be carried aloft by a balloon to observe the troposphere and stratosphere. Rockets can carry instruments to higher levels. A satellite can provide measurements over greater horizontal distances and for longer periods in a single rocket. But satellites cannot remain in orbit at heights much below 150 km, so in-situ techniques cannot be used from satellites to study the atmosphere below that height. However, satellites can nevertheless play a role, through provision of reliable rapid and economic telecommunication channels for collection of data from in-situ sensors on the ground, on buoys, on ships and on aircraft. They can also be used to locate a sensor from its transmissions using Doppler techniques (useful for drifting buoys).

There are ground based instruments which make observations at a distance, for example, radar provides information on the spatial distribution of rain by detecting back-scattering of an emitted pulse of rf radiation from rain drops. Remote sensing techniques, exploiting the processes of scattering, absorption and emission of radiation, are the basic tools of satellite meteorology. To date operational satellite techniques have been confined to exploiting natural radiation (ie sunlight, and thermal black body emission). Instruments have been flown experimentally which generate microwave radiation to illuminate the scene and detect the back-scattered radiation. Sensors using natural and artifical radiation are referred to as passive and active respectively.

The following lectures will describe examples of these remote sensing techniques and go into details of the theory of the methods. At this point it may be useful to provide a reminder of some of the terminology and basic laws of radiation.

3. Radiation

a. Units of wavelength and frequency

Radiation may be described by its wavelength (λ) or frequency (ν), which are related by:

$$C = \nu\lambda$$

where C is the velocity of light, 3×10^8 ms^{-1}. In the visible and infra-red spectral regions, radiation is normally referred to by its wavelength, in nanometers (nm = 10^{-9} m) or microns (10^{-6} m). In the infra-red wavelength is often expressed as the number of wavelengths per cm, the wavenumber, in units of cm^{-1}. Thus

$$1000 \text{ nm} \equiv 1 \text{ micron} \equiv 10000 \text{ cm}^{-1}$$
$$10 \text{ micron} \equiv 1000 \text{ cm}^{-1}$$

In the microwave region it is more common to refer to radiation by its frequency. Thus a frequency of 30 GHz (1 gigahertz = 10^9 cps) corresponds to a wavelength of approximately 1 cm, and 180 GHz to 1.7 mm.

b) Emission: some definitions.

A 'black body' absorbs all radiation which falls upon it. In general a body absorbs only a fraction of incident radiation, known as the absorptivity; this is wavelength dependent. Similarly, the efficiency for emission is known as the emissivity. At a given wavelength:

$$\text{Emissivity} = \text{Absorptivity} \qquad \text{(KIRCHHOFF'S LAW)}$$

Power emitted per unit area, steradian and wavenumber is known as radiance.

c) Emission from a blackbody.

Flux (ie energy per unit area) per unit wavelength interval emitted by a blackbody at temperature T at wavelength λ is given by:

$$B(\lambda) = \frac{2\pi hc^2\lambda^{-5}}{\exp(hc/k\lambda T)-1}$$

$B(\lambda)$ and its equivalent in frequency units, $B(\nu)$, are known as the Planck Function.

$B(\lambda)$ peaks at wavelength λm given by:

$$\lambda m.T = 0.29 \text{ deg. cm} \qquad \text{(WIEN'S LAW)}$$

For the Sun: T = 6000 K; λm = 0.48 micron
For the Earth T = 290 K; λm = 10 micron

Total energy emitted by a blackbody:

$$= \int B(\lambda)\, d\lambda = \sigma T^4 \qquad \sigma, \text{ STEFAN'S CONSTANT}$$

B is proportional to T at microwave and far infra-red wavelengths. Typical dependence of B on T for λ at or below λm is shown in Figure 1.

d) Atmospheric absorption.

Atmospheric absorption in the infra-red is dominated by "absorption bands" of water, carbon dioxide, ozone etc. Studies of radiation within these bands enables us to determine characteristics of the atmosphere; its temperature and the concentration of the absorber. However there are regions of the spectrum where absorption is low, providing the possibility for a satellite sensor to view the surface and to determine its temperature or other characteristics. Such spectral regions are called "windows". There is a particularly important window near the peak of the earth/atmosphere emission curve, around 11 microns.

4. Satellite orbits

An artificial satellite moves in an elliptical orbit, with the earth's centre at one focus of the ellipse. The size, shape and orientation of the orbit are defined by a set of parameters known as orbital elements. For various practical reasons meteorological satellites are in circular orbits (or as nearly so as possible). The angle between the orbital plane and the earth's equatorial plane is termed the inclination, i (see Figure 2). The point at which the orbit crosses the equator with the satellite going north is called the ascending node. The orbital period, P is given by:

$$P = 2\pi \sqrt{a^3/\mu}$$

where a is the semi-major axis of the orbit (in practice the radius, ie the earth's mean radius plus the satellite's height above the surface) and $\mu = 3.986\ 10^5\ km^3\ s^{-2}$.

The orbital period of a satellite at a height of 900 km is about 102 minutes.

For an orbital height of 36000 km (ie a = 42400 km), P = 24 hours. If the orbital inclination is zero the satellite is travelling vertically above the equator. The angle of velocity of a satellite at this height is equal to that of the earth and the satellite remains above the same point on the equator; the satellite appears stationary relative to an observer on the earth's surface. Such an orbit is termed geostationary. In practice, the inclination of such an orbit will be non-zero (even if inserted into an i = 0 orbit; the inclination will change as a result of the influence of the moon). In this case the more general term, geosynchronous orbit, applies and the satellite will appear to move in the sky through a "narrow figure of 8" pattern, bounded in latitude by the angles of i and -i, each day. The inclination increases in a regular way because of the influence of the moon, and the satellite will also tend to slide down any

geopotential slope caused by non-uniformities in the earth's gravitational field, hence the required orbit must be maintained by active station keeping, using gas discharge thrusters to adjust the orbit several times each year.

In Figure 2 the angle Ω defines the position of the ascending node with respect to a conventional fixed reference direction (the intersection of the equator and ecliptic planes; "the first point in Aries"). King-Hele (1964) shows that, contrary to simple theory, Ω changes at a rate given approximately by:

$$\dot{\Omega} = -10.0\ (R/a)^{3.5} \cos i \text{ deg/day}$$

where R is the earth's equatorial radius. This effect is caused by the oblateness of the earth. Thus, unless $i = 90^{0}$ (a true polar-orbit), the plane of the orbit precesses about the earth's axis (see Figure 3).

To achieve good quality visible imagery from near-earth orbit, it is desirable to be able to select the local solar time at which observations are made and to keep this constant (or at least to avoid substantial long-term changes) throughout the satellite's life. This means that the orbital plane of a satellite should remain fixed in orientation to the earth-sun direction. The latter rotates in the ecliptic plane, through 360/year (approximately 1° per day). If i is less than 90°, the precession of the orbital plane adds to this relative rotation. However, if i is increased beyond 90° to the point where $\dot{\Omega} = 1°/\text{day}$, then precession of a plane will, over a year, balance out the effect of the motion of the earth around the sun. Such an orbit is termed sun-synchronous. For an orbital height of 850 km, the necessary value of i is about 99. Thus the orbit is still near-polar and by using instruments which scan either side of the satellite track one may obtain observations from pole to pole.

Satellite orbital height controls the radius of the contact circle for direct reception of data transmitted in real time from the satellite and the width of the swath which can be observed by a satellite sensor. Both are improved by increasing the satellite height. However, whilst greater orbital height has its advantages there are practical difficulties. Satellites in orbit above 1100 km encounter a much increased flux of charged particles (which can degrade performance of solar cells and other materials). Increases in satellite height also require more sensitive instruments to maintain the same ground resolutions.

5. General Classes of Meteorological Satellites

There are two major classes of satellites, distinguished by their orbits: geosynchronous and sun-synchronous near polar.

THE TWO MAJOR CLASSES OF WEATHER SATELLITE

	POLAR-ORBITER	GEOSTATIONARY
Orbit and consequences	height " 850 km sun-synchronous fixed local solar time	Height 36000 km equatorial plane fixed sub-satellite point (ssp).
Coverage	Global	Limited (70° of ssp).
Frequency	twice/day	twice/hour.
Special	- high resolution IR measurements easier.	- winds from motion of clouds.
	- active location of buoys and balloons.	- warnings from remote sensors

A geostationary satellite can produce an image by optically scanning the earth's disk, within 25 minutes; so observations are essentially simultaneous over its complete zone of coverage. Thus these observations are readily compatible with normal synoptic conventional observations. This is not to say that there are no difficulties. Products dependent on visible imagery cannot be available simultaneously from all geostationary satellites because it is always night time over half of the globe's surface.

The low orbiting satellite makes use of its orbital motion to build up its coverage of observations, taking 12 hours to obtain full global coverage. Its observations are asynoptic. Two satellites working together in orbits about 6 hours apart can dramatically increase the number of the observations of a particular area within the acceptance interval of an analysis. This is the approach adopted in the current US series, TIROS-N.

6. Current operational meteorological satellite series

There are 3 types of low orbiting meteorological satellite in operation. These are:-

TIROS-N: the US civil satellites. The system comprises two satellites, currently NOAA-7 and NOAA-8. They provide image services and carry instruments for temperature sounding as well as for data collection and data platform location. Some of the products of the system are provided on the GTS.

DMSP: the US military satellites. These provide image and (less sophisticated) sounding data. Their real time transmissions are encrypted.

METEOR-2: the USSR series; image and sounding services, but lower quality infra-red imagery. No products are made available on the GTS.

Complete coverage of the extra-polar regions requires 5 geosynchronous satellites. The current position is:

GOES: the US satellites. Two satellites provide imagery from longitudes 75 W and 135 W. A third is used for dissemination of imagery (located at 105 W). There are other satellites (some only partially workable) available as spares.

GMS: The Japanese satellite. A US designed and launched satellite operating at 140 E.

METEOSAT: The ESA satellite. METEOSAT-1 has a fault, only the data collection system can be operated, and is maintained at 10 E. METEOSAT-2 has a complimentary fault, the data collection system cannot be used, but all other functions are operational and this satellite is maintained at 0° longitude.

There are therefore effectively 4 geosynchronous satellites presently in operation, and there is no data coverage over the Indian Ocean area. This area of the world was covered temporarily during the FGGE year (1978), by a US satellite which was operated by ESA. The USSR has long term plans to position a satellite at some point over the Indian Ocean, but no precise launch data is yet available. The Indian Space Authorities have launched a general purpose satellite over the Indian Peninsula, INSAT, this is primarily a communication satellite, but does have some imaging capability, and is regarded as a national resource rather than part of a global system.

Further information is given in the references listed at the end of this lecture.

7. What satellite products are operationally available?

a. Qualitative products

Images from satellites can be used to locate features (cloud bands, fog patches, snow and ice cover) and to estimate the vigour of synoptic systems. Polar orbiting satellites transmit imagery in real time direct from the satellite. Given suitable reception and display facilities the forecaster can have access to image data over an area of radius about 2500 km. Such imagery is available 4 times per day, that is during daylight hours and at night from each of the 2 satellites. Reception of data from a geostationary satellite provides more frequent pictures over a wider area. In either case images can be available within 10-20 minutes of the time of observation, the delay being associated with addition of geographical location information (for example grids or coastlines).

b. Quantitative products

Images, supplemented by observations of radiance in a range of spectral channels, particularly in absorption bands of carbon dioxide, are used to generate a range of quantitative products. Principle amongst these are:

- Winds, derived from the motion of clouds as seen from the frequent images of geostationary satellites. Each satellite operator is providing about 1,000 winds per day within the latitude belt 50 N to 50 S.

- Temperature profiles derived from radiances. NOAA produce and distribute about 8000 atmospheric profiles per day, on a 300 km spacing. The HERMES system also produces about 7000 atmospheric profiles per day at about a 100 km spacing, from the same satellites.

Other products now regularly available include sea surface temperatures, cloud and humidity information.

8. Conclusion

Satellites provide data which has operational applications. The following lectures will explain the sources of the data, the means by which products are generated and an indication of their quality. Two of the lectures will discuss techniques which are still at the research and development stage.

REFERENCES

Orbit Theory

D King-Hele "Theory of satellite orbits in an atmosphere" London, Butterworths, 1964.

Information on satellite systems and products

BASIC "WWW GOS-satellite sub-system: Information on meteorological satellite programmes operated by members and organisations". WMO No 411 (1975, but updated annually).

TIROS-N "The TIROS-N/NOAA A-G satellite series", A Schwalb, NOAA Technical Memorandum NESS 95, (1978).

"Data extraction and calibration of TIROS-N/NOAA radiometers", L Lauritson, G L Nelson and F W Porto, NOAA Tech Memo NESS 107, (1979).

DMSP "Defence meteorological satellite program (DMSP) Users Guide", Washington Air Weather Service, Technical Report 74-250 (1974).

"The Defence Meteorological Satellite Program", D A Nichols, Optical Engineering 14 273-278 (1975).

METEOR "Soviet Meteor satellite imagery", B C Diesen III and D L Reinke, Bull. Amer Met Soc (1978) 59, 804-807.

GOES "Central processing and analysis of geostationary satellite data" C F Bristor, NOAA Tech Memo NESS 64 (1975).

"Geostationary operational environmental satellite/data collection system", NOAA Technical Report NESS 78 (1979).

"TIROS-N series Direct Readout Services Users Guide". NOAA-NESS (1982).

"The WEFAX User's Guide" NOAA-NESS (1981).

METEOSAT "Introduction to the Meteosat system", ESA Darmstadt (1981).

"The METEOSAT System Guide", ESA Darmstadt (various dates).

GMS "The GMS users' guide", issue 1, Tokyo Meteorological Satellite Centre, (1980).

T-N/GOES "National Environmental Satellite Service. Catalogue of Products, 3rd edition." D C Dismachek, A L Booth and J A Leese, NOAA Tech Memo NESS 109, (1980).

A LIST OF ACRONYMS, ABBREVIATIONS etc IS AVAILABLE.

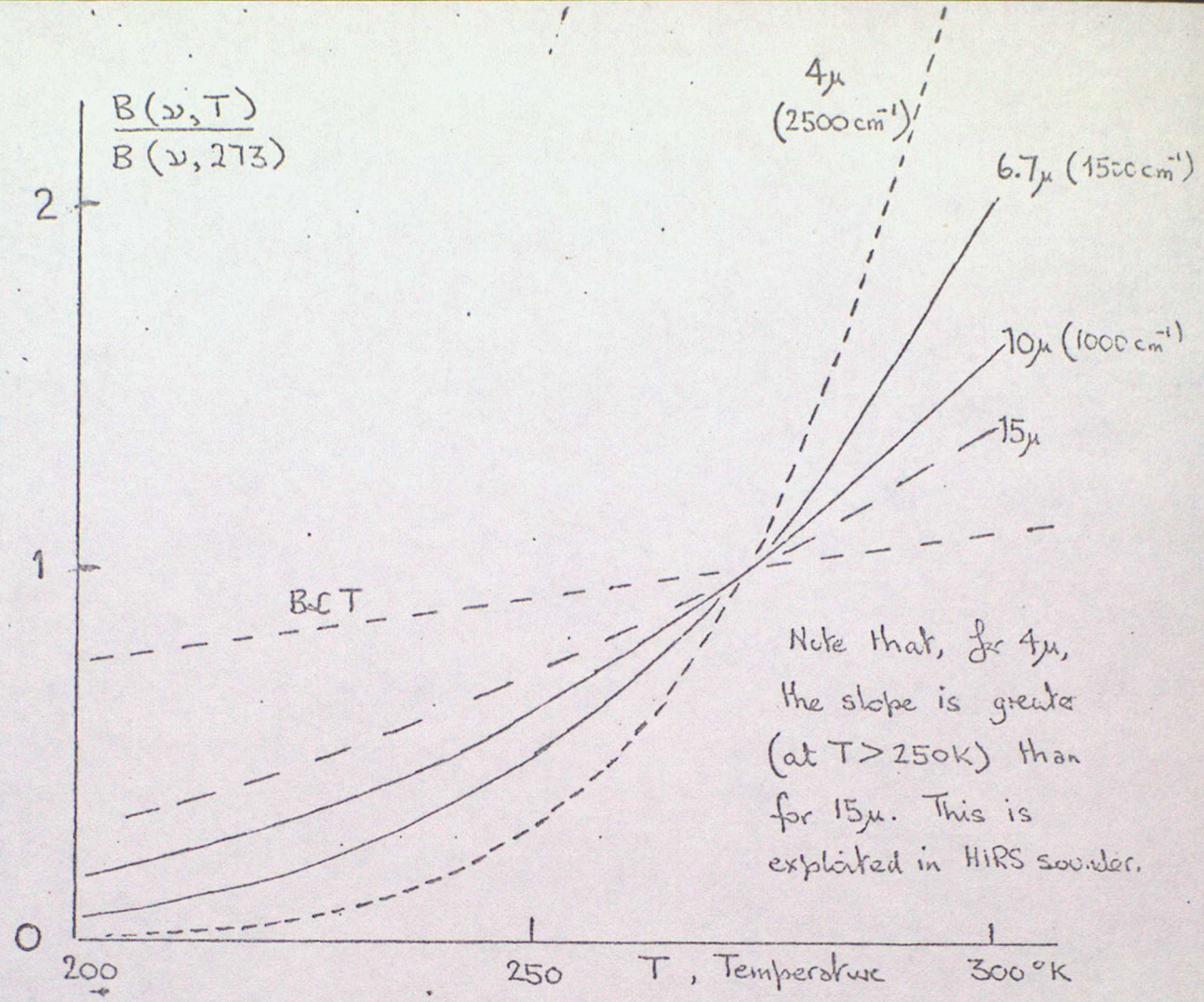

Figure 1. Temperature dependence of Planck function.

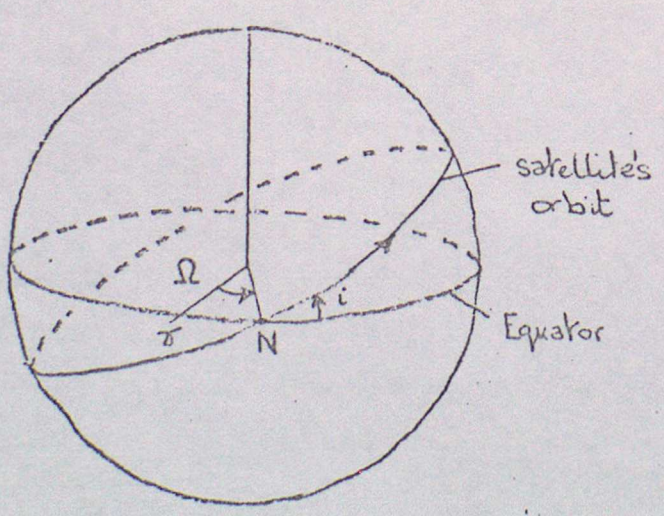

Figure 2. Satellite orbit.

N, ascending node
i, inclination of orbit
γ, first point in Aries
Ω, Right ascension of node.

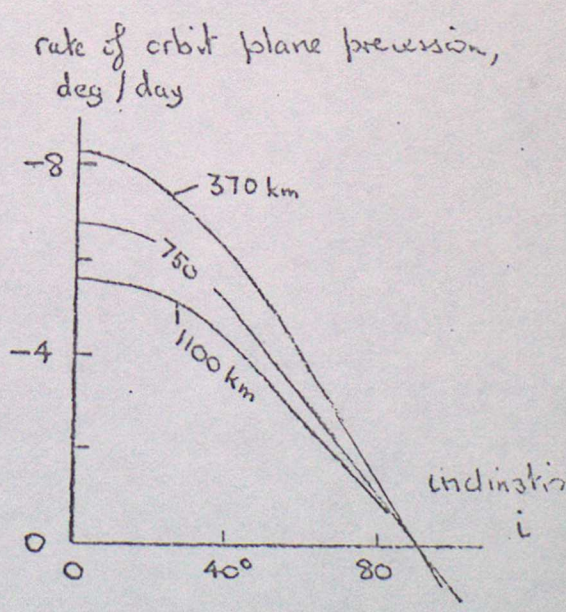

Figure 3. Precession of orbit plane for three orbit heights.

ADVANCED LECTURES - SATELLITE METEOROLOGY - 1984

LECTURE 2: RADIATIVE TRANSFER THEORY APPLIED TO SATELLITE MEASUREMENTS OF RADIATION

by J.R.Eyre

1. Introduction

In this lecture the theory of radiative transfer in the atmosphere is developed in a form appropriate to the interpretation of radiation measurements made by satellite instruments. The equations derived enable the radiation intensity reaching the satellite to be calculated if the state of the atmosphere and the absorption characteristics of its constituents are known. This is called the "forward problem"; in lecture 4 we shall consider inverse problems, i.e. estimation of the atmospheric state given measurements of upwelling radiation.

Although the treatment is fairly general, approximations are necessary and these have been made in such a way as to bias the treatment towards problems involving infra-red radiation. The effects of the approximations must be considered before applying the results to longer or shorter wavelengths. The most important simplification is the omission of scattering by clouds and aerosols. Clouds are treated as emitting/absorbing surfaces only and radiative transfer inside clouds is not considered. In this way we need only consider radiation fluxes along the satellite viewing direction. For many infra-red and microwave problems these approximations are very good.

2. Absorption, transmission and emission of monochromatic radiation

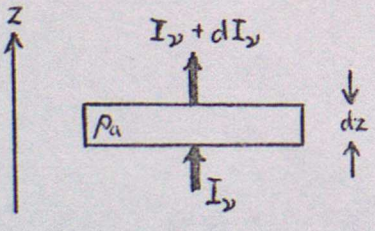

	Units
ρ_a = density of absorber	$Kg\,m^{-3}$
I_ν = intensity of radiation at wavenumber, ν	$Wm^{-2}sr^{-1}(cm^{-1})^{-1}$

The absorption of a beam of monochromatic radiation by an elemental path of absorbing gas is given by Lambert's law:

$$dI_\nu = - I_\nu k_\nu \rho_a dz , \qquad \ldots 2.1$$

and this effectively defines the monochromatic absorption coefficient, k_ν. Integrating over an arbitrary path from z_0 to z_1, we obtain

$$\int_{(I_\nu)_0}^{(I_\nu)_1} -dI_\nu / I_\nu = \int_{z_0}^{z_1} k_\nu \rho_a dz .$$

$$\therefore \quad (I_\nu)_1 = (I_\nu)_0 \exp\left\{ - \int_{z_0}^{z_1} k_\nu \rho_a dz \right\} . \qquad \ldots 2.2$$

Consequently the monochromatic transmittance of the path is given by

$$\tau_\nu(z_0, z_1) = \frac{(I_\nu)_1}{(I_\nu)_0} = \exp\left\{-\int_{z_0}^{z_1} k_\nu \rho_a \, dz\right\} \qquad \ldots 2.3$$

For a homogeneous path this simply reduces to $\tau_\nu = \exp\{-k_\nu \rho_a (z_1 - z_0)\}$, but we shall usually be considering vertical or slant paths through the atmosphere and, since k_ν and ρ_a are both in general functions of pressure and temperature, they will also be functions the distance, z, along the path.

Besides absorbing radiation, the element of gas considered above will emit radiation with an intensity dependent on its temperature. Consider the element enclosed in a black box with walls at the same temperature, T, as the gas. The intensity emitted by the box and incident on the gas in any direction is $B_\nu(T)$, the Planck function, and so from equation 2.1 the absorption by the element in the z-direction is $B_\nu(T)\, k_\nu \rho_a \, dz$. We know from the 2nd law of thermodynamics that in these circumstances the gas must neither tend to warm nor cool. Therefore the net change of radiation passing through an element of the gas in any direction must be zero, and so the intensity emitted in the z-direction must be $B_\nu(T)\, k_\nu \rho_a \, dz$. In other words, the coefficients of absorption and emission are both equal to k_ν. This is one of Kirchoff's laws and is strictly true only for thermodynamic equilibrium. Fortunately, in most of the neutral atmosphere local thermodynamic equilibrium (LTE) is a good approximation.

3. The radiative transfer equation

Consider the radiation emerging in the z-direction at point z from a path of gas between z_0 and z_1.

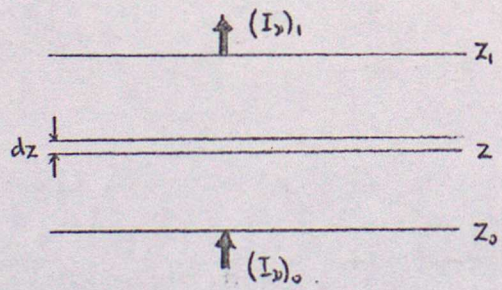

The intensity at z_1 is composed of 2 parts: a transmitted component, which depends on the intensity at z_0 and the transmittance from z_0 to z_1, and an emitted component, which includes the radiation reaching z_1 from all elements, dz, between z_0 and z_1. This leads to the equation,

$$(I_\nu)_1 = (I_\nu)_0 \, \tau_\nu(z_0, z_1) + \int_{z_0}^{z_1} \left[B_\nu\{T(z)\}\, k_\nu(z)\, \rho_a(z)\, dz\right] \tau_\nu(z, z_1). \qquad \ldots 3.1$$

By differentiating the expression for $\tau(z, z_1)$ (see equation 2.3) we obtain :

$$\frac{d\tau_\nu(z, z_1)}{dz} = k_\nu \rho_a \tau_\nu(z, z_1) . \quad \ldots 3.2$$

$$\therefore \boxed{(I_\nu)_1 = (I_\nu)_0 \tau_\nu(z_0, z_1) + \int_{\tau_\nu(z_0, z_1)}^{1} B_\nu\{T(z)\} \, d\tau_\nu(z, z_1)} \quad \ldots 3.3$$

This is the monochromatic radiative transfer equation.

4. Satellite measurements of radiation

Equation 3.3 can be applied to the monochromatic radiation emitted from the top of the atmosphere along a vertical or slant path and incident at a satellite instrument. Changing the notation so that $\tau_\nu(z)$ is the transmittance from height z to space, the radiance at the satellite is equal to intensity at the top of the atmosphere:

$$R_\nu = (I_\nu)_0 \tau_\nu(z_0) + \int_{\tau_\nu(z_0)}^{1} B_\nu\{T(z)\} \, d\tau_\nu(z) \quad \ldots 4.1$$

Note that $\tau_\nu(z)$ will also be a fuction of θ, the zenith angle of the path.

The first term in this equation represents the contribution from the underlying surface — cloud-top, land or sea — at height z . $(I_\nu)_0$ may include emitted, reflected and transmitted components. It depends in general on the temperature and emissivity of the surface and, if it is not black, on the reflecting properties of the surface and the downward radiation incident upon it and, for cloud, on the radiation transmitted through it. If the surface is black, then $(I_\nu)_0$ can be replaced by $B_\nu(T_s)$ where T_s is the surface temperature. In the infra-red this is usually an adequate approximation for the sea surface and water clouds but is less good for some land surfaces and ice clouds. In the microwave region, particularly over sea, the surface emissivity is very much less than one and reflection at the surface of down-welling atmospheric emission must be considered explicitly.

The second term in equation 4.1 is the contribution from the atmospheric emission and can be more readily appreciated when re-written:

$$\int_{\tau_\nu(z_0)}^{1} B_\nu\{T(z)\} \, d\tau_\nu(z) = \int_{z_0}^{\infty} B_\nu\{T(z)\} \frac{d\tau_\nu(z)}{dz} dz = \int_{z_0}^{\infty} B_\nu\{T(z)\} K_\nu(z) \, dz. \quad \ldots 4.2$$

$K_\nu(z)$ is known as a weighting function — it weights the Planck function profile corresponding to the atmospheric temperature profile. $K_\nu(z)$ is the derivative of the atmospheric transmittance profile: this is illustrated in figure 1 for two wavelengths, one of relatively strong and the other of relatively weak absorption. The height of the peak of the weighting function depends on the strength of the absorption and so, by using channels at different wavelengths with different absorption coefficients, radiation emanating from different layers of the atmosphere can be measured. When the first term in equation 4.1 is negligible compared to the second,

$$R_\nu = \int_{z_0}^{\infty} B_\nu\{T(z)\} \, K_\nu(z) \, dz , \quad \ldots 4.3$$

and so the radiance measured is a weighted average of the Planck function over the layer for which the weighting function has significant contribution. It is therefore related to the mean temperature of the layer. Because the weighting functions have considerable width, small scale vertical structure in the profiles of temperature (or composition) will have little effect on the measured radiances. For this reason we may expect variables related to the properties of an atmospheric layer (e.g. thickness) to be more accurately retrievable than those characterizing a specific level (e.g. tropopause temperature).

Equation 4.2 may be expressed using vertical co-ordinates other than height. For gases of constant mixing ratio, such as CO_2, a more convenient co-ordinate is log(pressure), since it yields weighting functions which are nearly (but not completely) independent of the temperature. This independence will be seen to be a desirable feature when we invert the radiative transfer equation to retrieve the temperature profile from the radiances.

5. Integration over frequency

So far we have only considered the monochromatic case. This is equivalent to assuming that k_ν is approximately constant over the pass-band of the radiometer. In the troposhere a typical infra-red spectral absorption line has a half-width (usually defined as the frequency interval over which the absorption coefficient falls from maximum to half-maximum) of about 0.1 cm^{-1}. Consequently a radiometer would need a pass-band considerably narrower than this for the monochromatic approximation to apply. At present, instrumental considerations necessitate radiometer spectral pass-bands of tens or hundreds of wavenumbers for temperature-sounding infra-red channels. This is very much greater than the half-width of a single spectral line and most channels encompass a spectral region with a complicated absorption spectrum caused by hundreds of lines. Therefore the radiative transfer equation needed for real instruments also contains an integration over wavenumber:

$$R = \frac{\int_0^\infty R_\nu f_\nu \, d\nu}{\int_0^\infty f_\nu \, d\nu} = \frac{\int_0^\infty \left\{ (I_\nu)_0 \tau_\nu(z_0) + \int_{\tau_\nu(z_0)}^1 B_\nu\{T(z)\} \, d\tau_\nu(z) \right\} f_\nu \, d\nu}{\int_0^\infty f_\nu \, d\nu} \quad \ldots 5.1$$

f_ν defines the "spectral response" of the instrument — it weights the incoming radiation at different wavelengths according to the relative sensitivity of the radiometer to such radiation. Typical relative responses are shown in figure 2 together with a molecular absorption spectrum for comparison. R, the radiance integrated over wavenumber, is usually normalised to the same units as B_ν by dividing by the integrated spectral response, $\int_0^\infty f_\nu d\nu$.

Equation 5.1 defines the FORWARD PROBLEM, i.e. given a knowledge of the atmospheric state and the concentrations and absorption characteristics of its absorbing species, we can calculate the intensity emitted from the top of the atmosphere as a function of wavenumber, and then, given the spectral response of the satellite instrument, we can calculate the radiance measured.

6. Absorption by single spectral lines

A single spectral line represents the transitions between 2 particular molecular energy states. The difference in energy between the 2 states determines the energy (and therefore the wavenumber) of the photon emitted/absorbed.

The monochromatic absorption coefficient for a single line depends on its strength and shape. The strength is the integrated absorption coefficient of the line,

$$S = \int_0^\infty k_\nu \, d\nu \qquad \ldots 6.1$$

and depends on the probability of occurrence of a transition between the energy states. The shape depends on the physical processes broadening the line. In the atmosphere 2 processes are important; the range of velocities of the absorbing molecules (relative to the observer) causes Doppler broadening, and the collisions with other molecules (which perturb the quantum mechanical wave functions) cause pressure or Lorentz broadening. Simple theory leads to the following expressions for absorption coefficient in each case:

$$\text{Doppler:} \quad k_\nu = \frac{S}{\sqrt{\pi}\,\alpha_D} \exp\left\{\frac{-(\nu-\nu_0)^2}{\alpha_D^2}\right\}, \qquad \ldots 6.2$$

$$\text{Lorentz:} \quad k_\nu = \frac{S}{\pi} \frac{\alpha_L}{\alpha_L^2 + (\nu-\nu_0)^2}. \qquad \ldots 6.3$$

ν_0 is the line centre wavenumber, and α_L and α_D are the so-called "half-widths" for Lorentz and Doppler broadening respectively. These shapes are illustrated in figure 3. The Doppler broadening "half-width" (actually the half-width at the point where the absorption coefficient is 1/e times its maximum value) is given by:

$$\alpha_D = \nu_0 \left\{\frac{2 k_B T}{mc^2}\right\}^{1/2}, \qquad \ldots 6.4$$

where k_B = Boltzmann's constant, T = temperature, m = molecular mass and c = speed of light. S and α_L are more difficult to evaluate theoretically. However, for many atmospheric gases, much theoretical and experimental work has been done to determine them and tabulations of ν_0, S and α_L for the lines of many bands are available (see, for example, McClatchey et al., 1973).

In the infra-red, pressure broadening is usually dominant in the troposphere. However, since α_L is proportional to pressure, higher in the atmosphere α_L and α_D are often comparable and a line shape which is a convolution of Lorentz and Doppler shapes must be used. Also, laboratory and atmospheric measurements have shown that the Lorentz shape obtained from simple molecular collision theory does not always correspond with measurement in the far wings; it is sometimes found necessary to adopt "sub-Lorentzian" or "super-Lorentzian" shapes, empirically determined, in order to model absorption coefficients to the required accuracy.

7. Some useful approximations

Equation 5.1 is difficult to evaluate in practice because it involves integrations of complicated functions over both atmospheric path and wavenumber. Several approximations are usually required when calculating radiance numerically and those given here are among the more useful.

7.1 The Curtis-Godson approximation

Each calculation of atmospheric transmittance involves an integration over an inhomogeneous path. This can be approximated by a homogeneous path containing the same absorber amount,

$$u = \int du = \int \rho_a(z)\, dz \,, \qquad \ldots 7.1$$

and with pressure and temperature equal to the absorber-weighted means of the inhomogeneous path:

$$\bar{p} = \frac{\int p\, du}{u} \,, \quad \bar{T} = \frac{\int T\, du}{u} \,. \qquad \ldots 7.2$$

The main application of the Curtis-Godson approximation is in the calculation of mean transmittances over a spectral interval, Δz, i.e. over a line or band of lines, for which the monochromatic approximation does not apply. If we can derive the mean transmittance,

$$\bar{\tau}_{\Delta\nu} = \frac{\int_{\Delta\nu} \tau_\nu \, d\nu}{\Delta\nu} \qquad \ldots 7.3$$

as a function of u, p and T for a homogeneous path (see below), then the Curtis-Godson approximation allows $\bar{\tau}_{\Delta\nu}$ to be calculated for an inhomogeneous path characterised by u, $\bar{p}$ and $\bar{T}$. It is exact in certain special cases, namely for the mean transmittance across a spectral line in the limits of both weak and strong absorption for an isothermal path where pressure broadening is the dominant line broadening mechanism. In other cases, including monochromatic calculations, the approximation is often adequate and the error depends on the degree of inhomogeneity.

7.2 Path splitting

For monochromatic calculations the above approximation is improved by treating the path as a series of J more nearly homogeneous sections and applying the Curtis-Godson approximation to each. Then, if $(T_\nu)_j$ is the transmittance of the jth section, the combined transmittance is given by

$$\tau_\nu = \prod_{j=1}^{J} (\tau_\nu)_j \,. \qquad \ldots 7.4$$

Note that in general equation 7.4 cannot be extended to mean transmittances:

$$\bar{\tau} \neq \prod_{j=1}^{J} \bar{\tau}_j \,. \qquad \ldots 7.5$$

This restriction applies most forcibly to series paths of the same absorbing gas, for which the spectra for path sections are highly correlated with each other. However equation 7.4 is applicable to the mean transmittances of spectra which are not highly correlated. Therefore one can calculate the mean transmittances of different gases separately and often approximate their combined mean transmittance accurately using equation 7.4.

7.3 Line-by-line integrations

The integration over wavenumber is most accuately performed using a "line-by-line" technique. This involves a series of monochromatic calculations at sufficiently high density in wavenumber space that the transmittance function between chosen points can be accurately interpolated and hence integrated numerically. The density required depends on the line widths and the accuracy to which the result is needed. The contributions from all significant lines are calculated at each wavenumber and so the effects of overlapping lines are automatically included. For complicated spectra this method is very demanding on computer time and requires an accurate knowledge of the spectral line parameters — their positions, strengths and shapes.

7.4 Band models

Until quite recently line-by-line integrations have been impracticable because of the computing power required. Also, transmittances of the accuracy required (or justified by the errors in the spectral data) may often be calculated much more efficiently using band model techniques. These approximate the mean transmittance (as defined by equation 7.3) over an interval of, say, 20 cm^{-1} containing many lines. For a theoretical discussion of band models and the calculation of mean transmittances see Goody (1964) or Rodgers (1976).

Having calculated mean transmittances over intervals of width $\Delta\nu$ across the spectral response of the radiometer, we can now compute the total radiance as the sum of contributions from all intervals:

$$R \simeq \sum_i R_i f_i \Big/ \sum_i f_i \qquad \ldots 7.6$$

where f_i is the mean relative spectral response for the ith interval and

$$R_i = \frac{\int_{\Delta\nu} (I_\nu)_o \tau_\nu(z_o)\, d\nu + \int_{\Delta\nu} \int'_{\tau_\nu(z_o)} B_\nu(z)\, d\tau_\nu(z)\, d\nu}{\int_{\Delta\nu} d\nu}$$

$$\simeq (\overline{I_o})_i\ \overline{\tau}_i(z_o) + \int'_{\overline{\tau}_i(z_o)} \overline{B}_i(z)\, d\overline{\tau}_i(z) \,. \qquad \ldots 7.7$$

Here, mean values have been used for $(I_\nu)_o$ and $B_\nu(z)$ for each interval, $\Delta\nu$. This is usually a good approximation for intervals $\lesssim 20$ cm^{-1} since $(I_\nu)_o$ and $B_\nu(z)$ are slowly varying functions of ν.

The integration over the atmospheric path is usually replaced by a summation over discrete layers of atmosphere. If $\overline{B}_{ni}$ is the mean Planck function for the ith spectral interval and the layer between levels $z=z_n$ and $z=z_{n+1}$, then

$$R_i \simeq (\overline{I_o})_i\ \overline{\tau}_i(z_o) + \sum_n \overline{B}_{ni} \left\{ \overline{\tau}_i(z_{n+1}) - \overline{\tau}_i(z_n) \right\}, \qquad \ldots 7.8$$

where the summation is over all layers between z_o and space. Given a model of $\bar{\tau}_i(z)$ for each interval in terms of the absorber parameters calculated using the Curtis-Godson approximation, equation 7.8 and hence equation 7.6 can now be evaluated numerically.

A widely used model which adopts this general approach and provides transmittances adequate for work at low spectral resolution is the LOWTRAN model of the USAF Geophysics Laboratory (Kneizys et al., 1980). This model is not appropriate either for obtaining very accurate transmittances or for application to narrow-band radiometers.

7.5 Fast, empirical models

With the increasing availability of computer power and the requirement for ever-increasing accuracy in transmittance calculations, the use of band models has declined. Line-by-line integrations form the basis of most methods in current use, but even today line-by-line models are too computationally expensive to be used for simulating radiances in those applications for which many thousands of atmospheric profiles must be considered. This precludes their use as part of routine atmospheric profile retrieval algorithms and also for many research and development experiments.

A satisfactory compromise, currently adopted for many atmospheric sounding problems, is to use a line-by-line model to make very accurate transmittance calculations for a small number ($\lesssim 100$) of widely differing atmospheric profiles, and then to use an empirical relation derived from these results to obtain transmittances corresponding to all other atmospheric profiles. McMillin and Fleming (1976) describe a particular example of this approach appropriate to calculating transmittances through an atmosphere containing a uniformly-mixed absorber. They derive an expression for a radiometer channel relating the mean transittances from pressure level p_n to space to the corresponding values from pressure level p_{n-1} to space:

$$\bar{\tau}_n = \bar{\tau}_{n-1} \left[\alpha_n + \beta_n \Delta T_n + \gamma_n \Delta T_n^2 + \delta_n \Delta T_n^* + \epsilon_n \Delta T_n^{**} \right] \quad \ldots 7.9$$

where ΔT_n is the difference between the temperature of a particular profile and some mean profile at pressure level p_n.
ΔT_n^* is the pressure-weighted mean temperature profile difference above pressure level p_n, i.e. $\Delta T_n^* = \int_o^{p_n} \Delta T(p)\, dp \Big/ \int_o^{p_n} dp$,

$$\Delta T_n^{**} = \int_o^{p_n} p\, \Delta T(p)\, dp \Big/ \int_o^{p_n} dp \ ,$$

and α_n, β_n, γ_n, δ_n, ϵ_n are empirical coefficients determined from a regression analysis of the line-by-line calculations for a small number of profiles.

The inherent approximations introduce errors which are much smaller than other uncertainties in the calculations. Two later papers extend the technique to cover varying angles of view (Fleming and McMillin, 1977) and non-uniformly mixed gases (McMillin et al., 1979). A summary of the methods of transmittance calculation used in support of the operational processing at NOAA (and in Met.O.19) for the TIROS Operational Vertical Sounder (TOVS) instruments is given by Weinreb et al., 1981.

An alternative approach to the problem of developing a comparatively efficient alternative to full line-by-line calculations has been developed by Scott and Chedin (1981) in their "Automatized Atmospheric Absorption Atlas" ("4A") model.

REFERENCES

Fleming H.E., McMillin L.M.
Appl.Opt., 16, 1366-1370 (1977).
Atmospheric transmittance of an absorbing gas.
2: a computationally fast and accurate transmittance model for slant paths at different zenith angles.

Goody R.M.
Oxford University Press (1964).
Atmospheric radiation. I: theoretical basis.

Houghton J.T.
Cambridge University Press (1977).
The physics of atmospheres.

Kneizys F.X., Shettle E.P., Gallery W.O., Chetwynd J.H., Abren L.W., Selby J.E.A., Fenn R.W., McClatchey R.A.
AFGL-TR-80-0067, Environ.Res.Pap.697 (1980).
Atmospheric transmittance/radiance computer code LOWTRAN 5.

McClatchey R.A., Benedict W.S., Clough S.A., Burch D.E., Calfee R.F., Fox K., Rothman L.S., Garing J.S.
AFGRL Report TR-73-0096, Environ.Res.Pap.434 (1973).
AFGRL atmospheric absorption line parameter compilation.

McMillin L.M., Fleming H.E.
Appl.Opt., 15, 358-363 (1976).
Atmospheric transmittance of an absorbing gas:
a computationally fast and accurate transmittance model for absorbing gases with constant mixing ratios in inhomogeneous atmospheres.

McMillin L.M., Fleming H.E., Hill M.L.
Appl.Opt., 18, 1600-1606 (1979).
Atmospheric transmittance of an absorbing gas.
3: a computationally fast and accurate transmittance model for absorbing gases with variable mixing ratios.

Rodgers C.D.
NCAR Tech.Note NCAR/TN 116, March 1976.
Approximate methods of calculating transmissions by bands of spectral lines.

Scott N.A., Chedin A.
J.Appl.Meteor., 20, 802-812 (1981).
A fast line-by-line model for atmospheric absorption computations: the automatised atmospheric absorption atlas.

Weinreb M.P., Fleming H.E., McMillin L.M., Neuendorffer A.C.
NOAA Tech.Rep. NESS 85 (1981).
Transmittances for TOVS.

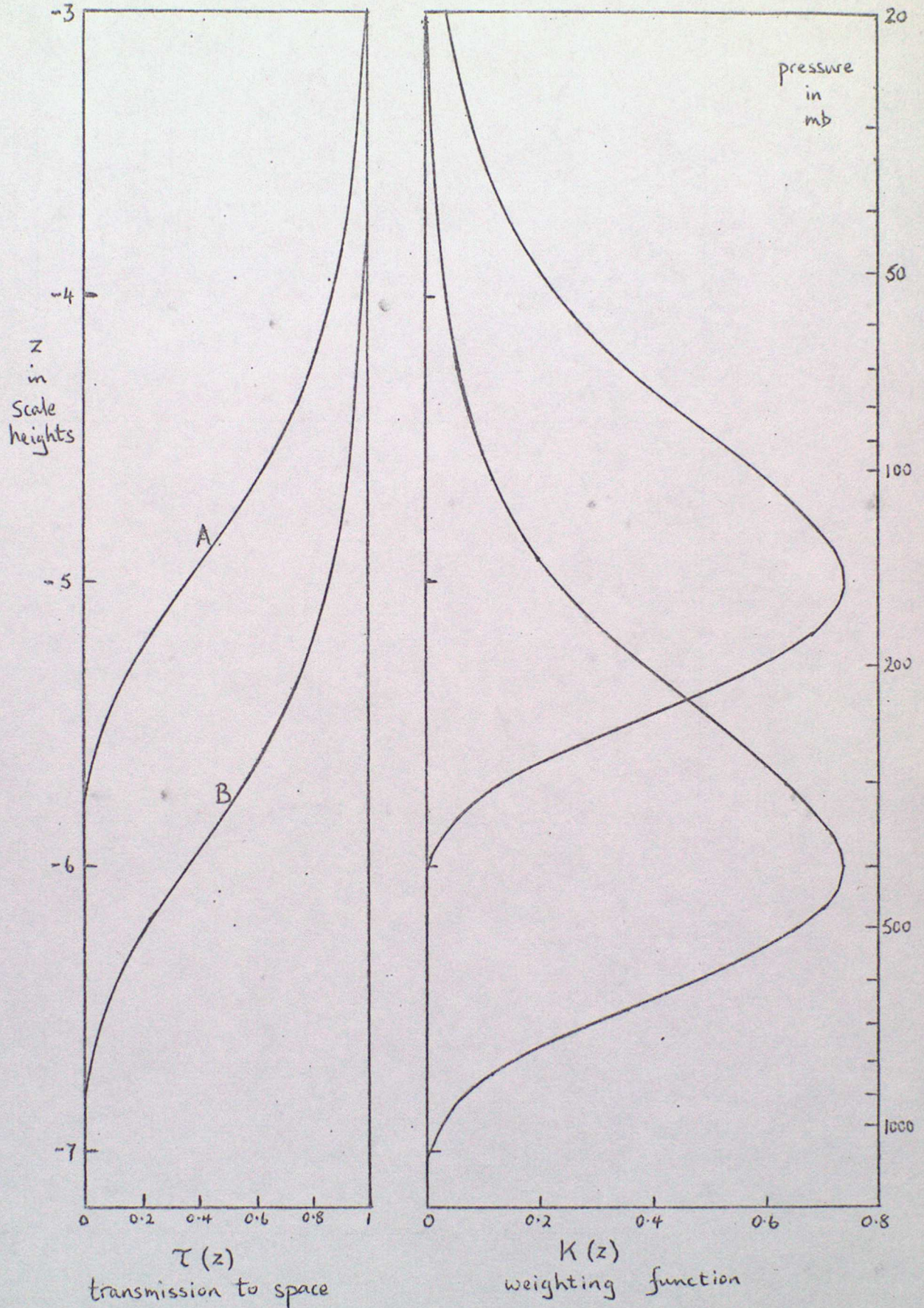

Figure 1 — 2 idealised transmission profiles and weighting functions at wavelengths with different absorption coefficients.

z is in scale heights, i.e. $z = -\ln(\text{pressure in mb})$

A : for wavelength of relatively strong absorption

B : for wavelength of relatively weak absorption

(a)

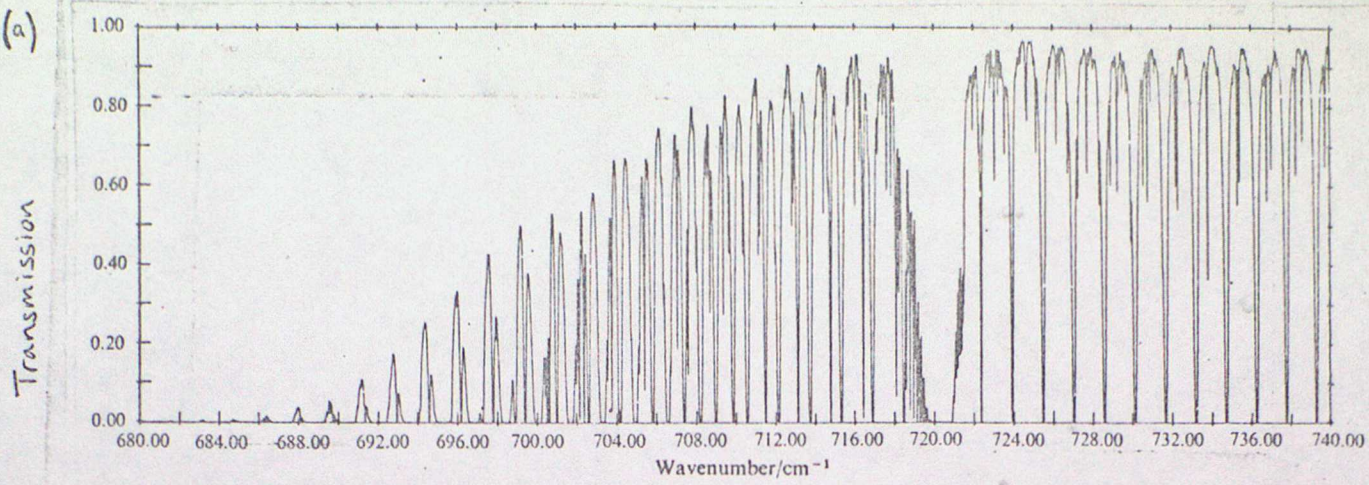

(b)

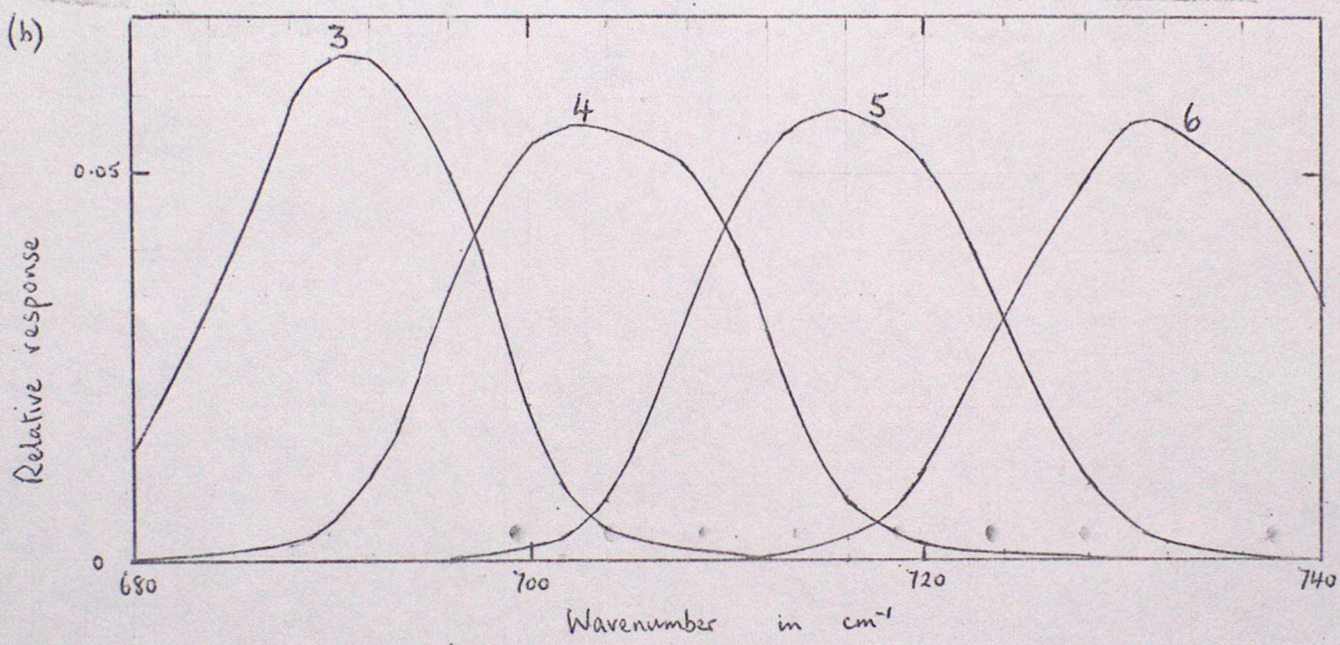

Figure 2

(a) Illustrating the fine structure of part of the 15μm CO_2 absorption band. Transmission of a 10 km horizontal path at 12 km altitude. [Taken from Houghton (1977), p. 34.]

(b) The relative spectral responses of channels 3, 4, 5 and 6 of the HIRS instrument on the TIROS-N series. [c.f. Lecture 4, table 1 and figure 1].

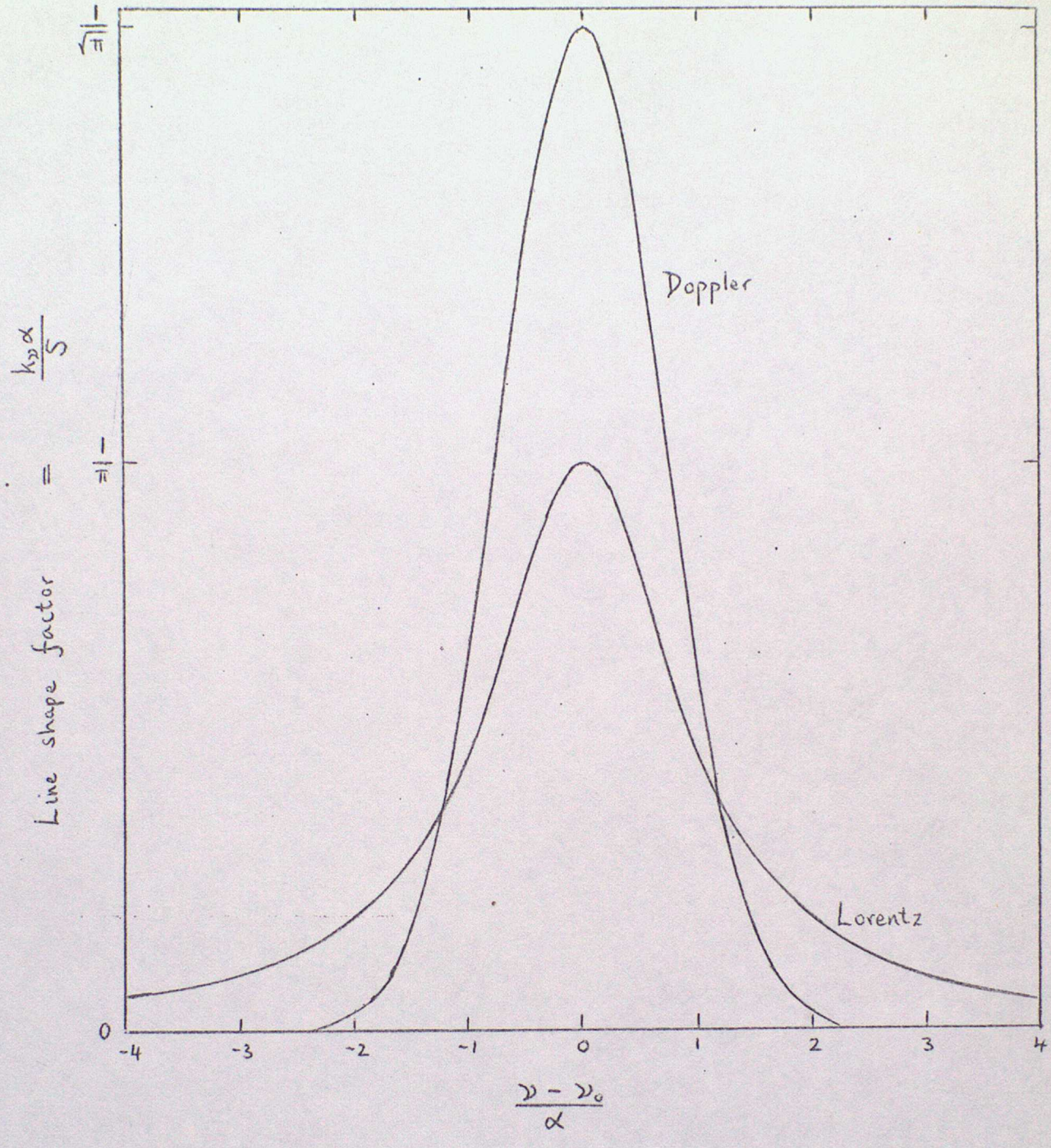

Figure 3

Illustrating the line shapes caused by Doppler and Lorentz broadening. α is the appropriate "half-width" for the broadening mechanism.

Advanced Lectures 1984

Satellite Meteorology

Lecture 3 Dr D R Pick Met O 19

The Office's contribution to satellite instruments

1. Introduction

The radiative transfer equation can be written as follows

$$R_\nu(\theta) = R_\nu^{\uparrow}(\theta) + \tau_o(\nu,\theta).\left(\varepsilon(\nu,\theta,S).B(\nu,T_s) + (1-\varepsilon(\nu,\theta,S)).R_\nu^{\downarrow}(\theta)\right) \quad \ldots 1.1$$

where $R_\nu(\theta)$ = the radiation emerging from the top of the atmosphere at frequency ν and angle θ with respect to the local vertical. Units are usually mW/(m^{2}sr cm^{-1}).

$R_\nu^{\uparrow}(\theta)$ = the 'upward' contribution

$\tau_o(\nu,\theta)$ = the atmospheric transmissivity between the surface and the top of the atmosphere

$\varepsilon(\nu,\theta,S)$ = the surface emissivity, which is also a function of the surface characteristics and surface wind speed (~ 1 in IR and .5 - .7 in microwave spectral region over sea).

$B(\nu,T_s)$ = the Planck function evaluated for the surface temperature T_s.

$R_\nu^{\downarrow}(\theta)$ = the 'downward' contribution (prior to reflection by the surface and transmission through the intervening atmosphere).

further $$R_\nu^{\uparrow}(\theta) = \int_{z=0}^{\infty} B(\nu,T_z).\frac{d\tau^{\uparrow}(\nu,\theta,z)}{dz}.dz \quad \ldots\ldots 1.2$$

where $\tau^{\uparrow}(\nu,\theta,z)$ = the transmissivity between a layer at height z and the top of the atmosphere.

This lecture is concerned with the practical measurement of the radiation incident on a satellite radiometer, how the spectral response of such a radiometer is determined and how some of the spectroscopy included in equation 1.1 is experimentally verified. The discussion is limited to those instruments in which the Meteorological Office has an active role viz: the Stratospheric Sounding Unit, the Advanced Microwave Sounding Unit and the Along the Track Scanning Radiometer.

2. Basic constraints on space borne radiometers

2.1 Infrared Radiometry

The energy reaching a detector in a radiometer is given by

$$R_i(\phi) = \int_i \tau_i(\nu) \cdot \iint_\phi g_i(\theta,\psi) \cdot A_i \cdot R_\nu(\theta,\psi) \cdot d\nu \cdot d\theta \cdot d\psi \quad \ldots 2.1$$

where $\tau_i(\nu)$ = the spectral response of the ith channel

$g_i(\theta,\psi)$ = the angular response of the viewing telescope about scan angle ϕ

A_i = the appropriate area for the input telescope.

$R_\nu(\theta,\psi)$ = 1.1 about the scan angle ϕ

The spatial resolving power (or viewing pixel area) is given by $\iint G_i(\theta,\psi) d\theta d\psi = \Omega$ (x height of radiometer^2). The product $A\Omega$ is a basic parameter for a radiometer since ideally $A\Omega$ is conserved during passage of radiation through an optical system. Loss due to optical aberrations and diffraction effects are usually included in the τ term. For a 'small' external field of view 2.1 can be simplified to give

$$R_i(\phi) = A\Omega \int_i \tau_i(\nu) R_\nu(\phi) d\nu \quad \ldots \quad 2.2$$

The trade-off loop logic can now be seen as follows

	comments
Channel purpose	
↓	
choose spectral region	
↓	
detector type	eg. uncooled thermal, cooled photo-conductor, cooled photo-voltaic.
↓	
potential performance	$\equiv \Delta R$ at detector, depends inter alia on sample/measurement time
↓	
pixel size required (Ω)	atmospheric structure considerations.
↓	
practical telescope size (A)	space craft constraints and money.
↓	
$\tau_i(\nu)$	effects atmospheric weighting function.
↓	
useful performance	
↓	
yes – next channel	
No ←	

The potential channel performance is then usually given in terms of NER (Noise equivalent radiance at the input) or NET_T (noise equivalent temperature at the input for a sense brightness temperature of T). The A term has been scaled out. Typically NET performance requirements per pixel are in the range .1K for sea surface temperature mapping to $\lesssim$1K for stratospheric temperature.

The absolute accuracy of the measurement of radiation is also required to a similar level ($\sim 1/4$K). Current radiometer design is such that this requirement can only be met by providing an inflight calibration system and such a system must encompass as much of the optical system as is economically possible. Such an inflight calibration system can consist of an 'ambient' target and space (SSU, AMSU-B) or two calibration targets at different temperatures (ATSR). Any inaccuracy in this calibration system or scan dependent errors are quantified by vacuum chamber tests before launch.

Microwave radiometers are subject to similar guidelines with two notable exceptions. The radiometer is usually constructed as a superhetrodyne system with a power measurement being made using a diode on the shifted frequency. The other exception is that A Ω cannot be decoupled into a separate choice of A and Ω. This is because the external acceptance solid-angle Ω is primarily determined by diffraction considerations of the radiation field of area A, since the wavelength of the radiation is comparible with the dimensions of A.

2.2 Spectroscopic considerations

Besides A Ω the other important term is $\tau_i(\nu)$ The quantity $W=\int_\nu \tau_i(\nu)\,d\nu$ usually expressed in cm^{-1} is called the (spectral) equivalent width. The energy reaching the radiometer detecting system is linear in this term. However as discussed in lecture 2 an increase in W, while improving the signal to noise or NET usually leads to an increased spread of the weighting function. This happens when such an increase causes an increase in the distribution of absorption coefficients accepted by the radiometer channel.

Current infrared systems used for temperature sounding eg HIRS on the TIROS-N series of weather satellites uses narrow band (9-10 cm^{-1}) multilayer filters to define the spectral regions required. Such a filter contains many lines leading to broadening of the weighting function. State of the art filters can achieve $\sim 3cm^{-1}$ with $\tau \sim .6$ (c.f $10cm^{-1}$ $\tau \sim .9$) with a factor of 5 loss in NET. The SSU described below partially over-comes this problem by using a selective filtering technique. A dramatic improvement in spectral resolution in the infrared needs either a grating system or an interferometer system. Such a spectrometer has been proposed for TIROS-N by Kaplan and Chahine and is called the Advanced Meteorological Temperature Sounder: This spectrometer is however about 5-10 times bigger than HIRS and consumes all the available spacecraft power and is not likely to be flown in the next decade. A more practical interferometer system has been proposed for the geostationary satellites by W L Smith. This 'High resolution Interferometer Sounder (HIS) proposed is shortly to undergo aircraft trials. The spectral resolution in this case is $<.7cm^{-1}$.

2.3 Spacecraft environment and constraints

The advanced TIROS-N satellite shown in Figure 1 illustrates most of the salient features of a civilian weather satellite. Electrical power is obtained from the solar panel array (when illuminated by sunlight) through the use of silicon photocells. The efficiency of this conversion process is about 3% (i.e. .03 x 1.4 KW/m^2 ~ $40W/m^2$). Rechargable batteries are used to maintain spacecraft power availability as the solar generated power varies around the orbit.

Thermal control of the satellite requires that a thermal balance is achieved between the input radiation sources (earth thermal radiation (~240K), earth albedo, varing solar radiation (up to ~1.4 kW/m^2), (cosmic background ~2.85K)), internal electrical heating and thermal emission from the spacecraft itself. Basic control is achieved through the use of a combination of surface finishes and liberal use of multilayer thermal blanket. A serious problem associated with such blankets is their propensity to exude large quantities of water vapour especially during the first weeks in orbit. This water vapour can condense onto optical components, particularly those components whose temperature has been deliberately cooled with respect to the surroundings, with a consequential degradation in radiometric performance.

Orbital variations in radiation loading is damped to some extent by the thermal capacity of the satellite systems. Finer control to about 1K is achieved through the use of louvre systems. Locally much finer control to ~.01K can be achieved by electrical thermostating arrangements. Hence for example a space borne precision radiometer is designed to survive +40°C and to operate at 20°C with an orbital variation of about 1-2K (over 100 min) with particularly sensitive areas controlled to ~.01K if required. This is a more stable environment than obtained in an average laboratory.

Satellite orientation is actively controlled through servo controlled gyroscopes. Coarser control is achieved by dumping momentum through gas discharge via suitably sited nozzles.

2.4 Resources needed to design and build a flight radiometer

The design and building of a radiometer for space use envolves scientists and engineers with a variety of backgrounds as well as an intensive test and calibration programme. To put this activity in prospective for the SSU the resources for the SSU were:

Development model and 4 flight models employed 80 man years of effort at the contractors, cost ~ £3.5m (83 prices) and envolved 20my of effort at the Met Office in monitoring the contractor, developing the science, field trials, providing the inhouse calibration facility and scientifically testing the 5 SSU's.

A further 4 flight models cost £1.7m (83 prices).

3. The Stratospheric Sounding Unit

The Stratospheric Sounding Unit was built by Marconi Space Defence Systems for the Meteorological Office. Some 8 of these units have been built and tested. Four have been successfully flown on the TIROS N series of weather satellites. The SSU is a self calibrating infrared radiometer sounding the temperature structure of the stratosphere through making absolute radiometric measurements of emission by atmospheric carbon dioxide in the 15μm band.

3.1 Spectroscopic selection

The problem mentioned above of restricting the range of absorption values while still accepting a sufficiently wide spectral range to provide acceptable radiometric performance is solved in the SSU by using a selective chopping technique. Figure 2 outlines the SSU optical system. Signal modulation is provided by changing the amount of carbon dioxide in the transmission cell A shown in this figure. The effect on the radiation passing through the system is illustrated in figure 3 for the top channel 27. Curves A and B of figure 3b indicate the range of transmission values for the cell for a single carbon dioxide line in the band at 15 μm. Cycling between these values causes selective modulation with a spectral frequency dependence given by curve C. i.e. only spectral regions from 1 x 10^{-3} → 6 x 10^{-3} cm^{-1} from the line centre are modulated for lines of this strength. The broad band filter also shown in figure 2 limits the spectral response lines in 15 μm band over some 60cm^{-1}. The equivalent width of this channel is ~ .4cm^{-1}. Increasing the amount of carbon dioxide gas in the cell moves the effective spectral modulation curve 'c' (fig 3b) away from the line centre and hence lowers the weighting function in the atmosphere.

Figure 4 shows the weighting functions achieved for the SSU. Curve 1 is the top channel achieved by a 3cm^{-1} filter in HIRS using the same band of CO_2. Of note is the much better height resolution of the SSU when compared to that which can be achieved by the simple filter technique used in HIRS. However the selective chopping technique is not 'perfect'. Curve 24 in figure 4 illustrates the near monochromatic weighting function achieved by the Microwave Sounding Unit on TIROS N. In the 1990's an Advanced Microwave Sounding Unit which among others will have channels with weighting functions within the range of the SSU, will replace the SSU as the stratospheric sounder on the TIROS Series.

3.2 Spectroscopic verification

In lecture 2 mention was made of the Curtis Godson approximation. This approximation allows the direct measurement of weighting functions in the laboratory using a uniform pressure path provided that for such a path and for the equivalent varing pressure path in the atmosphere the quantities $\int du$ and $\int p\,du$ are matched. For CO_2 an approximate fit can be found for laboratory paths of ~ 10m and a CO_2/N_2 mixing ratio of about .3.

Figure 5 outlines the system installed in a Met O 19 laboratory to make such measurements. In addition to such laboratory measurements a direct measurement of atmospheric transmission has been made. For this measurement a high pressure cell -peak of weighting function at 15 mbar -

was mounted at the output of a balloon borne sun-seeker and was used to make direct measurements of solar intensity as a function of height from the ground to a balloon float altitude of 4 mbars.

Both the balloon borne experiment and the laboratory measurements demonstrated the need for small empirical corrections to the line by line theory used to calculate the atmospheric weighting function.

Account must also be taken of a weak ozone band at 14 μm. Measurements were made with ozone in the weighting function rig transmission cell. These ozone transmission measurements demonstrated that a small correction (~.15K) is needed only in the radiances measures by channel 25 (the lowest SSU weighting function). The varation of this correction (~.05K) with variation in atmospheric ozone is ignored for the SSU. The correction needed by a filter radiometer is much larger - eg. for HIRS the worst channel has 1-2K offset where the size depends on ozone column amount.

3.3 Radiometric assessment

Also shown in figure 5 is the 'earth' target used to verify the SSU inflight calibration. The target fills the whole scan angle of the SSU hence tends to be rather bulky. Even from this sketch the salient features in the design of precision calibration target can be seen. The SSU views the corrugations shown on the base of the target. These corrugations improve the blackness of a plane painted surface from ~ .95 - ~.99 and the baffle arrangement further enhance this emissivity to ~.998 as well as reducing the temperature gradients within the paint. Helium gas, thermostatically controlled, is vigorously pumped round the target and its baffle to minimize temperature gradients < .2K within a field of view and <~.5K in all fields of view.

4. ASMU-B - a new microwave instrument

The next major instrument development for the TIROS N system is the enhancement of the present 4 channel microwave sounding unit (MSU) by replacement with a 20 channel advanced microwave sounding unit. Such a radiometer will have significant impact on satellite based atmospheric temperature and humidity retrievals. This is mainly through providing soundings under cloudy conditions, since the current infrared system can only provide retrievals in clear areas or in gaps between clouds and cannot probe active frontal systems. Humidity profiles near the ground and quantitative preciptiation mapping are also some of the new products expected from AMSU. Retrievals of humidity will be discussed in lecture 4.

The channels are listed in table 1 and figure 6 shows the calculated weighting functions for the AMSU sounding channels. AMSU has been divided into two sections AMSU-A the first 15 channels, and AMSU-B the channels 16-20. The Met Office is becoming envolved in the processes necessary to provide the AMSU-B units.

4.2 Spectroscopy of AMSU B

The AMSU channels are located in the microwave region 20-190 GHz. Figure 7 shows this part of the spectrum. There are 5 main features apparent. Features 1, 4 and 5 are isolated water vapour lines, 2 is a band of some 50

oxygen lines while 3 is an isolated oxygen line at 118 GHz (potentially a frequency that can be used for microwave temperature sounding from a geostationary satellite). AMSU-B has a channel in the window region between 2 and 3 - here the main contribution is due to wing effects of water vapour and a continuum term, a channel at 166 GHz and 3 channels straddling the single line at 183 GHz at differing locations down the line.

A field trial programme is already under way to experimentally test the spectroscopy of AMSU-B. Dr T Wilheit of NASA, GSFC has built a radiometer with channels similar to AMSU-B (except for the 166 GHz channel). Several flights with his radiometer mounted on an aircraft have been made. On the most recent flight the Met Office provided in situ measurements by dropping sondes in a joint exercise between Gander and 6°N. The results indicate that there is good agreement between theoretical brightness temperature calculations based on the drop sonde profile data and measured brightness temperature for the channels near the strong water vapour line - but poor agreement ~10-15K difference in the window channel region at 90 GHz.

Laboratory measurements are planned and further aircraft trials are needed to solve this discrepancy.

4.3 Radiometric aspects

Precision radiometric calibration of a microwave radiometer present some challenging technical problems, which have yet to be tackled. The main problems are the lack of 'black' paint, the large field of view of AMSU-B presence of side lobes to this field of view and the possibility of resonant scattering (induced by standing waves set up in the calibration target cavities because of the wavelengths involved are comparable with the structuring used to enhance the basic absorption properties of a calibration target).

5. The Along-Track Scanning Radiometer (ATSR)

ATSR is a sensitive infrared radiometer designed to measure sea-surface temperature with an accuracy of better than ±0.5K. This 4 channel radiometer is being designed by RAL and is expected to fly on ERS-1, with a tentative launch date of 1988. The spectral frequencies for ATSR have been chosen to be identical to those of the four channel AVHRR currently providing the operational sea-surface temperature from the A TIROS-N series. However ATSR is expected to improve on AVHRR by viewing the same area of the earth's surface at two angles, which gives a direct measurement of the 'atmospheric correction' to the surface radiance.

Figure 8 shows an outline of the instrument. This will be the first civilian instrument with detectors cooled by a Stirling engine cooler. This cooler has been developed by Oxford University Engineering department. The cooler arrangement uses the same type of pressure 'modulation' mechanics as the SSU. A prototype model has been built with a heat dumping capability of ~.5W at 75K (compared to passive coolers of 10-50 mW at ~100K).

The Meteorological Office contribution to this instrument is through providing the detail design and fabrication of the focal plane assembly. The high performance required by ATSR has lead to the design shown in figure 9. The ultimate performance of cooled detectors is achieved when

the background radiation is reduced to a low level to avoid the statistical fluctuation of the quanta from the background being the main noise source. To achieve this the entrance aperture, beam dividers, optical filters and detectors together with some active preamplifier components need to be cooled to 80K. This design is now starting its environmental testing programme (vibration to simulate spacecraft launch and thermal shock tests).

The Meteorological Research Flight is also involved in mounting an experiment on their Hercules aircraft. This experiment is designed to experimentally verify the dual angle approach of compensating for atmospheric absorption and emission effects on the sea temperature measurements.

6. Summary

The table lists the Meteorological Offices involvement in instrumental hardware.

Table of involvement in instrument hardware

unit	involvement	spacecraft	launch	data
SSU	all aspects	TIROS-N series	78→88	stratospheric thickness maps 150km resolution.
AMSU-B	all aspects	TIROS-NEXT	90→?	maps at 15 km resolution of water vapour profiles, liquid water and precipitation.
ATSR	focal plane assembly design	ERS-1	88(?)	sea-surface temperature maps ~2km resolution.

References

There is not a very extensive open literature on development and testing of satellite radiometers. The following list is a selection of the more general concepts.

H. H. Aumann and M T Chaline 1976 'Infrared multidetector spectrometer for remote sensing of temperature profiles in the presence of clouds' App. Optics 15P p2091-2094.

D. L. Croom 1982 'Workshop on next generation operational satellite meteorological sounding systems' RAL 2-5 Nov 1982.

D. E. Miller, J. L. Brownscombe, C. P. Carruthers, D. R. Pick and K. H. Stewart 1980 'Operational temperature sounding of the stratosphere' Phil Trans R. Soc Loud A296 p 65-71.

W. L. Smith et al 1983 'HIS a satellite instrument to observe temperature and moisture profiles with high resolution' Amer. Met. Soc 5th Conf Atmos Radiat Oct 31 - 4 Nov 1983 p1-9.

D. H. Staelin 1981 'Passive microwave remote sensing for meteorology' IEEE Digest Int Geosci Remote Sensing Symp June 8-10 1981 p 158-162.

TABLE 1A

AMSU-A CHANNEL CHARACTERISTICS (as of 5 Oct 1982)

Ch No. Designation	Center Frequency (GHz)	No. of Pass Bands	Maximum Bandwidth (MHz)	Center Frequency Stability (MHz)	Temperature Sensitivity (K) Goal	Temperature Sensitivity (K) Req'd	Absolute Calibration Accuracy (K)	Beam Width (degree)	Prime Polarization
1	23.800	1	270	20	0.20	0.50	2.0	3.3	V
2	31.400	1	200	20	0.20	0.50	2.0	3.3	V
3	50.300	1	200	50	0.30	0.40	1.5	3.3	V
4	52.800	1	400	5	-	0.25	1.5	3.3	V
5	53.330	1	400	5	-	0.25	1.5	3.3	V
6	54.400	1	400	10	-	0.25	1.5	3.3	-
7	54.940	1	400	10	-	0.25	1.5	3.3	-
8	55.500	1	400	20	-	0.25	1.5	3.3	
9	57,290.334 MHz = f_{10}	1	330	0.5	-	0.25	1.5	3.3	-
10	$f_{10} \pm 217$ MHz	2	78	0.5	-	0.35	1.5	3.3	-
11	$f_{10} \pm 322.2 \pm 48$ MHz	4	36	0.5	-	0.35	1.5	3.3	-
12	$f_{10} \pm 322.2 \pm 22$ MHz	4	16	0.5	-	0.50	1.5	3.3	-
13	$f_{10} \pm 322.2 \pm 10$ MHz	4	8	0.5	-	0.80	1.5	3.3	-
14	$f_{10} \pm 322.2 \pm 4.5$ MHz	4	3	0.5	-	1.30	1.5	3.3	-
15	89.0	1	6000	50	0.60	1.00	2.0	3.3	V

TABLE 1 B

AMSU-B CHANNEL CHARACTERISTICS

Ch No. Designation	Center Frequency (GHz)	No. of Pass Bands	Maximum Bandwidth (MHz)	Center Frequency Stability (MHz)	Temperature Sensitivity (K) Goal	Temperature Sensitivity (K) Req'd	Absolute Calibration Accuracy (K)	Inter-channel calibration, accuracy (K)	Beam Width (degree)	Prime Polarization
16	89.0	1	6000	50	0.60	1.00	1.0	.5	1.0	V
17	166.0	1	4000	50	0.60	1.00	1.0	.5	1.0	V
18	183.31±1.00	2	1000	30	0.60	1.00	1.0	.5	1.0	-
19	183.31±3.00	2	2000	30	0.60	1.00	1.0	.5	1.0	-
20	183.31±7.00	2	4000	30	0.60	1.20	1.0	.5	1.0	(V)

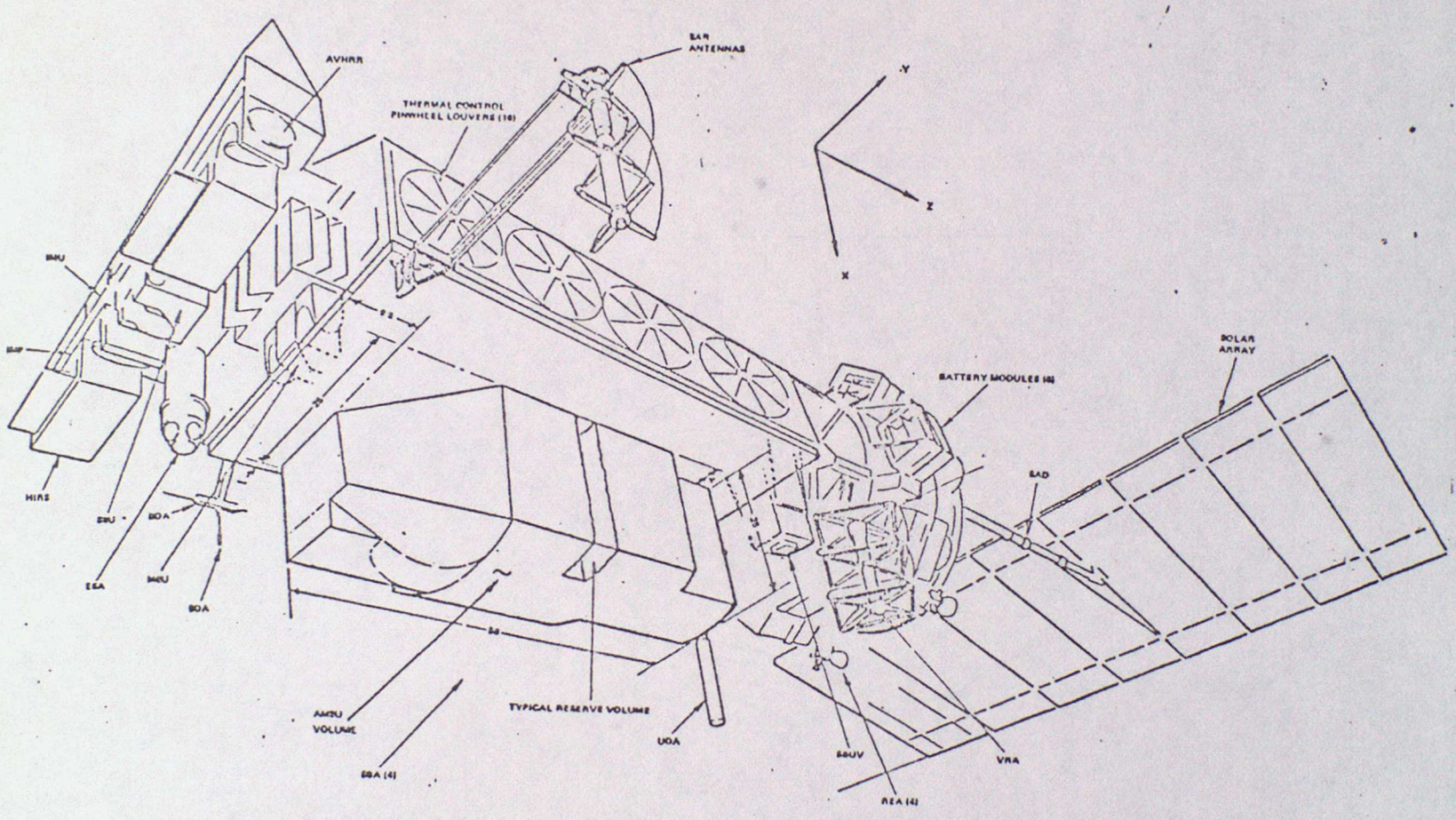

NOTE: DIMENSIONS ARE APPROXIMATE FOR INITIAL LAYOUT ONLY.
DIMENSIONS ARE IN INCHES.

Figure 1 Advanced TIROS-N

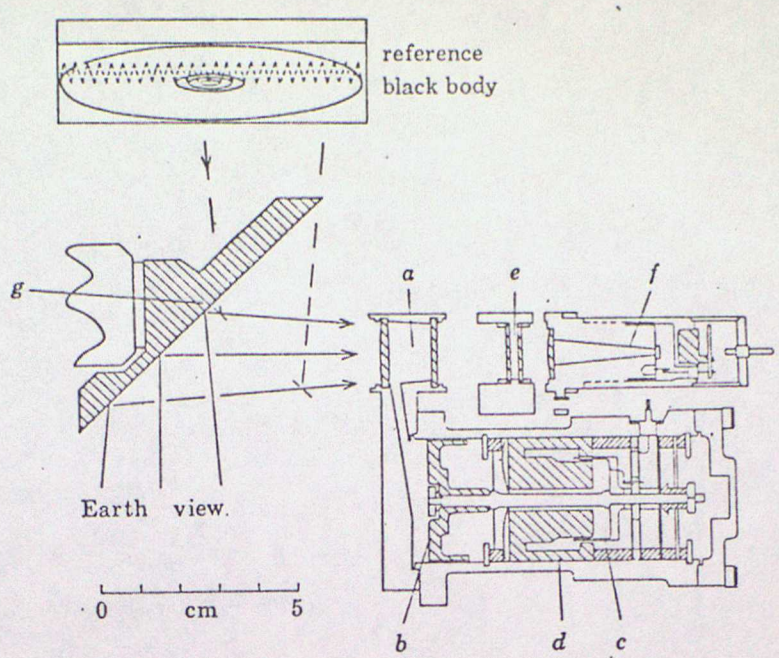

FIGURE 2. The optical system and pressure modulator of a stratospheric sounding unit. *a*, Absorption cell; *b*, piston; *c*, drive coil; *d*, magnet; *e*, interference filter; *f*, detector; *g*, scan mirror. Another two optical channels share the scan mirror.

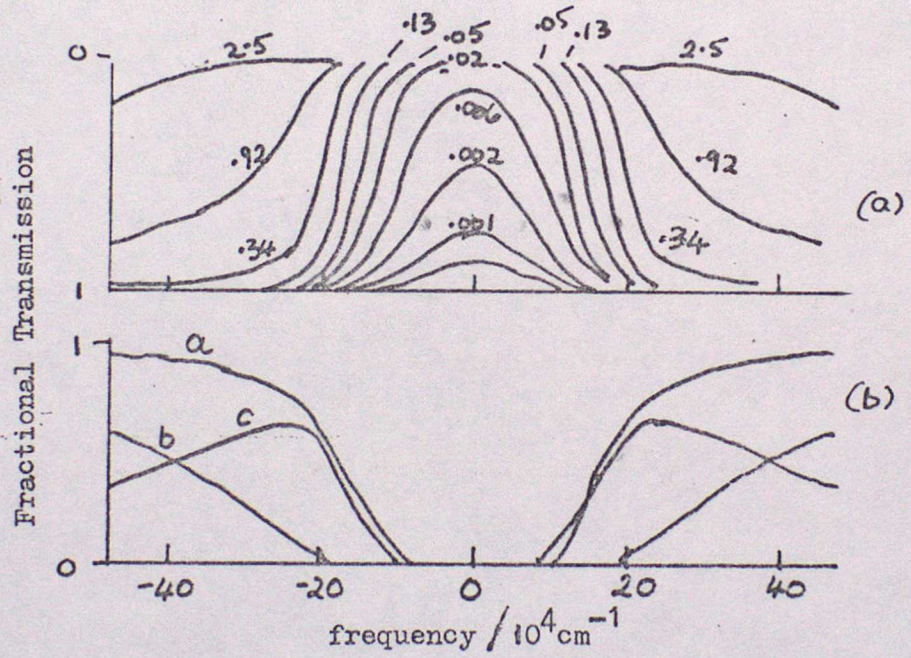

Figure 3 Illustrating the technique of pressure modulation applied to a single line (strength 2 cm^{-1} (atm $cm)^{-1}$ ν_2 CO_2)

(a) Transmission plotted against frequency for various vertical atmospheric paths from level of pressure p in millibars to the top of the atmosphere for a single line.

(b) Transmission of a pressure modulator all 1 cm long for same line as (a). Cell pressure is 5 millibars for curve a, 14 mbars for curve b and difference curve c.

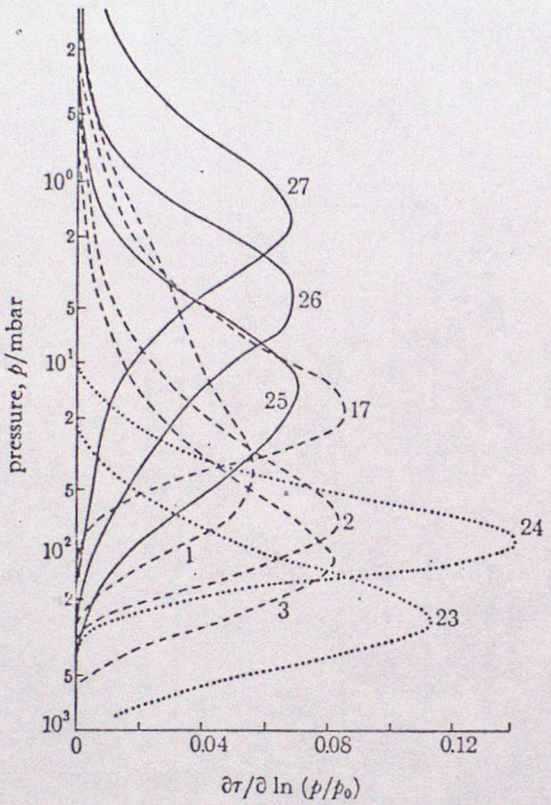

FIGURE 4. Weighting functions for those channels used for stratospheric analysis. The labels indicate the channel designations within the Tiros operational vertical sounder. The associated instruments are: ——, stratospheric sounding unit; ...., microwave sounding unit; --, high-resolution infrared sounder.

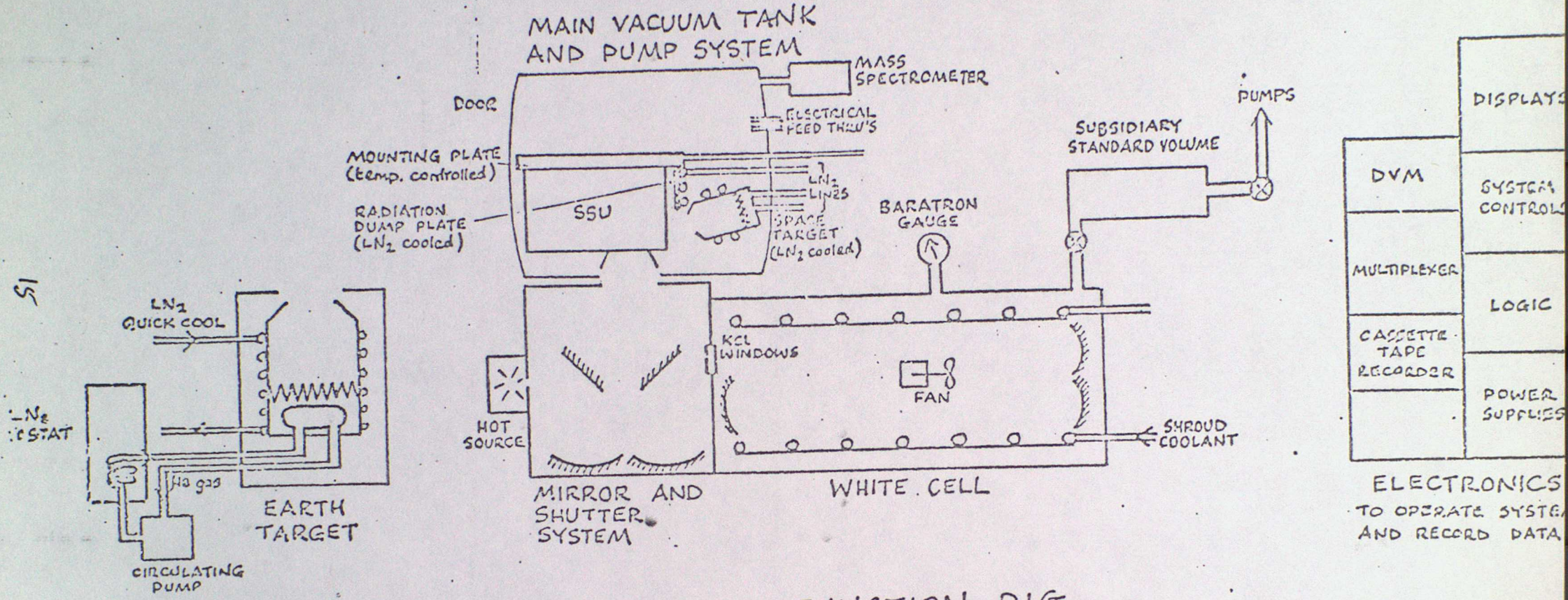

WEIGHTING FUNCTION RIG

FIG. 5 THE SSU CALIBRATION FACILITIES.

THE MAIN VACUUM TANK AND PUMPING SYSTEM CAN BE MOVED FROM THE WEIGHTING FUNCTION RIG TO THE EARTH TARGET. THE AREA AROUND THE TANK DOOR IS ENCLOSED IN A POLYTHENE TENT WITH A FILTERED AIR SUPPLY. WHEN USING A COMPLETE SSU, A DCU WILL ALSO BE NEEDED.

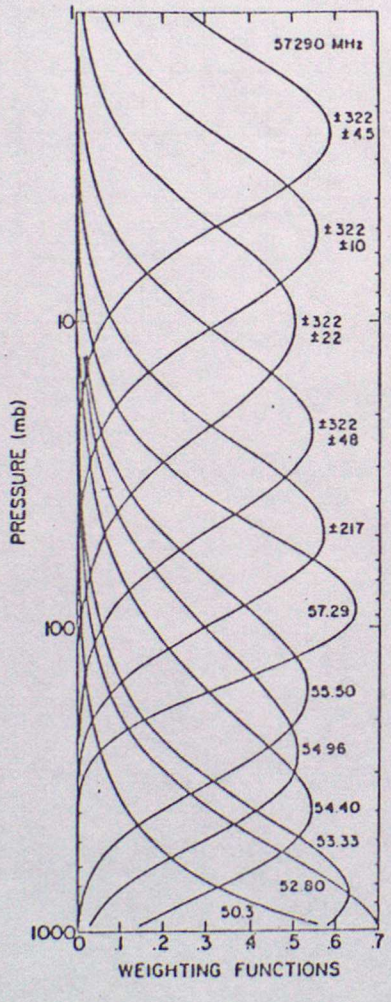

Figure 6a. Temperature weighting functions, channels 4-15.

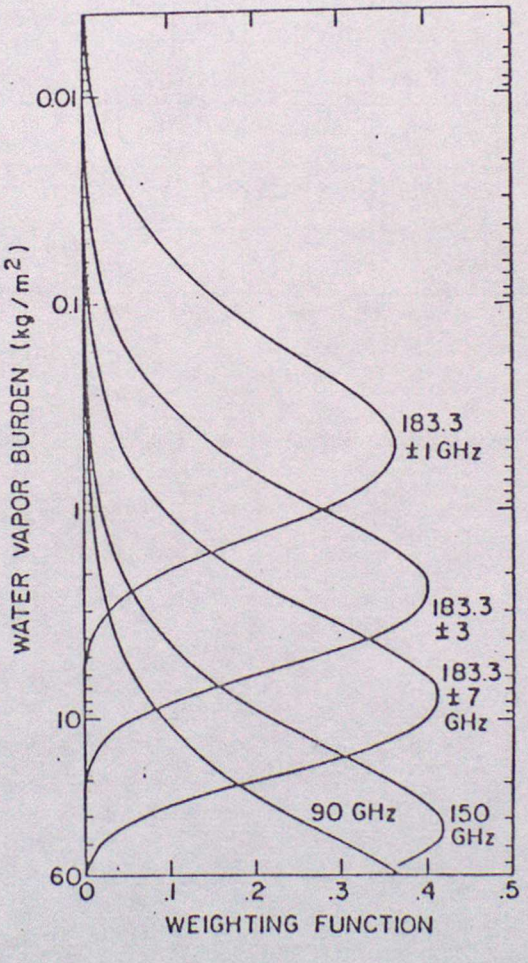

Figure 6b Water vapor burden weighting functions, channels 16-20.

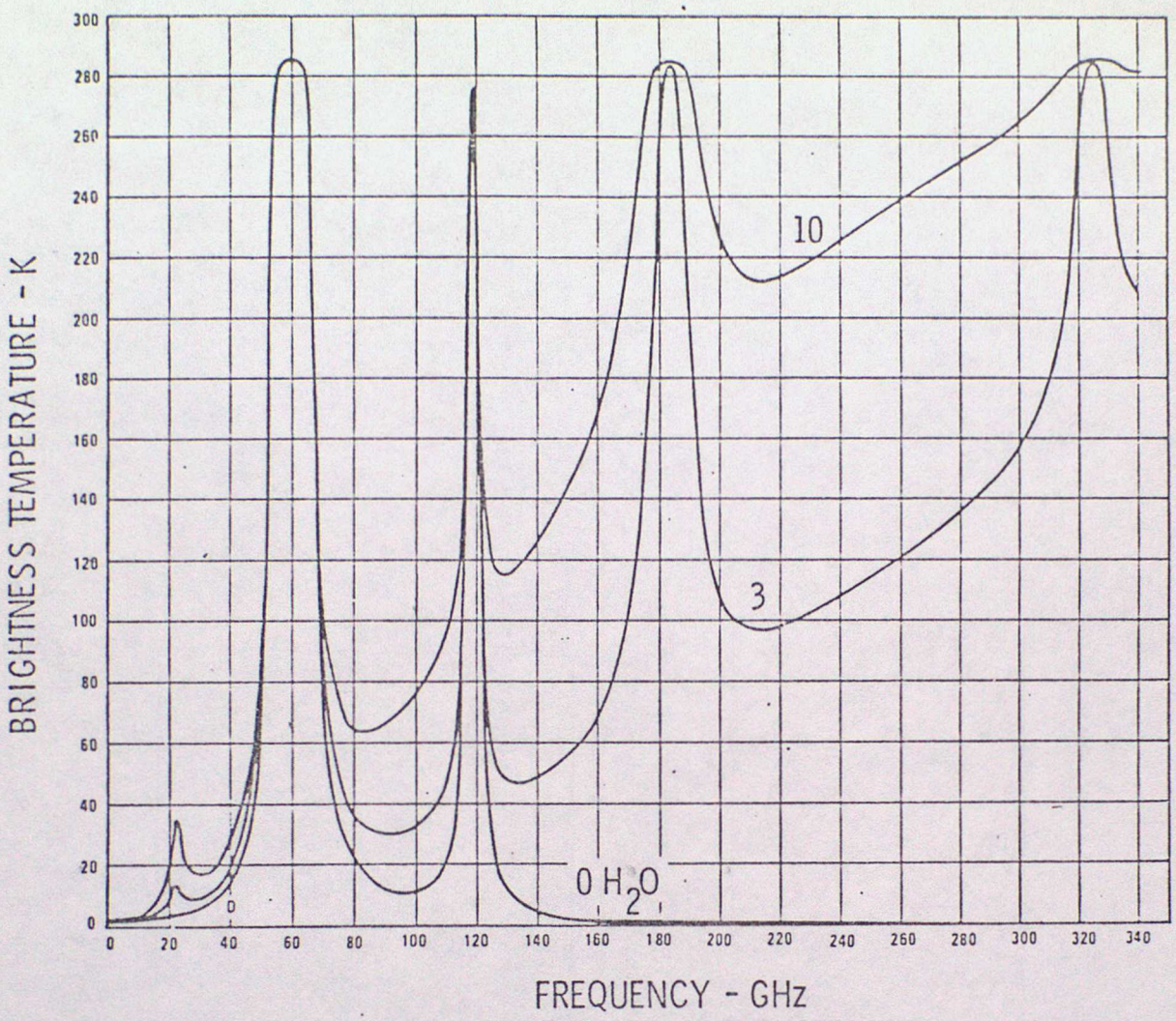

Fig. 7 Zenith brightness temperature for 0, 3, and 10 g/m^3 surface water vapor (2-km scale height) added to the U.S. Standard Atmosphere, 1976 (surface temperature 288 K), 1–340 GHz.

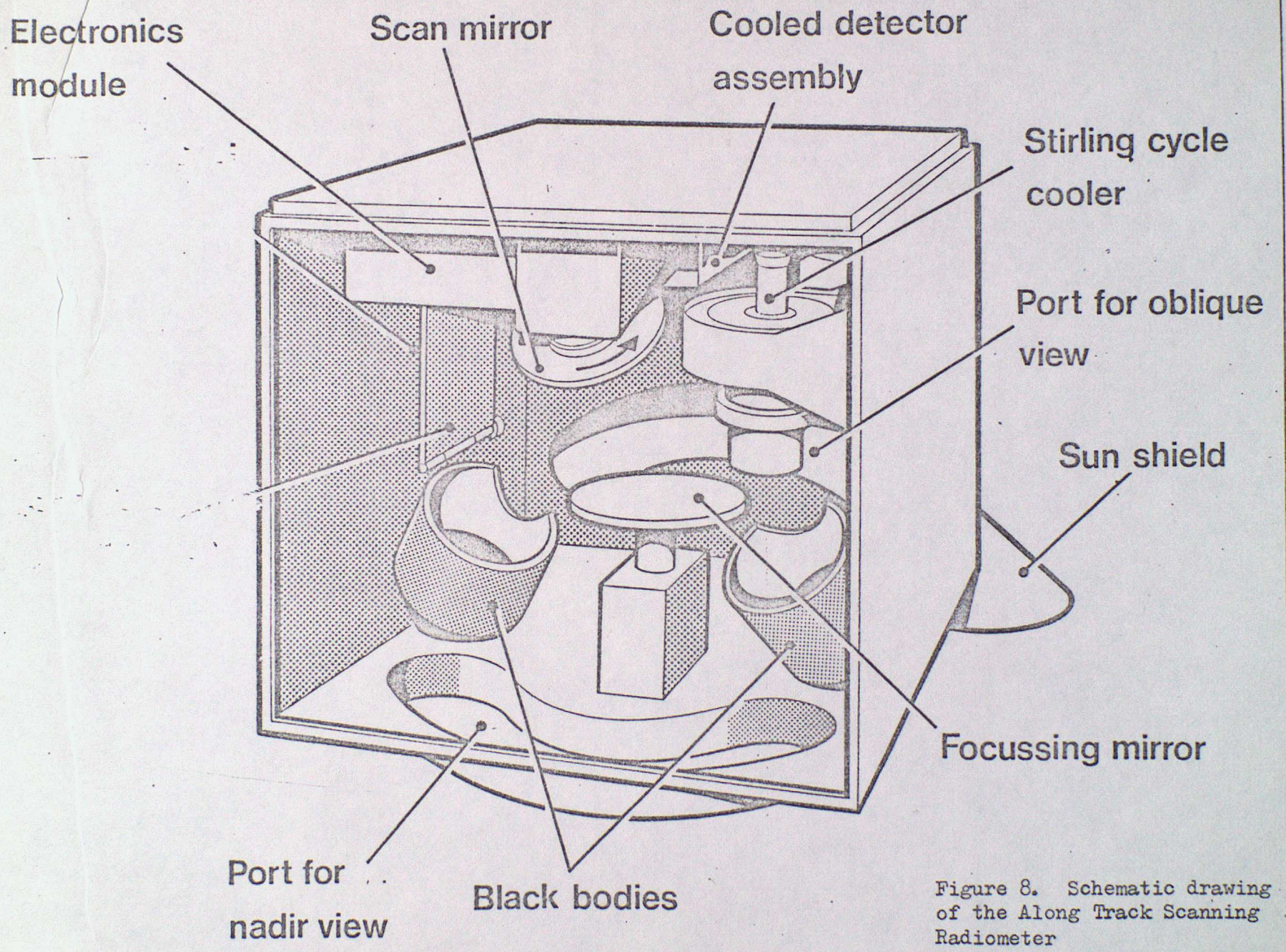

Figure 8. Schematic drawing of the Along Track Scanning Radiometer

ADVANCED LECTURES - SATELLITE METEOROLOGY - 1984

LECTURE 4: THE RETRIEVAL OF ATMOSPHERIC TEMPERATURE AND HUMIDITY FROM SATELLITE MEASUREMENTS OF RADIATION

by J.R.Eyre

1. Introduction

We have seen in lecture 2 that the intensity of radiation emitted from the top of the atmosphere varies with wavelength and is a function of the temperature and composition structure. Atmospheric sounding instruments measure radiation over a number of spectral intervals or "channels" at wavelengths chosen such that most of the radiation detected has been emitted by the atmosphere itself. Measurements of emission from gases of known concentration such as carbon dioxide and oxygen can be used to retrieve atmospheric temperature. Alternatively, if the temperature structure is known, information on the variable concentration profiles of constituents such as water vapour can be deduced from measurements at the wavelengths of the appropriate absorption bands. The channels used by the present TIROS Operational Vertical Sounder (TOVS) instruments on the TIROS-N satellite series are given in table 1 and typical weighting functions for them are shown in figure 1.

The theory presented in lecture 2 allows us to calculate the emitted radiance given the state of the atmosphere (and underlying surface). In interpreting satellite measurements we are faced with the INVERSE PROBLEM, i.e. given the measured radiances, we have to estimate the atmospheric state. For sounding systems using infra-red measurements, the retrieval problem is usually divided into 2 major stages:

(a) allowing for the effects on the radiances of cloud,

(b) using the cloud-free or "cloud-cleared" radiances to deduce the temperature and humidity profiles.

In this lecture we shall consider the theoretical aspects of (b). Lecture 5 will discuss both (a) and (b) in the context of one practical retrieval scheme.

There is a extensive literature on the theory of inverse problems in general and temperature retrieval in particular. An excellent discussion of the problem and literature review is given by Rodgers (1976). Hayden (1978) and Twomey (1977) also give useful introductions to the subject.

2. Temperature retrieval: characteristics of the inverse problem

Using the theory developed in lecture 2, we can express the radiance measured by the ith channel of a satellite-borne radiometer as:

$$R_i = (I_o)_i \, \bar{\tau}_i(z_o) + \int_{z_o}^{\infty} \bar{B}_i(z) \, K_i(z) \, dz \, . \qquad \ldots 2.1$$

Here we have chosen scale height, z = -ln(pressure), as the vertical co-ordinate (with z_o as the surface value), and we have used mean quantities averaged over the spectral response of the radiometer channel: $\bar{\tau}_i(z)$ is the mean transmittance from z to space for the ith channel, and $K_i(z)$ is the corresponding weighting function ($= d\bar{\tau}_i(z)/dz$). $B_i(z)$ is a Planck function slightly modified so as to represent the mean Planck function for the spectral response of the channel, and $(I_o)_i$ is the surface radiance evaluated in a similar manner. The approximations involved in the representation of this polychromatic problem by an equation in the form of the monochromatic problem usually produce negligible error.

For numerical solution of the problem it is more convenient to replace the integral equation by a vector formulation:

$$R_i = \underline{K}_i \cdot \underline{B} \, . \qquad \ldots 2.2$$

Here we have expressed the atmosphere's vertical temperature profile at a finite number of pressure levels and represented it by the corresponding Planck function vector, $\underline{B}$. $\underline{K}_i$ is the weighting function vector, the elements of which represent the layers centred on the levels at which $\underline{B}$ is expressed. $\underline{B}$ and $\underline{K}_i$ are vectors of length, J, the number of levels. The surface term has been absorbed as the first element of each vector. J must be sufficiently large for accurate approximation of an integral by a vector equation.

Equation 2.2 refers only to one channel. For a radiometer with I channels we can write,

$$\underline{R} = \underline{\underline{K}} \cdot \underline{B} \, , \qquad \ldots 2.3$$

where $\underline{R}$ is a vector of length I,
$\underline{B}$ is a vector of length J,
and $\underline{\underline{K}}$ is a matrix, J x I, containing the discrete weighting functions for all channels.

An important property of equation 2.3 (for the temperature sounding problem) is its degree of linearity. $\underline{B}$ is related in a known way to the unknown variable, i.e. the temperature profile, whilst $\underline{\underline{K}}$ is only weakly dependent on temperature. This allows us to use linear inverse theory successfully. The linearity of the problem is usually improved further by expressing the radiances and Planck functions as deviations from mean values:

$$\underline{r} = \underline{R} - \bar{\underline{R}} \quad \text{and} \quad \underline{b} = \underline{B} - \bar{\underline{B}} \, .$$

$$\therefore \quad \underline{r} = \underline{\underline{K}} \cdot \underline{b} \, . \qquad \ldots 2.4$$

One further problem which must be tackled in practice concerns the nature of the function $\underline{b}$. Unless all channels are very close in wavenumber, we have a set of significantly different functions and we cannot solve for a single vector $\underline{b}$. There are several approaches to this problem. The one usually adopted for TOVS, which has temperature sounding channels in 3 widely separated spectral regions (the 15μm CO_2 band, the 4.3μm CO_2 band and the 50-60 GHz O_2 band), is to convert radiances to equivalent black body temperatures (often called "brightness temperatures") and to derive the atmospheric temperature profile rather than the Planck function profile. Using 1st order Taylor expansions we can write,

$$r_i = \frac{dR_i}{dT_{B_i}} t_{B_i} \quad \text{and} \quad b_j = \frac{dB_j}{dT_j} t_j , \qquad \ldots 2.5$$

where T_{B_i} is the brightness temperature of the ith channel,
t_{B_i} is its deviation from the mean,
T_j is the temperature at the jth pressure level,
and t_j is its deviation from the mean.

We can now re-write equation 2.4 as

$$\underline{t_B} = \underline{\underline{K'}} \cdot \underline{t} , \qquad \ldots 2.6$$

where $K_{ij} = K'_{ij} (dB_j/dT_j) / (dR_i/dT_i)$. This formulation is not quite as linear as equation 2.4 because of the nature of $\underline{\underline{K'}}$, but it yields an expression in which there is a single unknown vector, $\underline{t}$, independent of the radiometer.

The fundamental difficulties of the retrieval problem can be seen by examining equation 2.4 or 2.6; we have I measurements of radiance and we wish to obtain a profile at J atmospheric levels. Usually J > I, giving an under-constrained problem and an infinite number of solutions $\underline{t}$ which satisfy the measurements $\underline{t_B}$. Referring back to equation 2.1 we see that we are really attempting to obtain the temperature profile, a continuous function of height, from a finite number of measurements. Our task is to find, from the infinite number of solutions, an acceptable solution and, if possible, the most probable solution. This involves constraining the solution using some *a priori* information which is equivalent to adding more equations to the problem so that we have at least as many equations as unknowns.

One obvious way of constraining the solution is to reduce the number of levels at which $\underline{t}$ is specified or to express $\underline{t}$ as a linear combination of a small number of pre-selected functions so that $J \leq I$. Neither of these simple approaches tends to work well in practice (see Rodgers, 1976). Briefly, problems arise in the mathematics of the inversion procedure. We are seeking a predictive equation of the form,

$$\underline{t} = \underline{\underline{D}} \cdot \underline{t_B} . \qquad \ldots 2.7$$

The matrices $\underline{\underline{D}}$ obtained by the simple methods suggested above tend to have elements which oscillate from large positive to large negative values. Consequently any small errors in $\underline{t_B}$ are amplified into unacceptably large errors in $\underline{t}$. This instability arises because the weighting functions overlap significantly and we do not have I independent observations. Since $\underline{t_B}$ will always contain a contribution from instrumental noise, successful inversion methods must overcome

this kind of instability.

3. Practical inversion methods for temperature retrieval

Numerous schemes have been devised for retrieving temperature profiles from satellite sounding data. In this section we examine 2 types of approach in common use.

3.1 Minimum variance method (regression)

This method recognises that there is insufficient information in the measured brightness temperatures, $\underline{t}_B$, for us to retrieve the exact, true temperature profile, $\underline{t}$. It does not attempt to find $\underline{t}$ but seeks a estimate profile, $\hat{\underline{t}}$, using a linear predictive equation,

$$\hat{\underline{t}} = \underline{\underline{D}} \cdot \underline{t}_B \quad . \qquad \ldots 3.1$$

$\underline{\underline{D}}$ is a predictive matrix calculated such that the variance of $\hat{\underline{t}}$ from $\underline{t}$ is a minimum when averaged over a large number of profiles, M, i.e.

$$\sum_{m=1}^{M} (\underline{t}_m - \hat{\underline{t}}_m)^T \cdot (\underline{t}_m - \hat{\underline{t}}_m) \qquad \ldots 3.2$$

is minimised with respect to all elements of $\underline{\underline{D}}$. (^{T} denotes matrix transpose.)

This procedure leads to the well-known multiple linear regession relation:

$$\underline{\underline{D}} = (\underline{\underline{t}} \cdot \underline{\underline{t}}_B^T) \cdot [\underline{\underline{t}}_B \cdot \underline{\underline{t}}_B^T]^{-1} \qquad \ldots 3.3$$

where $\underline{\underline{t}}$ is a matrix of dimension M x J containing M profiles specified at J levels,
$\underline{\underline{t}}_B$ is a matrix of dimension M x I containing the corresponding M brightness temperature vectors for J channels,
and $[\ldots]^{-1}$ denotes a matrix inverse.

$(\underline{\underline{t}}_B \cdot \underline{\underline{t}}_B)/M$ is the brightness temperature covariance matrix and $(\underline{\underline{t}} \cdot \underline{\underline{t}}_B)/M$ the covariance of temperature profile with brightness temperature. Thus there is a strong constraint on the inversion which enters the problem through the covariance matrices representing the statistical properties of atmospheric profile variations and the related statistics for the radiances measured at the satellite.

The minimum variance solution is discussed by Rodgers (1976) and shown to be identical to the "maximum probability" solution for sets of profiles with Gaussian statistics.

In practice there are several possible ways of generating the predictive matrix, $\underline{\underline{D}}$:

(a) We may neglect all considerations of the physics involved and collect a large set of measured brightness temperatures, $\underline{\underline{t}}_B$, collocated with a set of radiosonde profiles, $\underline{\underline{t}}$, and hence derive $\underline{\underline{D}}$. This is the basis of the method currently used by NOAA/NESDIS

for the operational scheme which generates global soundings. The same coefficients are also used at present by Met.O.19 for routine generation of high-resolution regional retrievals (see lecture 5). The method was first developed in the simple form given here (Smith et al., 1970) but has been refined to use the coefficients of the eigenvectors of the temperature profile and brightness temperature covariance matrices rather than the vectors themselves (Smith and Woolf, 1976; Smith et al., 1979). This makes the inversion less sensitive to noise in the measurements.

(b) From equation 2.6 we can write a measured brightness temperature vector as

$$\underline{t}_B = \underline{\underline{K}}' \cdot \underline{t} + \underline{\epsilon} \qquad \ldots 3.4$$

where $\underline{\epsilon}$ represents random measurement error. Substituting equation 3.4 into equation 3.3, we obtain

$$\underline{\underline{D}} = \left\{ \underline{t} \cdot \left(\underline{\underline{K}}' \cdot \underline{t} + \underline{\epsilon} \right)^T \right\} \cdot \left[\left(\underline{\underline{K}}' \cdot \underline{t} + \underline{\epsilon} \right) \cdot \left(\underline{\underline{K}}' \cdot \underline{t} + \underline{\epsilon} \right)^T \right]^{-1}$$

$$= \left\{ \underline{\underline{S}}_t \cdot (\underline{\underline{K}}')^T \right\} \cdot \left[\underline{\underline{K}}' \cdot \underline{\underline{S}}_t \cdot (\underline{\underline{K}}')^T + \underline{\underline{S}}_\epsilon \right]^{-1}, \qquad \ldots 3.5$$

where $\underline{\underline{S}}_t$ and $\underline{\underline{S}}_\epsilon$ are the covariance matrices of $\underline{t}$ and $\underline{\epsilon}$ respectively, and $\underline{\epsilon}$ is assumed to be uncorrelated with $\underline{t}$.

(c) Method (b) can only be applied satisfactorily if the problem is sufficiently linear for one set of weighting functions $\underline{\underline{K}}'$ to be applied to all profiles. Because $\underline{\underline{K}}'$ is in practice weakly dependent on temperature, it is preferable to apply an accurate radiative transfer model to each profile $\underline{t}$ and generate theoretically the corresponding brightness temperature vector, $\underline{t}_B$. Thus we obtain a set of profiles $\underline{t}$ and their corresponding synthetic brightness temperatures $\underline{t}_B$, from which $\underline{\underline{D}}$ may be found as in method (a).

The advantage of method (c) over method (a) is that we can select carefully from a historical radiosonde data-base a set of profiles representative of the statistical behaviour of the atmosphere. Also the synthetic radiances do not have contributions from collocation errors as they do in method (a).

Method (a) is a purely statistical approach, whereas methods (b) and (c) are mixed physical-statistical techniques. They all have the advantage that they are computationally fast (since the $\underline{\underline{D}}$ matrices may be pre-computed) and take advantage of existing knowledge about atmospheric statistics. On the other hand, the profiles from which the statistics are derived must be chosen with care; inappropriate statistics lead to poor results. For example, statistics based on tropical profiles will give large errors when used to retrieve profiles typical of higher latitudes. Similarly, seasonal dependence of statistics must be carefully considered. Another problem with the regression approach concerns the nature of the retrieved profile. The statistical data-base (particularly in mid-latitudes) will generally contain profiles of distinct and widely differing shape. In representing these profiles by a single covariance matrix, we usually lose the sense of these different shapes, and the retrieved profiles,

whilst being optimum in the minimum variance sense, will tend to have shapes which are smoother than those which actually exist in the atmosphere.

3.2 Physical methods

Several "direct", "empirical" or "physical" methods, which do not use atmospheric statistics are to be found in the literature. The iterative relaxation method, introduced by Chahine (1968) and reformulated by Smith (1970), is an example. In Smith's method the brightness temperatures $\underline{T}_{B_0}$, corresponding to a first-guess profile $\underline{T}_0$, are calculated using a radiative transfer model. Then the profile at the jth level is adjusted according to the difference between the measured brightness temperatures $\underline{T}_{B_M}$ and the calculated brightness temperatures $\underline{T}_{B_0}$ using the weighting function values at the jth level as relative weights:

$$(T_1)_j = (T_0)_j + \frac{\sum_{i=1}^{I} K'_{ij} \left\{ (T_{B_M})_i - (T_{B_0})_i \right\}}{\sum_{i=1}^{I} K'_{ij}} \qquad \ldots 3.6$$

From $\underline{T}_1$, the equivalent brightness temperatures are computed and the process repeated. The iteration proceeds to a solution $\underline{T}_n$ at the nth step, when the difference between measured and calculated brightness temperatures meets some criterion (related to instrument noise).

The a priori constraints in this method are not obvious but are effectively introduced in equation 3.6 through the implicit assumption that the temperature profile change at each step must be a linear combination of the weighting functions. In common with similar direct methods, a solution is obtained which may not be the most probable solution in the statistical sense. Also it is found that the solution is often sensitive to the first-guess profile, $\underline{T}_0$, particularly with respect to the shape of the profile. For example, with retrievals from data of current operational instruments, the tropopause height assumed in the first guess will tend to be altered little by the iterative procedure. A good first guess from a forecast model will yield a good solution, but the advantage of this must be weighed carefully against the desirability of obtaining retrieval errors uncorrelated with those of the forecast model.

The strength of physical methods lies in their ability to include the physics of the radiative transfer problem directly. Non-linearities are treated explicitly as are problems caused by the effects of high terrain or variable surface emissivity, which are difficult to handle in a regression scheme. These advantages are obtained at the expense of computation time, since radiative transfer calculations are required as part of the retrieval algorithm. This is not true of regression schemes (see figure 2).

A draw-back common to both physical and physical-statistical schemes is that they involve theoretical calculations of radiance, and hence they propagate errors in our knowledge of the spectroscopy into the solution. This problem can be tackled fundamentally by research to improve our understanding of the molecular spectroscopy involved in the calculations of transmittance. In the short term it can be treated reasonably well by making empirical corrections to the transmittance models to minimise differences between measured radiances and those calculated theoretically from collocated

radiosonde data.

To summarise, it can be seen that statistical and physical methods have different strengths and weaknesses. It would appear therefore that the best results ought to be obtained using a combined approach which seeks to use all the available information — the radiance measurements and our knowledge of both the physics of the problem and the statistical behaviour of the atmosphere.

4. Humidity retrieval

By comparison with the temperature retrieval problem, humidity retrieval has received little attention. This reflects not only the relative importance of the 2 parameters in numerical forecasting but also the additional difficulties which arise in the case of humidity retrieval. Also errors in the temperature retrieval tend to propagate into the humidity retrieval and so it is sensible to give priority to the former.

The global operational retrieval scheme currently used by NOAA/NESDIS and Met.O.19's present system take a rather simplistic approach to the problem of humidity retrieval. By analogy with the linear regression scheme used for temperature retrieval (section 3.1(a) above), they use a regression of measured brightness temperatures against collocated humidity mixing ratio profiles and obtain a predictive matrix $\underline{\underline{D}}'$ to be used in the retrieval as follows:

$$\hat{\underline{c}} = \underline{\underline{D}}' \cdot \underline{t}_B \quad , \qquad \ldots 4.1$$

where $\hat{\underline{c}}$ is a vector representing the minimum variance estimate of the water vapour mixing ratio profile (or rather its deviation from a mean profile).

It is accepted that there is a theoretical weakness in this approach. In using a linear regression retrieval we imply that the forward problem can be expressed as a linear equation, i.e. by anology with equation 2.1 we are assuming an expression for the radiance measured by a water vapour sounding channel of the form,

$$R_i = (I_o)_i \, \bar{\tau}(z_o) + \int_{z_o}^{\infty} c(z) \, G(z) \, dz \quad , \qquad \ldots 4.2$$

where $c(z)$ is the humidity profile (in terms of mixing ratio or any other suitable humidity parameter) and $G(z)$ is a weighting function which is only weakly dependent on $c(z)$.

In fact it is not possible to derive such a formulation. This is because $c(z)$ enters the radiative transfer equation through the monochromatic transmittance:

$$\tau_\nu(z) = \exp\left\{ - \int_z^{\infty} k_\nu(z') \, \rho(z') \, c(z') \, dz' \right\} \quad , \qquad \ldots 4.3$$

where $k_\nu(z)$, $c(z)$ and $\rho(z)$ are the profiles of absorption coefficient, mixing ratio and atmospheric density respectively. The weighting functions are consequently strongly dependent on the unknown variable,

c(z). The effect of increasing the humidity in the atmosphere is to decrease the transmittance from any level to space. Since the "temperature weighting function" has the form, $K(z) = d\tau(z)/dz$, the peak of this function will rise as the humidity increases, and so the layer from which we measure the radiation is a function of the variable profile we wish to measure. Consequently we have a very non-linear problem and it is perhaps surprising that retrievals based on equation 4.1 are as acceptable as they prove to be. Nevertheless we can argue on theoretical grounds that by treating the problem as a non-linear one, we should be able to improve significantly on the linear approach represented by equation 4.1. Several algorithms have been developed for humidity profile retrieval. An extensive bibliography on the subject has been compiled by Rosenberg et al. (1983).

The non-linear nature of the problem suggests that a physical retrieval will have advantages over a linear, statistical method. An example of the physical approach is given by Smith and Woolf (1981), who develop an algorithm of the form of equation 3.6 to solve iteratively for u_j, the water vapour overburden above pressure level j. u_j is related to the mixing ratio profile as follows:

$$u_j = \int_{z_j}^{\infty} c(z)\,\rho(z)\,dz = \int_{p_j}^{0} -\,c(p)\,\frac{dp}{g}\,, \qquad \ldots 4.4$$

and so, if required, c(p) can be found by differentiation of the u profile.

A different approach, which provides a theoretical basis for the use of atmsopheric statistics in a linear manner, has been developed by Rosenkranz et al. (1982). Returning to equation 2.1, we can integrate the atmospheric term over any convenient vertical co-ordinate. Noting that the usual co-ordinate, pressure, can be thought of as "mass overburden", for humidity retrieval we can change from pressure to water vapour overburden and thus obtain a term,

$$\int B\{T(u)\}\,K(u)\,du\,. \qquad \ldots 4.5$$

For a water vapour sounding channel the transmittance to space, $\tau(u)$, from a level above which there is a given water vapour overburden, u, is fairly constant and is only a weak fuction of temperature. Since $K(u) = d\tau(u)/du$, it also is only weakly temperature-dependent, and so we have a temperature retrieval problem with the same properties as that discussed in section 2. The only difference is that we are using water vapour sounding channels to estimate the temperature profile, T(u), at levels of constant u. Hence, if we also have T(p), from a retrieval based on temperature sounding channels, we may combine the two to find u(p) as illustrated in figure 3. As explained above, the mixing ratio profile may be found in principle by differentiation of the u(p) profile. In practice it is found more satisfactory to use a regression relation to derive c(p) from u(p).

A fundamental problem with humidity retrieval concerns the sensitivity of satellite measurements to low level water vapour. If the surface emissivity is high, as for microwave measurements over land or infra-red measurements over land and sea, there is usually little difference between the brightness temperature of the surface and the temperature of the lower layers of the atmosphere.

Consequently, if we consider the effects of increasing the humidity in the lower layers on the radiation emanating from the top of these layers, the extra emission from the increased water vapour is almost exactly compensated by increased absorption of upwelling radiation from below. This means that the satellite measurements are relatively insensitive to humidity of layers close in temperature to the surface. This problem is perhaps the major limitation on the accuracy and utility of current humidity retrievals, particularly when we note that most of the water vapour in an atmospheric column is in the lower layers. It is ameliorated in the case of microwave measurements over the sea, where the surface emissivity is sufficiently low for there to be a large contrast between surface brightness temperature and atmospheric temperature in the lower layers.

The discussion so far has concentrated on the retrieval of humidity profiles. To obtain a profile we need multi-channel information; from a single humidity sounding channel of a radiometer it is only possible to retrieve one piece of information, such as the mean humidity of the layer from which the radiation is coming. This approach has been used to derive mean layer relative humidity from Meteosat water vapour (6.5μm) channel data (Meteosat System Guide, 1980; Eyre, 1980) and for the 3 humidity sounding channels of the GOES VISSR Atmospheric Sounder (VAS) used independently for 3 atmospheric layers (Smith and Zhou, 1982). It is advisable to retrieve relative humidity rather than other humidity parameters because it is the least sensitive to errors in the assumed temperature profile.

Also of interest is the total precipitable water of the atmosphere. This can be obtained most accurately using "window" channels which are principally surface-sensing channels and have a relatively small contribution from atmospheric emission. However the atmospheric component of the radiation they measure is often closely related to the total water vapour in the column. Using brightness temperatures in 2 or more window channels with different absorption characteristics, we can set up regression relations to retrieve both surface temperature (lecture 8) and total water content (see, for example, Chesters et al., 1982).

REFERENCES

Chahine M.T.
J.Opt.Soc.Amer., 58, 1634-1637 (1968).
Determination of the temperature of an atmosphere from its outgoing radiance.

Chesters D., Uccellini L.W., Robinson W.
NASA Technical Memorandum, TM 83951 (1982).
Low-level water vapour fields from VISSR Atmospheric Sounder (VAS) split window channels at 11 and 12 microns.

Eyre J.R.
Proc.IAMAP Symp., Hamburg, August 1981 (ESA SP-165, 63-66, June 1981).
Direct use of Meteosat water vapour channel radiances to improve the humidity analysis in a forecast model.

Hayden C.M.
WMO Technical Note No. 166 (1979).
Quantitative meteorological products from satellites. Chapter 1: Remote soundings of temperature and moisture.

Meteosat System Guide
ESA publication (ESOC/MDMD) (1980).

Rodgers C.D.
Rev.Geophys.Sp.Phys., 14, 609-624 (1976).
Retrieval of atmospheric temperature and composition from remote measurements of thermal radiation.

Rosenberg A., Hutter E.C., Horan J.J.
Nav.Env.Pred.Rsch.Fac. Contract Report CR 83-01(b) (1983).
Satellite moisture retrieval techniques. Volume 2: Atmospheric sounding bibliography.

Rosenkranz P.W., Komichak M.J., Staelin D.H.
J.Appl.Meteor., 21, 1364-1370 (1982).
A method for estimation of atmospheric water vapour profiles by microwave radiometry.

Smith W.L.
Appl.Opt., 9, 1993-1999 (1970).
Iterative solution of the radiative transfer equation for the temperature and absorbing gas profile of an atmosphere.

Smith W.L., Woolf H.M.
J.Atmos.Sci., 33, 1127-1140 (1976).
The use of eigenvectors of statistical covariance matrices for interpreting satellite sounding radiometer observations.

Smith W.L., Woolf H.M.
Proc.4th Conf. on Atmospheric Radiation, 13-17, Toronto, June 1981.
Algorithms used to retrieve surface-skin temperature and vertical temperature and moisture profiles from VISSR Atmospheric Sounder (VAS) radiance observations.

Smith W.L., Woolf H.M., Hayden C.M., Wark D.Q., McMillin L.M.
Bull.Amer.Meteor.Soc., 60, 1177-1187 (1979).
The TIROS-N operational vertical sounder.

Smith W.L., Woolf H.M., Jacob W.J.
Mon.Wea.Rev., 98, 582-603 (1970).
A regression method for obtaining real time temperature and geopotential height profiles from satellite spectrometer measurements and its application to NIMBUS-3 SIRS observations.

Smith W.L., Zhou F.X.
Appl.Opt., 21, 924-928 (1982).
Rapid extraction of layer relative humidity, geopotential thickness and atmospheric stability from satellite sounding radiometer data.

Twomey S.
Elsevier Co. (1977).
Introduction to the mathematics of inversion in remote sensing and indirect measurements.

HIRS Channel number	Channel central wavenumber	Central wavelength (μm)	Principal absorbing constituents	Level of peak energy contribution	Purpose of the radiance observation
1	668	15.00	CO_2	30 mb	*Temperature sounding.* The 15-μm band channels provide better sensitivity to the temperature of relatively cold regions of the atmosphere than can be achieved with the 4.3-μm band channels. Radiances in Channels 5, 6, and 7 are also used to calculate the heights and amounts of cloud within the HIRS field of view.
2	679	14.70	CO_2	60 mb	
3	691	14.50	CO_2	100 mb	
4	704	14.20	CO_2	400 mb	
5	716	14.00	CO_2	600 mb	
6	732	13.70	CO_2/H_2O	800 mb	
7	748	13.40	CO_2/H_2O	900 mb	
8	898	11.10	Window	Surface	*Surface temperature* and cloud detection.
9	1 028	9.70	O_3	25 mb	*Total ozone* concentration.
10	1 217	8.30	H_2O	900 mb	*Water vapor sounding.* Provides water vapor corrections for CO_2 and window channels. The 6.7-μm channel is also used to detect thin cirrus cloud.
11	1 364	7.30	H_2O	700 mb	
12	1 484	6.70	H_2O	500 mb	
13	2 190	4.57	N_2O	1 000 mb	*Temperature sounding.* The 4.3-μm band channels provide better sensitivity to the temperature of relatively warm regions of the atmosphere than can be achieved with the 15-μm band channels. Also, the short-wavelength radiances are less sensitive to clouds than those for the 15-μm region.
14	2 213	4.52	N_2O	950 mb	
15	2 240	4.46	CO_2/N_2O	700 mb	
16	2 276	4.40	CO_2/N_2O	400 mb	
17	2 361	4.24	CO_2	5 mb	
18	2 512	4.00	Window	Surface	*Surface temperature.* Much less sensitive to clouds and H_2O than the 11-μm window. Used with 11-μm channel to detect cloud contamination and derive surface temperature under partly cloudy sky conditions. Simultaneous 3.7- and 4.0-μm data enable reflected solar contribution to be eliminated from observations.
19	2 671	3.70	Window	Surface	
20	14 367	0.70	Window	Cloud	*Cloud detection.* Used during the day with 4.0- and 11-μm window channels to define clear fields of view.

MSU	Frequency (GHz)	Principal absorbing constituents	Level of peak energy contribution	Purpose of the radiance observation
1	50.31	Window	Surface	*Surface emissivity* and *cloud attenuation* determination.
2	53.73	O_2	700 mb	*Temperature sounding.* The microwave channels probe through clouds and can be used to alleviate the influence of clouds on the 4.3- and 15-μm sounding channels.
3	54.96	O_2	300 mb	
4	57.95	O_2	90 mb	

SSU	Wavelength (μm)	Principal absorbing constituents	Level of peak energy contribution	Purpose of the radiance observation
1	15.0	CO_2	15.0 mb	*Temperature sounding.* Using CO_2 gas cells and pressure modulation, the SSU observes thermal emissions from the stratosphere.
2	15.0	CO_2	4.0 mb	
3	15.0	CO_2	1.5 mb	

Table 1.

Characteristics of TIROS Operational Vertical Sounder (TOVS) channels

From Smith et al., 1979

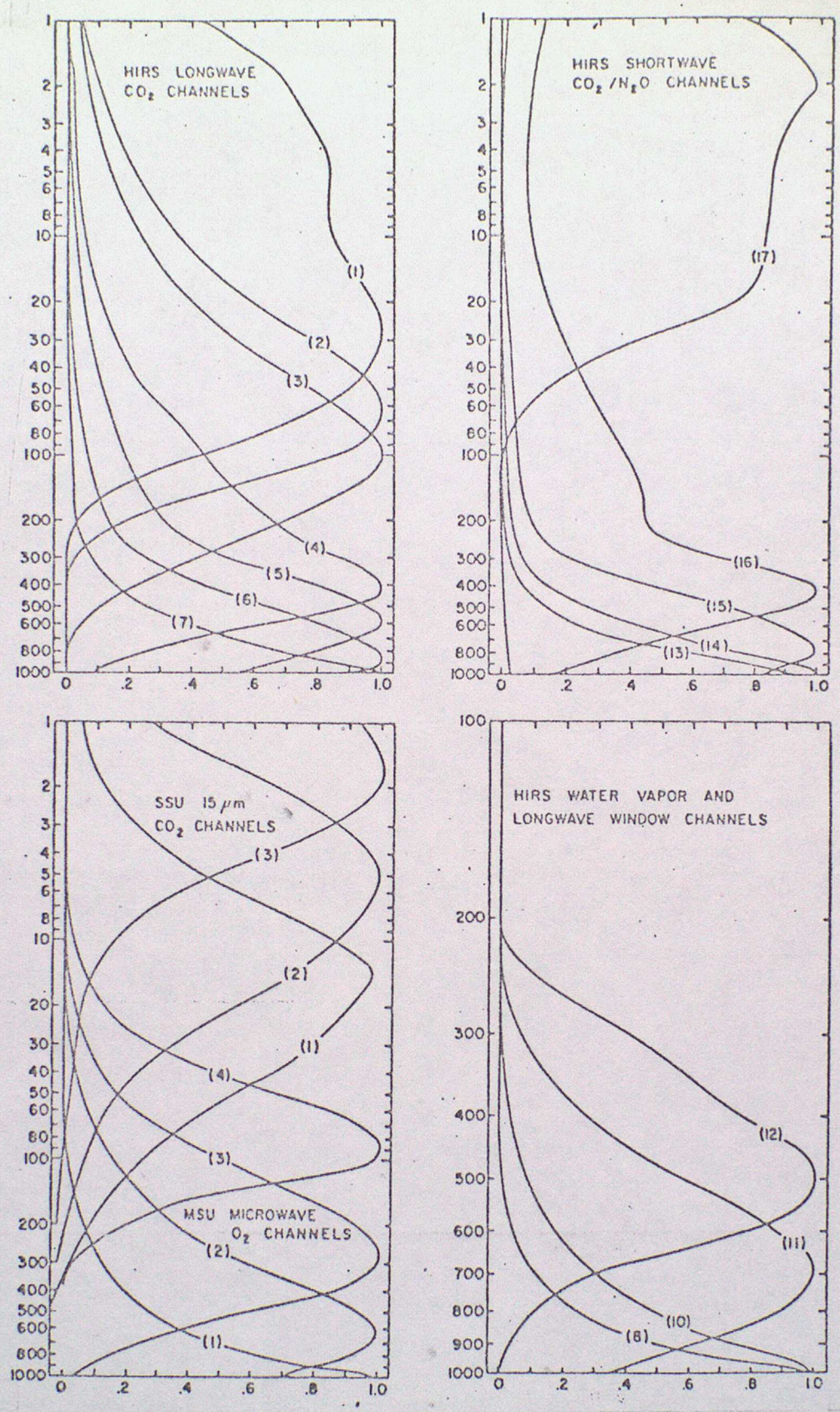

Figure 1

TOVS weighting functions

from Smith et al., 1979

FIGURE 2. SCHEMATIC REPRESENTATION OF REGRESSION AND PHYSICAL RETRIEVALS

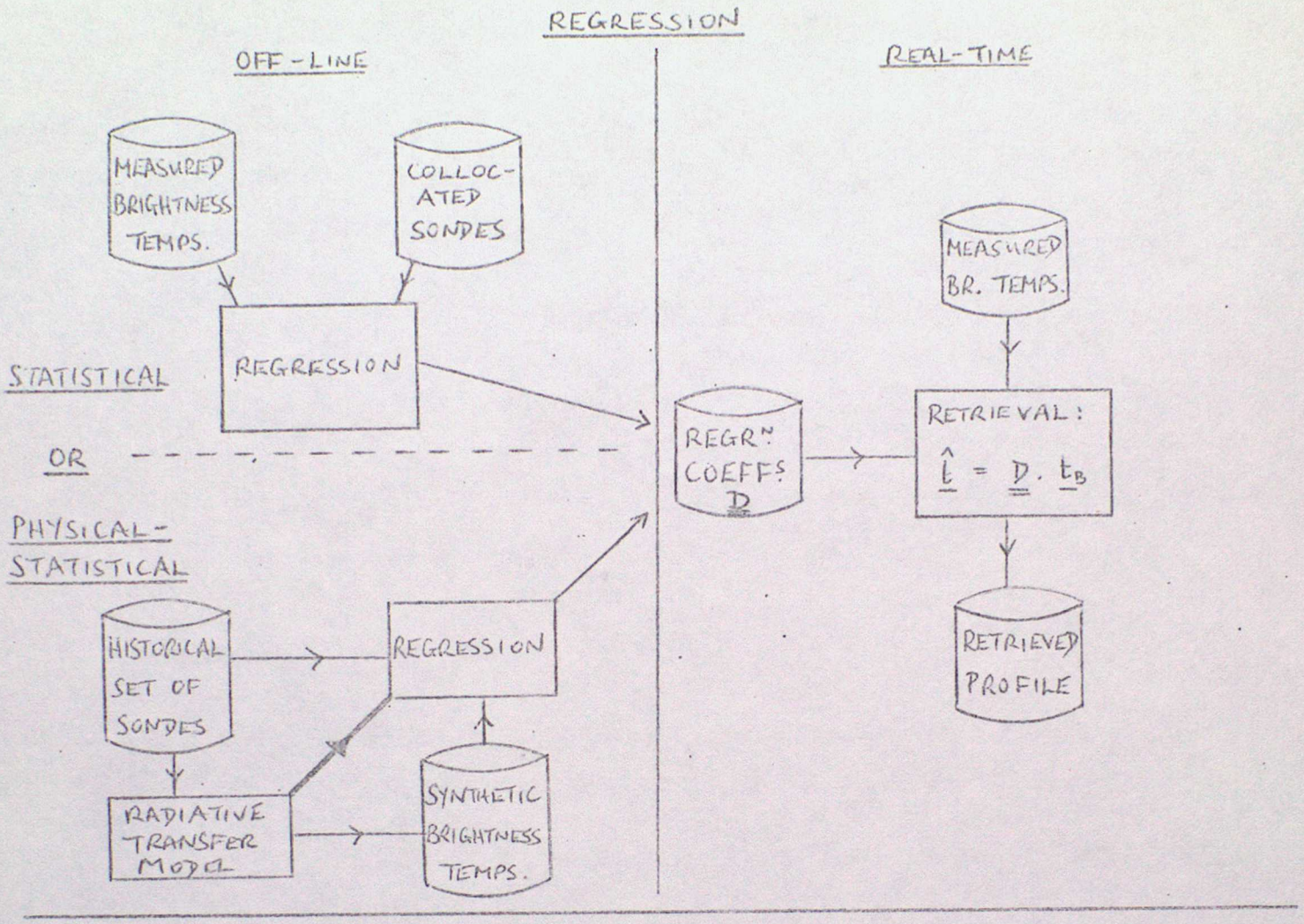

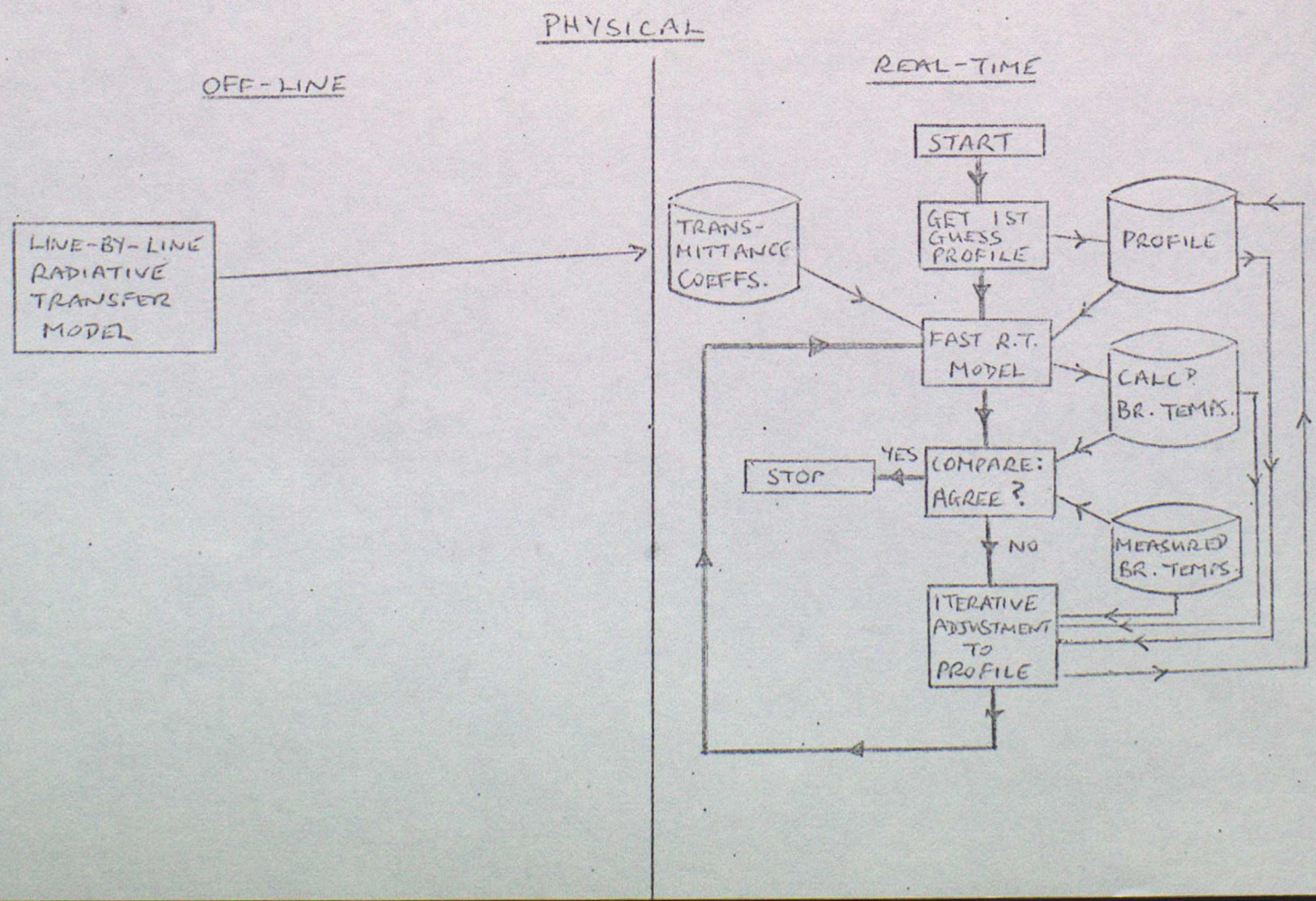

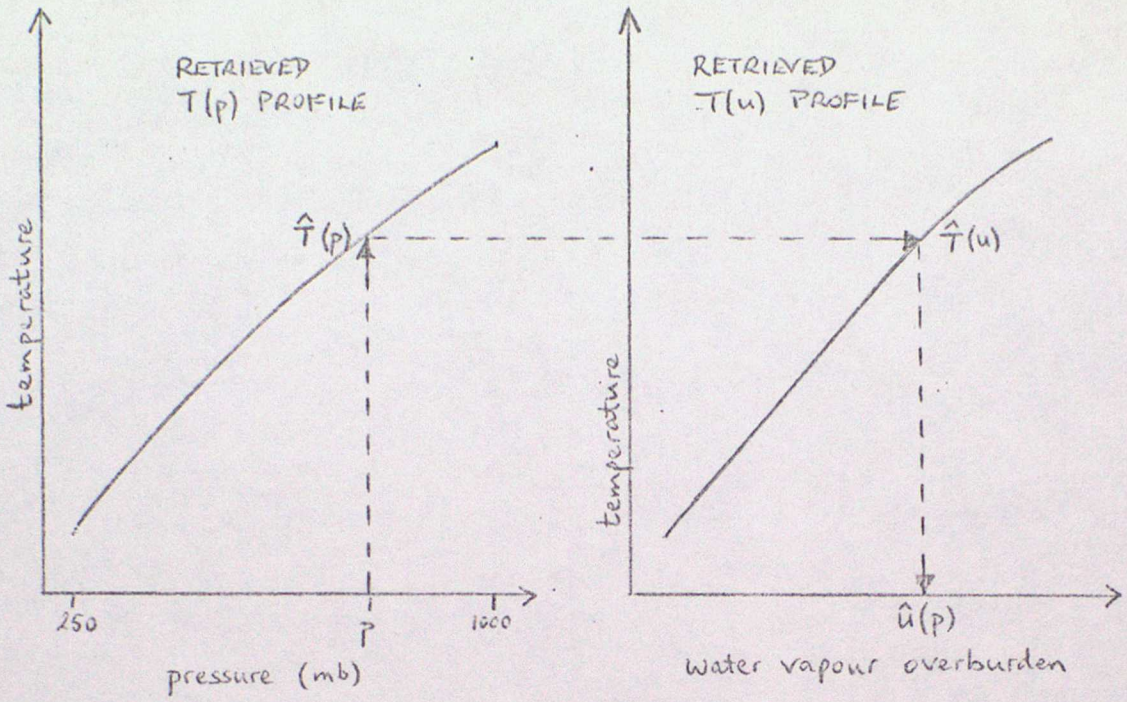

FIGURE 3. ILLUSTRATING THE RETRIEVAL OF WATER VAPOUR OVERBURDEN PROFILE USING THE METHOD OF ROSENKRANZ ET AL. (1982).

ADVANCED LECTURES - SATELLITE METEOROLOGY - 1984

LECTURE 5: THE HERMES LOCAL-AREA SOUNDING SYSTEM: AN EXAMPLE OF A PRACTICAL RETRIEVAL SCHEME

by J.R.Eyre

1. Introduction

Met.O.19 has recently established a system for routine processing of locally-received data from the TIROS Operational Vertical Sounder (TOVS) instruments on the TIROS-N series of polar-orbiting satellites. The system, known as HERMES (High-resolution Evaluation of Radiances from MEteorological Satellites), has two functions: processing TOVS data for use in operational forecasting, and research and development on satellite data interpretation techniques. In this lecture we shall consider details of the retrieval scheme currently used for TOVS data processing and the areas of potential future improvement. Lecture 6 will describe other aspects of the HERMES system, namely the operational framework of TOVS data processing and the planned role of the products in the forecasting environment of the Office. A description of the system in its development phase is given by Eyre and Jerrett (1982) and some case study results are presented in Jerrett et al. (1982).

2. Scientific overview

2.1 The radiometers

Operational atmospheric sounding is currently performed by the TOVS instruments described by Schwalb (1978) and Werbowetzki (1981). Briefly, each satellite carries 3 sounding radiometers collectively known as TOVS:

- The High-resolution Radiation Sounder (HIRS), which has 19 infra-red channels (and one visible channel) for measuring temperature in the troposphere and lower stratosphere, and for sounding tropospheric humidity.

- The Microwave Sounding Unit (MSU), which has 4 channels at frequencies around 55 GHz for measuring tropospheric and lower stratospheric temperature. It has inferior horizontal and vertical resolution to HIRS, but its measurements are affected relatively little by the presence of cloud.

- The Stratospheric Sounding Unit (SSU), which has 3 infra-red channels around 15 μm wavelength and uses a pressure modulation technique for sensing radiation from the middle and upper stratosphere (see Miller et al., 1980).

The details of the channels of these instruments are given in table 1. Considerable use has been made of SSU data for global stratospheric

analysis. However, the retrieval scheme described here is intended to produce high-resolution tropospheric retrievals on a regional scale. Consequently it does not make use of SSU data (although it could be extended to do so).

Each instrument scans the Earth from left to right covering a swath below the satellite as illustrated in figure 1. (The scan pattern of SSU is similar to that of MSU but covers a swath of reduced width, i.e. about 1500 km.) The horizontal resolution of the products obtained from each instrument cannot exceed that imposed by the separation of adjacent fields-of-view. This is on average about 40 km for HIRS and about 170 km for MSU.

2.2 The data processing scheme

The scheme used is similar in most respects to the global operational system used by NOAA/NESDIS, Washington D.C., to generate the soundings which are distributed internationally as SATEM messages (see Smith et al., 1979). The major difference concerns the horizontal resolution of the retrieved products: NESDIS derive products from "boxes" of 7 x 9 HIRS soundings with a spacing of about 300 km, whereas the HERMES scheme seeks to exploit more fully the resolution of the original data and at present yields profiles with a spacing down to 80 km in cloud-free and partly cloudy areas (see section 5).

The retrieval scheme in current use was obtained from the NOAA/NESDIS Development Laboratory at the Co-operative Institute for Meteorological Satellite Studies, Madison, Wisconsin, and the scientific content of the scheme has been modified only slightly. The major elements of the data processing are presented below:

(a) "Decommutation"

The first stage in the processing chain "catches" the data broadcast by the satellite in real-time. It unpacks the raw data stream, checks the gross structure of the data and strips out HIRS and MSU measurements.

(b) Calibration

The raw data are in the form of digital counts and must be converted into physical units. This is done using the calibration information in the data stream, as described in section 3.

(c) Earth-location

The latitude and longitude of each sounding are calculated using knowledge of the satellite's orbital characteristics and the instruments' scanning geometries. The TBUS messages received daily from the USA over the GTS update the parameters of the satellite's orbit. This information acts as input data to an orbital prediction model which is used to calculate the sub-satellite point for any time up to a few days ahead with an accuracy sufficient for TOVS data location. Simple geometry allows the latitude and longitude of the sounding to be derived given the sub-satellite point, the inclination of the orbit, the

satellite altitude and the scan angle of the instrument relative to the satellite.

(d) "Pre-processing"

The next step consists of a series of small corrections to the measured brightness temperatures to put them into a form suitable for the inversion process. These include:

- correcting the HIRS brightness temperatures for scan angle, i.e. converting values at the angle of measurement to values which would have been measured if the instrument had been viewing vertically,
- correcting the HIRS window channels (numbers 8, 18 and 19) for the effects of atmospheric water vapour,
- correcting MSU brightness temperatures for scan angle,
- correcting MSU values for surface emissivity effects, i.e. correcting measured values to those which would have been measured if the surface were black,
- correcting MSU for the angular dependence of its antenna gain to obtain the values which would have been measured if the instrument had an infinitely narrow angular response,
- interpolating MSU brightness temperatures to HIRS sounding locations.

The scan angle and other corrections are performed using regressions against other channels as explained in section 4. For MSU, the corrections for the 3 physical effects are combined into one regression-based correction.

(e) Cloud-clearing

This step treats the problem of cloud-contamination of infra-red radiances. It effectively classifies the pre-processed brightness temperatures roughly according to their degree of cloud-contamination and determines the retrieval route to be used:

- If the HIRS radiances are identified as cloud-free, they are used directly in the retrieval.
- If the HIRS radiances are identified as cloud-contaminated but are amenable to cloud-clearing as described in section 5, then they undergo the cloud-clearing algorithm to estimate the radiances which would be measured from the same profile in the absence of cloud; these are then used in the retrieval.
- If the cloud-contamination is such that clear HIRS radiances cannot be accurately estimated, no retrieval is attempted at this stage (but see paragraph (g) below).

(f) Inversion

As explained in lecture 4, the inversion is performed using a multiple linear regression relation which estimates vectors of temperature, $\hat{\underline{t}}$, and humidity mixing ratio, $\hat{\underline{c}}$, (expressed at standard pressure levels) from the vector of pre-processed, cloud-free (or cloud-cleared) brightness temperatures, $\underline{t_B}$:

$$\hat{\underline{t}} = \underline{\underline{D}} \cdot \underline{t_B} \quad , \qquad \ldots 2.1$$

$$\hat{\underline{c}} = \underline{\underline{D}}' \cdot \underline{t_B} \quad , \qquad \ldots 2.2$$

where all vectors are expressed as differences from mean vectors.

The predictive matrices $\underline{D}$ and $\underline{D}'$ (and the corresponding mean vectors) are obtained from a large set of collocated radiance measurements and radiosonde profiles by multiple linear regression on the eigenvector coefficients of the appropriate covariance matrices (Smith and Woolf, 1976). The regression coefficients are updated every week by NOAA/NESDIS using collocations collected during the previous 2 weeks. Separate regression coefficients are produced for 5 latitude zones: 90-60°S, 60-30°S, 30°S-30°N, 30-60°N and 60-90°N. For retrievals in the vicinity of the zone boundaries, the coefficients are carefully interpolated to avoid steps in the retrieved values. For temperature retrieval both HIRS and MSU brightness temperatures are used in the vector, $\underline{t}_B$. At present HIRS channels 1-16 and MSU channels 2-4 are employed. HIRS channels 17-19 are subject to contamination by solar radiation and are difficult to use during the day-time. MSU channel 1 is a window channel and its interpretation is complicated by uncertainties in surface emissivity. It is therefore applied indirectly to correct other MSU channels for minor surface emissivity effects but is not itself used in the inversion. The mixing ratio retrieval uses only HIRS channels, but it utilises temperature sounding channels as well as humidity sounding channels. In this way information on the temperature profile, which is necessary for accurate humidity retrieval, enters the solution indirectly.

(g) Derived quantities and additional processing

A number of additional checks and computations are performed following the inversion. The most notable are as follows:

- Mixing ratios are converted to dew points.
- The estimated profiles are integrated to provide quantities representing layer mean values, i.e. geopotential thickness and layer precipitable water, for layers between standard pressure levels.
- A number of rejection tests are performed on the retrievals. The difference between HIRS+MSU and MSU-only retrievals is computed and the retrieval is only passed if the sum of the squares of the difference is below a given threshold. Soundings which are grossly inconsistent with their neighbours are also rejected.
- When HIRS+MSU retrievals have been attempted for a complete satellite overpass, the horizontal coverage is analysed to search for large gaps. Under certain conditions the gaps are judged suitable for the addition of MSU-only soundings. Care is taken to adjust such soundings for local biases between HIRS+MSU and MSU-only soundings.
- Using each successful retrieval as a processing centre, the local gradient of the thickness field is computed from a group of neighbouring soundings. This gradient is then expressed as a geostrophic thermal wind. These values do not contain any information which is not present in the thicknesses, but they are found helpful in visualising the fields when expressed in chart form and may prove useful as inputs to numerical analyses (see section 6).

Figure 2 gives an example of a plotted chart obtained from derived products and shows the 1000-500 mb thickness values and associated thermal winds retrieved from 4 consecutive passes of NOAA-7 data. Figure 3 gives an example of a retrieved vertical profile together with a collocated radiosonde ascent.

3. Calibration of HIRS and MSU

For HIRS, calibration measurements are made every 40 scan lines and occupy 3 scan lines (for which no earth-view data are available). During this period the instrument views an internal black-body target, the temperature of which is monitored. This gives a warm reference point. A cold reference point is obtained by viewing space, which acts as a black body at about 3 K — essentially a zero radiance target. Since the radiometer is designed to give an output linearly related to the incoming radiance, it can be calibrated as shown in figure 4.

The calibrated radiance for each channel is converted to an equivalent black body temperature ("brightness temperature") using a relation containing the inverse Planck function:

$$T_B = a + b\left\{\frac{c_2 \nu_0}{\ln\left(\frac{c_1 \nu_0^3}{R} + 1\right)}\right\} \qquad \ldots 3.1$$

where $c_1 = 1.1911 \times 10^{-8}$ W.m^{-2}.sr^{-1}.(cm^{-1})$^{-1}$,
$c_2 = 1.4388$ K.(cm^{-1})$^{-1}$,
ν_0 is the central wavenumber of the channel,
and R is the calibrated radiance.

a and b are known as "band correction coefficients". They allow for the fact that the radiometer channel is not monochromatic and are determined numerically using the spectral response of the radiometer channel (see Lauritson et al., 1979). For a narrow band radiometer such as HIRS $a \ll T_B$ and $b \simeq 1$.

For MSU, the calibration sequence takes place at the end of each scan line and so no earth view data are lost. Again a 2-point calibration is provided from warm and cold reference sources. However, for MSU channel frequencies and typical earth-view temperatures, the measured radiances are in the Rayleigh-Jeans tail of the Planck function, where radiance is proportional to brightness temperature. Therefore the data may be calibrated into brightness temperatures directly.

4. Limb correction

This term is used to describe the process whereby a brightness temperature measured at a non-zero nadir angle is corrected to provide an estimate of the value which would have been measured if the instrument had viewed the same volume of atmosphere vertically. The physical effect which necessitates this correction is illustrated in figure 5. As the angle of view moves away from the vertical, the path length of the radiation through the atmosphere increases. Therefore the transmittances from all levels to space decrease and the peak of the weighting function rises (see lecture 2). If the channel senses radiation from an atmospheric layer in which there is a temperature lapse rate, then the measured radiance will change; for tropospheric channels it will tend to decrease.

It would, of course, be possible to remove the need for a limb correction by using a temperature retrieval algorithm with a different set of regression coefficients for each scan angle, or by using a physical retrieval method in which radiances are applied at their angle of measurement. However, because we have chosen to perform a regression retrieval in which one set of coefficients (appropriate to a zero scan angle) is used, we must convert all brightness temperatures to this form.

Adequately accurate limb corrections are possible because the weighting function of the nadir view for one channel will, in general, peak at a level intermediate between the weighting function peaks of 2 channels at the angle of measurement. Thus, for a given angle, θ, we may express the difference between the brightness temperature at nadir and at the angle of measurement as a linear combination of the measured brightness temperatures in a number of channels:

$$(T_B)_i^{\theta=0} - (T_B)_i^{\theta} = a_{0i}^{\theta} + \sum_{i'=1}^{I} a_{i'i}^{\theta} (T_B)_{i'}^{\theta} . \qquad \ldots 4.1$$

The coefficients, $a_{i'i}^{\theta}$ are found by multiple linear regression on synthetic brightness temperatures computed for a representative set of profiles.

5. Cloud-clearing

Infra-red radiances are affected markedly by the presence of clouds, since most are almost opaque in this wavelength region. Consequently the algorithms used in the retrieval of tropospheric temperature must be able to detect clouds which have a significant effect on the radiances and, if possible, make allowances for these effects. This is usually done by correcting the measured radiances to obtain "clear-column" values, i.e. the radiances which would be measured from the same temperature and humidity profiles in the absence of cloud. In most retrieval schemes the inversion process converts clear-column radiances to atmospheric parameters and so a preliminary cloud-clearing step is required.

A review of cloud-clearing methods is given by Eyre (1983). Many of the algorithms developed, including the one used in this retrieval scheme, are variants of the adjacent field-of-view or N* method first proposed by Smith (1968). In this approach, the measured radiances, R_1 and R_2, in 2 adjacent fields-of-view (hereafter referred to as "spots") of a radiometer channel can, under certain conditions, be expressed as follows:

$$\left.\begin{aligned} R_1 &= N_1 R_{cloudy} + (1 - N_1) R_{clear} , \\ R_2 &= N_2 R_{cloudy} + (1 - N_2) R_{clear} , \end{aligned}\right\} \qquad \ldots 5.1$$

where R_{clear} and R_{cloudy} are the radiances appropriate to clear and completely overcast conditions respectively, and N_1 and N_2 are the effective fractional cloud coverages in spots 1 and 2. In deriving these equations the following assumptions have been made:

- that the atmospheric profile and surface characteristics in the 2 spots are the same,
- that only one layer of cloud is present,
- that the cloud top has the same height (and temperature) in both spots.

If the fractional cloud coverages in the 2 spots are different ($N_1 \neq N_2$), then equations 5.2 may be solved simultaneously to give the clear radiance:

$$R_{clear} = \frac{R_1 - N^* R_2}{1 - N^*} , \qquad \ldots 5.2$$

where $N^* = N_1 / N_2$. Alternatively,

$$N^* = \frac{R_{clear} - R_1}{R_{clear} - R_2} , \qquad \ldots 5.3$$

and so N* can be found if we have an estimate of the clear radiance in one channel. The requirement for this additional piece of information leads to different practical formulations of the N* method suited to the type of data available and the products required, as explained below. Since N* is channel-independent, it can be used in equation 5.2 to find the clear radiance in all other channels. The method is illustrated in figure 6(a). For infra-red radiometers with moderately high horizontal resolution (e.g. HIRS, with a field-of-view spacing of about 40 km), the inherent assumptions are true sufficiently often for the method to be useful. Various quality controls are applied to trap those cases for which the cloud field does not conform with the assumptions made.

The variant of this method used by NOAA/NESDIS for global retrievals is described by McMillin and Dean (1982). It has been developed specifically to meet the requirements for global, low-resolution retrievals on a scale of about 300 km. The Met.0.19 system uses a variant more suited to regional and mesoscale applications, in which clear radiances are required at higher horizontal resolution. A cloud-clearing algorithm based on a box of 3 x 3 HIRS spots is used. N*, and hence clear radiances, is calculated 8 times, the central spot being used with each of its 8 neighbours (figure 6(b)). The additional piece of information required for the solution of equation 5.3 is obtained from the measured value of MSU channel 2 which acts as a "pseudo-HIRS" channel. This approach is successful because the weighting functions of HIRS and MSU overlap, and the brightness temperature in MSU channel 2 can be predicted quite accurately from a linear combination of cloud-free HIRS brightness temperatures:

$$T_{MSU-2} \simeq b_0 + \sum_i b_i T_{HIRS-i} \qquad \ldots 5.4$$

The coefficients, b_i, are also calculated by regression on collocated measurements and are updated weekly by NOAA/NESDIS (although this is probably unnecessary). From equations 5.4 and 5.2, and assuming a linear relation between radiance and brightness temperature, we can obtain an expression for N*:

$$N^* = \frac{T_{MSU-2} - b_0 - \sum_i b_i T_{1i}}{T_{MSU-2} - b_0 - \sum_i b_i T_{2i}} , \qquad \ldots 5.5$$

where T_{1i} and T_{2i} are the measured HIRS brightness temperatures in channel i for spots 1 and 2 respectively, and T_{MSU-2} is the measured brightness temperature in MSU channel 2 interpolated to the central HIRS spot. (The assumption of linearity between radiance and brightness temperature is an approximation which can lead to large errors in certain cases. This aspect of the cloud-clearing could be improved and is currently under review.) In the present implementation of the N* method, N* is calculated separately for the HIRS longwave tropospheric channels (4-12) and the shortwave tropospheric channels (13-16) in an attempt to allow for an instrument effect which may cause small differences in field-of-view location for the 2 sets of channels. For each pair of spots, the processing is only allowed to continue for values of N* less than 0.75. If N* is greater than 0.75, the error amplification is considered too large; physically, the spots are too similar for the N* technique to apply.

From all the sets (up to 8) of successfully cloud-cleared HIRS radiances generated from 8 N* calculations, plus the set of "clear" radiances (i.e. the measured radiances treated as cloud-free), the set is chosen which leads to the best agreement between HIRS+MSU and MSU-only retrieval (measured by the sum of the square of the retrieved temperature differences for the 5 lowest standard pressure levels).

6. Error characteristics

The accuracy of satellite retrievals is difficult to assess: as with many other observing systems, we are faced with the problem of "what is truth?". A widely-used method of assessing accuracy is the study of statistics of differences between retrievals and collocated radiosonde profiles. Such statistics will include the retrieval errors but will also contain contributions from radiosonde errors (which include the effects of both discrepancies from the true profile along the radiosonde ascent path and also the degree to which this profile is representative of the surrounding volume of atmosphere) and collocation errors caused by the separation in space and time between the satellite sounding and the radiosonde ascent. Although retrieval-radiosonde collocation statistics are very useful, they should not be treated simply as measurements of retrieval error.

Figure 7 shows typical statistics from the HERMES retrieval system. The bias and standard deviation profiles for retrieval-radiosonde differences are shown. These are based on all collocations obtained from NOAA-7 retrievals during October 1983, with collocation criteria of ±3 hours time separation and 150 km horizontal separation. If the set of profiles in the collocations and the set from which the regression coefficients have been generated are large and both are representative of the same population, then the biases in these statistics should be very small. The biases found, about 1 degree at some pressure levels, are to be expected here, where collocations for a limited period and limited area may not be representative of a zonal set. The standard deviations, while they are larger than the equivalent values for retrieval errors alone, exhibit some of the

expected characteristics of the retrieval error profile. They have a minimum in the mid-troposphere, with higher values near the surface and at the tropopause. The lower tropospheric values reflect problems associated with residual cloud contamination and various surface effects. Low level inversions will also tend to cause retrieval problems. The tropopause values reflect both the lack of information in the radiances from this part of the profile and also the tendency of the regression coefficients to "smooth out" features of this type.

It is possible to assess theoretically the accuracy which should be attained by studying the residual error in the regression between a set of profiles and corresponding calculated brightness temperatures; using realistic values for the "noise" in the cloud-cleared brightness temperatures. A theoretical error curve, obtain in this way from 400 profiles chosen to be representative of September conditions for the European and N. Atlantic areas, is also shown in figure 7. This represents the attainable limit for this combination of instruments with this retrieval scheme.

The errors in humidity retrievals are more difficult to study because of increased prblems with radiosonde errors and the horizontal scales of humidity field fluctuations. Statistics from the HERMES system are currently showing standard deviations in dew point differences of about 6-7 degrees between retrievals and sondes. There are indications that retrieval errors are the major contributors below 800 mb, but that radiosonde errors (and failures to be representative of the surrounding atmospheric volume) are more important in the mid-trosophere, although this has not yet been clearly demonstrated.

A further aspect of the error characteristics which should be taken into account when using the data in numerical analysis concerns the spatial correlation of retrieval errors. Radiance measurements from channels with broad, overlapping weighting functions will lead to errors which are correlated in the vertical. Also the strong assocation between retrieval errors and profile shape will often lead to similar errors in adjacent profiles where the true atmospheric profiles are similar. This horizontal correlation of error can be put to good use, because it assists accurate computation of the gradient (i.e. geostrophic thermal wind) in the retrieved field, which may itself be a useful analysis parameter.

7. Future improvements

The retrieval scheme descibed above has been implemented with the intention of its output being used in operational forecasting, because the products are considered to have reached a level of accuracy at which they are potentially useful, particularly in data sparse regions. However it is recognised that there is considerable scope for improvement in several aspects of the retrieval process.

A number of minor improvements are planned in the calibration and limb-correction algorithms, the treatment of sea-ice, the mapping of MSU data to HIRS locations, the cloud-clearing routine and others. In addition, more fundamental changes to the retrieval process will be tested. There is scope for improvement in the approach to cloud-clearing by developing a scheme which attempts to achieve better horizontal consistency in the cloud-cleared radiances (Eyre, 1983). Also better results might be expected if the cloud-clearing preceded the limb-correction. Another avenue of investigation with potential for improving the cloud-clearing concerns the use of Advanced Very High Resolution Radiometer (AVHRR) data. From this imagery it is possible to extract information on the cloud field and surface temperature which should be of considerable value in the derivation of clear radiances. Successful developments in these areas would be expected to improve the quality of retrievals in the lower troposphere.

Another area of potential improvement is in the use of atmospheric statistics. It is expected that regression coefficients derived from a carefully selected historical set of radiosonde profiles from the European / N. Atlantic area, together with corresponding synthetic brightness temperatures, will lead to better results that the present system, based on regression coeffients from collocations (see section 2(f) and discussion in lecture 4). Another promising approach concerns a more sophisticated use of statistics, involving the generation of several sets of regression coefficients corresponding, perhaps, to different air mass types or profile shapes. Also, we have seen in lecture 4 that the present humidity retrieval approach has deficiencies and improvements can be expected from a more appropriate application of atmospheric statistics or a scheme which is more physically based. Indeed, it is acknowledged that, in general, inprovements are to be expected from a more explicit application of a (correct) understanding of the physics involved, and ways should be sort to include these while attempting to preserve the advantages of the statistical approach and taking care not to add unacceptably to the computer processing time required.

REFERENCES

Eyre J.R.
Met.O.19 Branch Memorandum 72 (1983).
Towards an optimal approach to cloud-clearing for satellite temperature sounding.

Eyre J.R., Jerrett D.
Weather, 37, 314-322 (1982).
Local-area atmospheric sounding from satellites.

Jerrett D., Eyre J.R., McCallum E.
Proc.Annual Tech.Conf.Remote Sensing Society (Liverpool, Dec. 1982), pp. 230-237 (1983).
High resolution soundings of temperature in the European / N. Atlantic area.

Lauritson L., Nelson G.J., Porto F.W.
NOAA Technical Memorandum NESS 107 (1979).
Data extraction and calibration of TIROS-N/NOAA radiometers.

McMillin L.M., Dean C.
J.Appl.Meteor., 12,1005-1014 (1982).
Evaluation of a new operational technique for producing clear radiances.

Miller D.E., Brownscombe J.L., Carruthers G.P., Pick D.R., Stewart K.H.
Phil.Trans.R.Soc.Lond., A296, 65-71 (1980).
Operational temperature sounding of the stratosphere.

Schwalb A.
NOAA Technical Memorandum NESS 95 (1978).
The TIROS-N/NOAA A-G satellite series.

Smith W.L.
Mon.Wea.Rev., 96, 387-396 (1968).
An improved method for calculating tropospheric temperature and moisture profiles from satellite radiometer measurements.

Smith W.L., Woolf H.M.
J.Atmos.Sci., 33, 1127-1140 (1976).
The use of eigenvectors of statistical covariances matrices for interpreting satellite sounding radiometer observations.

Smith W.L., Woolf H.M., Hayden C.M., Wark D.Q., McMillin L.M.
Bull.Amer.Meteor.Soc., 60, 1177-1187 (1979).
The TIROS-N operational vertical sounder.

Werbowetzki A.
NOAA Technical Report NESS 83 (1981).
Atmospheric sounding user's guide.

HIRS Channel number	Channel central wavenumber	Central wavelength (μm)	Principal absorbing constituents	Level of peak energy contribution	Purpose of the radiance observation
1	668	15.00	CO_2	30 mb	*Temperature sounding.* The 15-μm band channels provide better sensitivity to the temperature of relatively cold regions of the atmosphere than can be achieved with the 4.3-μm band channels. Radiances in Channels 5, 6, and 7 are also used to calculate the heights and amounts of cloud within the HIRS field of view.
2	679	14.70	CO_2	60 mb	
3	691	14.50	CO_2	100 mb	
4	704	14.20	CO_2	400 mb	
5	716	14.00	CO_2	600 mb	
6	732	13.70	CO_2/H_2O	800 mb	
7	748	13.40	CO_2/H_2O	900 mb	
8	898	11.10	Window	Surface	*Surface temperature* and cloud detection.
9	1 028	9.70	O_3	25 mb	*Total ozone* concentration.
10	1 217	8.30	H_2O	900 mb	*Water vapor sounding.* Provides water vapor corrections for CO_2 and window channels. The 6.7-μm channel is also used to detect thin cirrus cloud.
11	1 364	7.30	H_2O	700 mb	
12	1 484	6.70	H_2O	500 mb	
13	2 190	4.57	N_2O	1 000 mb	*Temperature sounding.* The 4.3-μm band channels provide better sensitivity to the temperature of relatively warm regions of the atmosphere than can be achieved with the 15-μm band channels. Also, the short-wavelength radiances are less sensitive to clouds than those for the 15-μm region.
14	2 213	4.52	N_2O	950 mb	
15	2 240	4.46	CO_2/N_2O	700 mb	
16	2 276	4.40	CO_2/N_2O	400 mb	
17	2 361	4.24	CO_2	5 mb	
18	2 512	4.00	Window	Surface	*Surface temperature.* Much less sensitive to clouds and H_2O than the 11-μm window. Used with 11-μm channel to detect cloud contamination and derive surface temperature under partly cloudy sky conditions. Simultaneous 3.7- and 4.0-μm data enable reflected solar contribution to be eliminated from observations.
19	2 671	3.70	Window	Surface	
20	14 367	0.70	Window	Cloud	*Cloud detection.* Used during the day with 4.0- and 11-μm window channels to define clear fields of view.

MSU	Frequency (GHz)	Principal absorbing constituents	Level of peak energy contribution	Purpose of the radiance observation
1	50.31	Window	Surface	*Surface emissivity* and *cloud attenuation* determination.
2	53.73	O_2	700 mb	*Temperature sounding.* The microwave channels probe through clouds and can be used to alleviate the influence of clouds on the 4.3- and 15-μm sounding channels.
3	54.96	O_2	300 mb	
4	57.95	O_2	90 mb	

SSU	Wavelength (μm)	Principal absorbing constituents	Level of peak energy contribution	Purpose of the radiance observation
1	15.0	CO_2	15.0 mb	*Temperature sounding.* Using CO_2 gas cells and pressure modulation, the SSU observes thermal emissions from the stratosphere.
2	15.0	CO_2	4.0 mb	
3	15.0	CO_2	1.5 mb	

Table 1.

Characteristics of TIROS Operational Vertical Sounder (TOVS) channels

From Smith et al., 1979

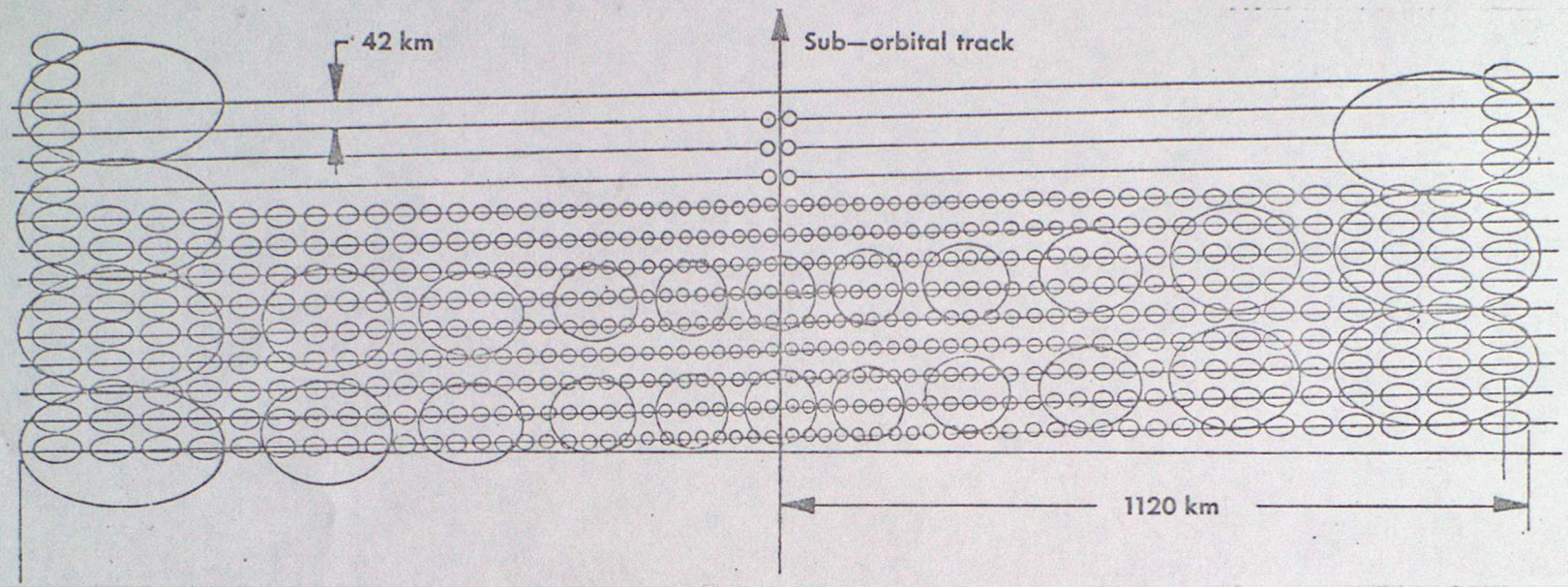

HIRS : Soundings per scan line=56 Line spacing=42 km

MSU : Soundings per scan line=11 Line spacing=168 km

FIGURE 1 HIRS AND MSU SCAN PATTERNS

FIGURE 2. AN EXAMPLE OF HERMES PRODUCTS DERIVED FROM NOAA-7 DATA

HERMES

1000 - 500 MB. THICKNESS

LAST PASS: 0650Z 11 FEB 1984

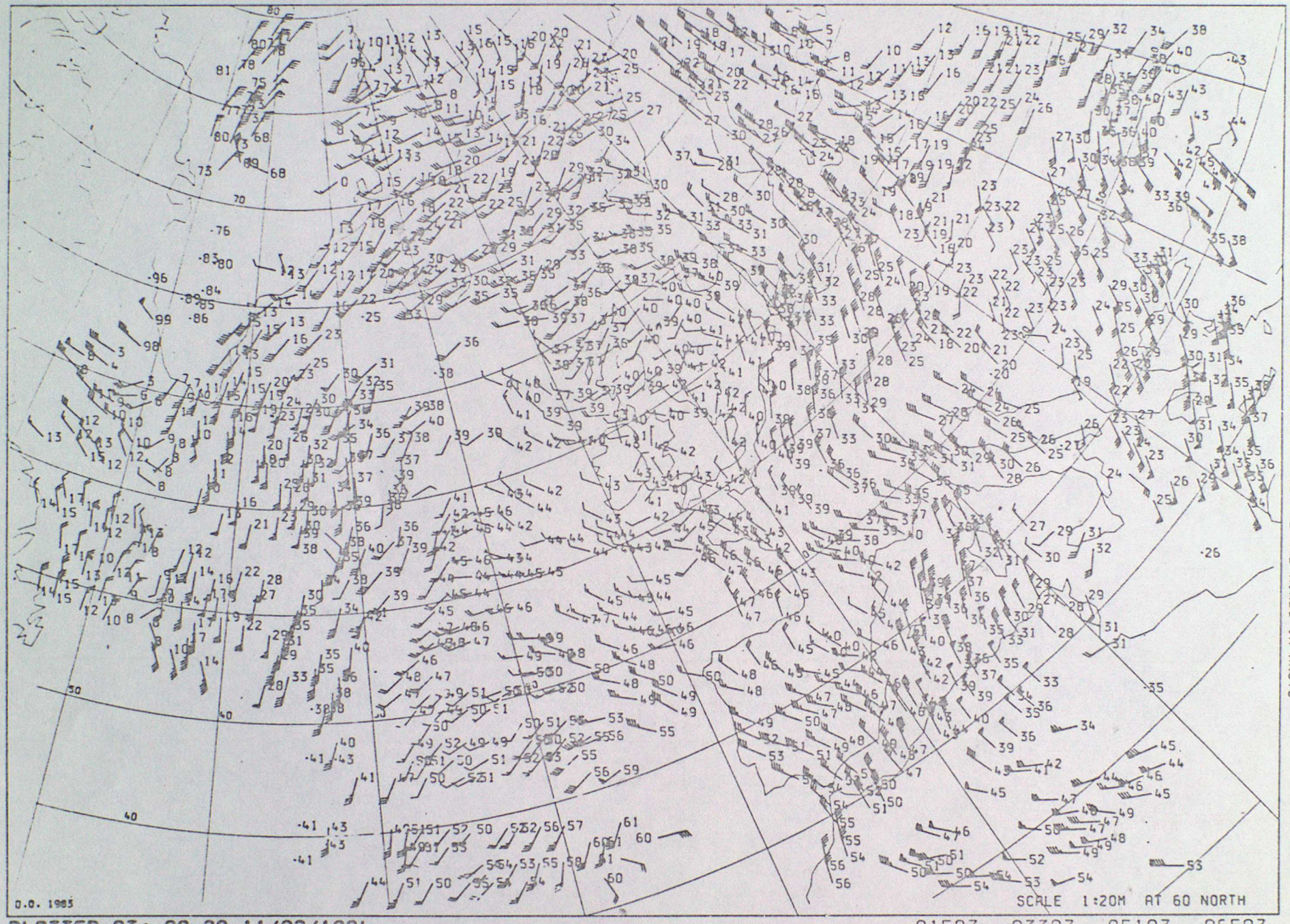

THICKNESSES IN DM (ONLY LAST TWO DIGITS SHOWN) AND THERMAL WINDS IN KNOTS

PLOTTED AT: 08.20 11/02/1984

0150Z 0330Z 0510Z 0650Z

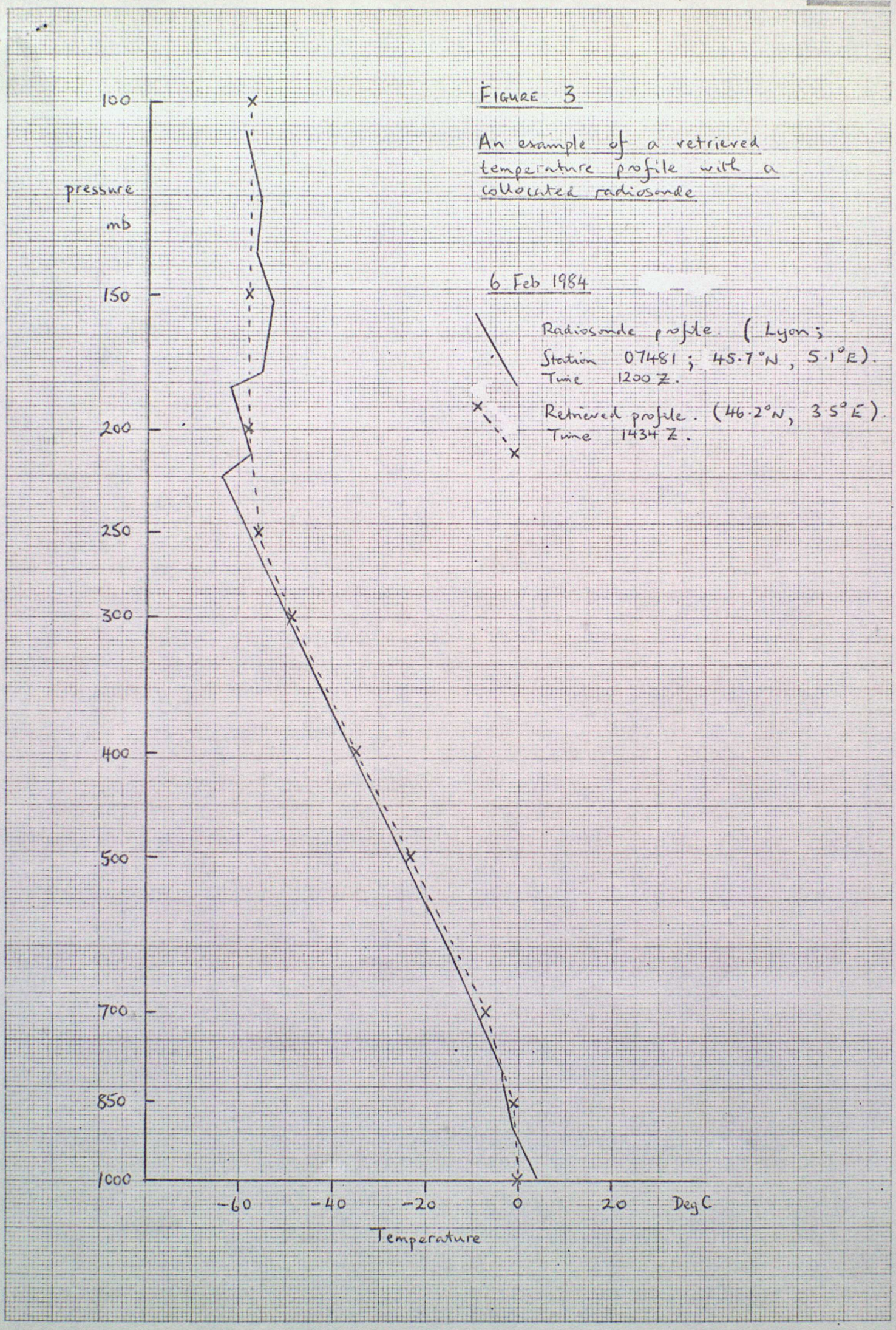

FIGURE 3

An example of a retrieved temperature profile with a collocated radiosonde

6 Feb 1984

Radiosonde profile (Lyon; Station 07481; 45·7°N, 5·1°E). Time 1200 Z.

Retrieved profile. (46·2°N, 3·5°E). Time 1434 Z.

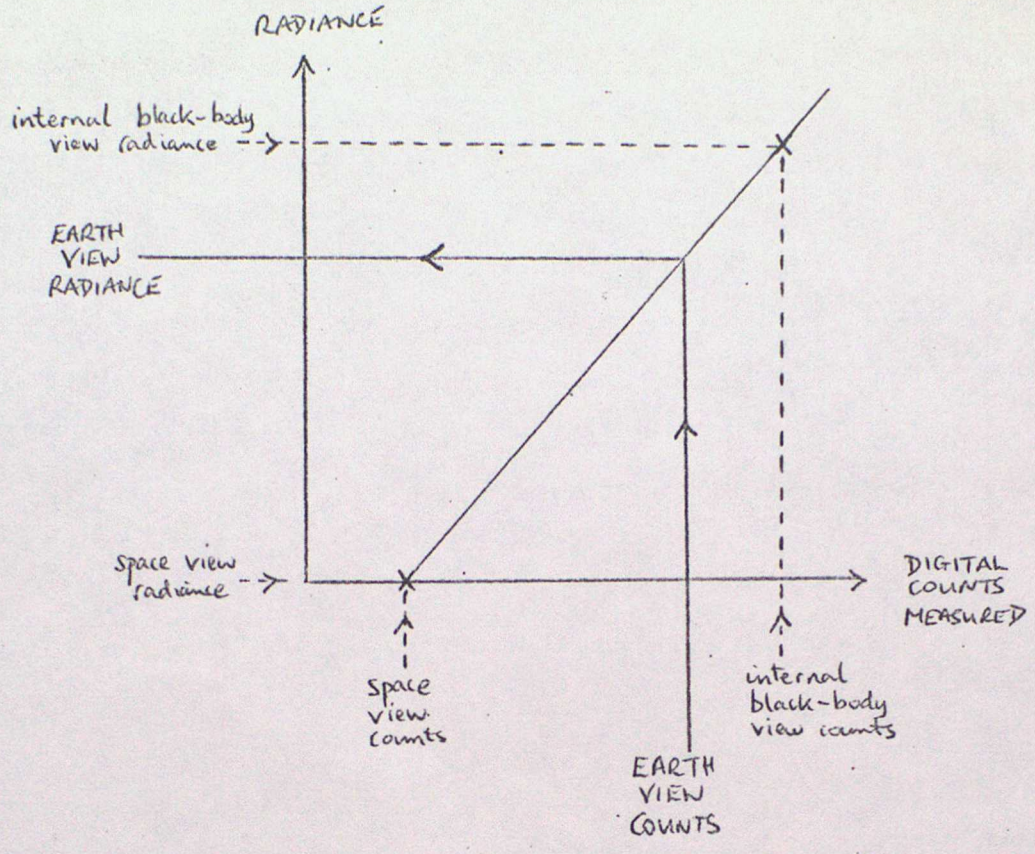

FIGURE 4.

Illustrating the 2-point calibration process for a linear radiometer.

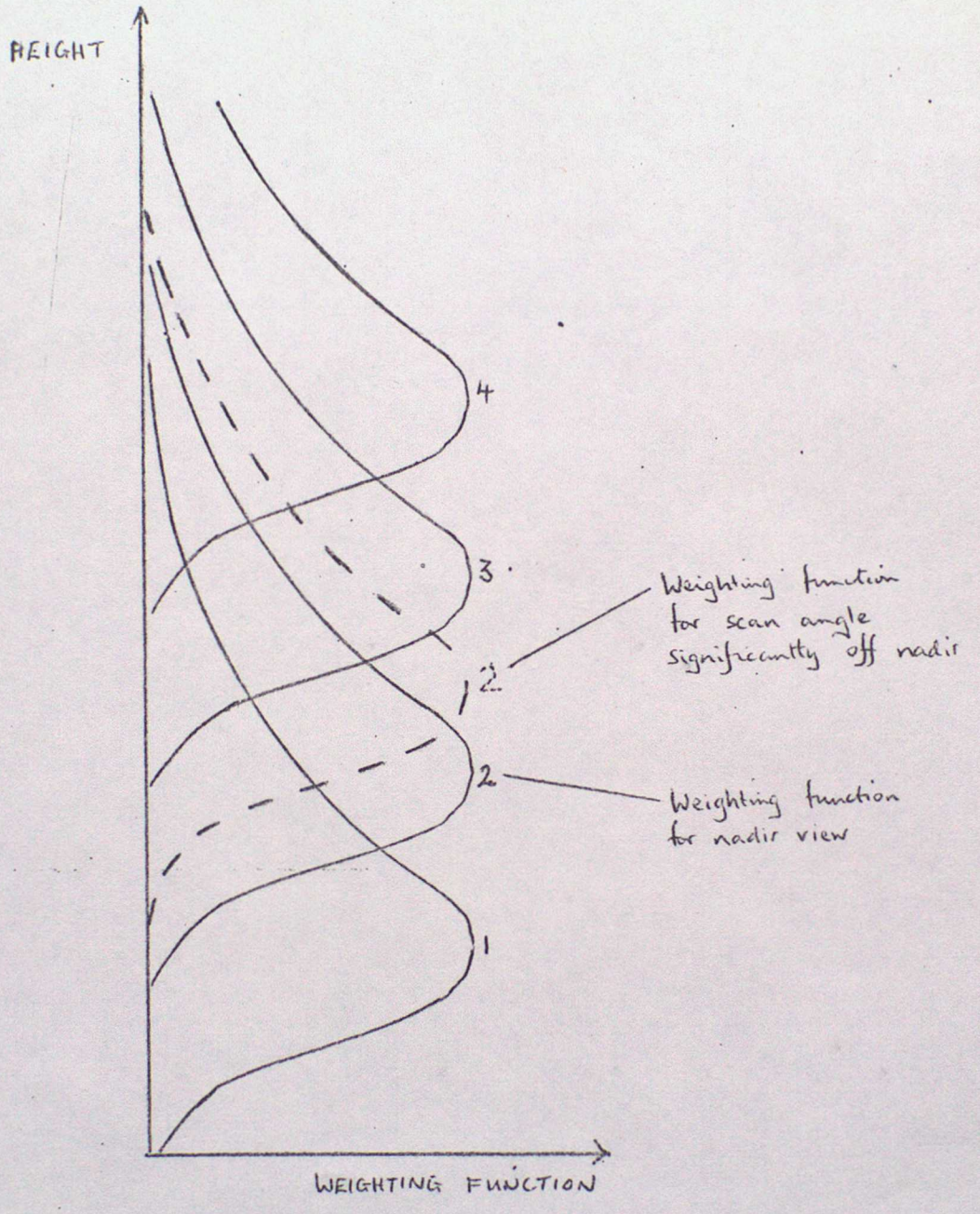

FIGURE 5.

Illustrating schematically a group of weighting functions for nadir viewing and the effect of scanning off nadir on one of these functions.

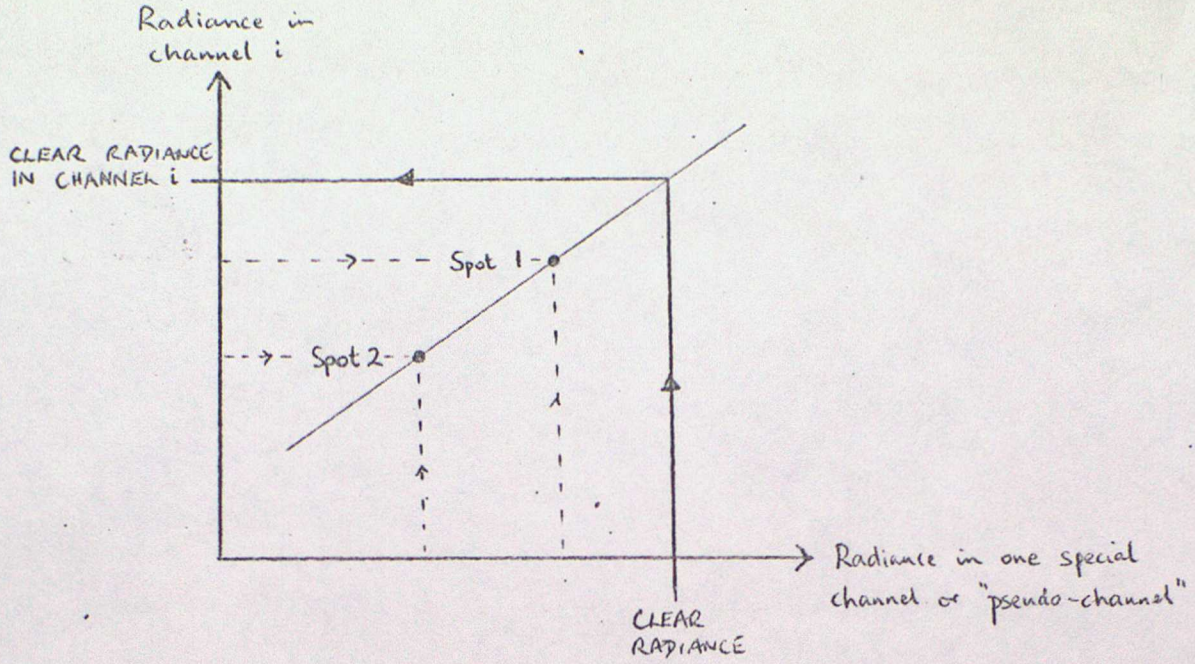

FIGURE 6(a). A graphical representation of the N* cloud-clearing method

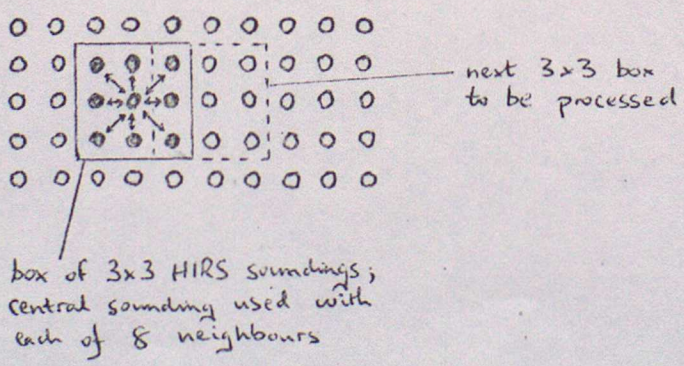

FIGURE 6(b). Illustrating the method of cloud-clearing using 3×3 boxes of HIRS soundings.

FIGURE 7

RETRIEVAL-RADIOSONDE TEMPERATURE DIFFERENCES

NOAA-7 OCTOBER 1983

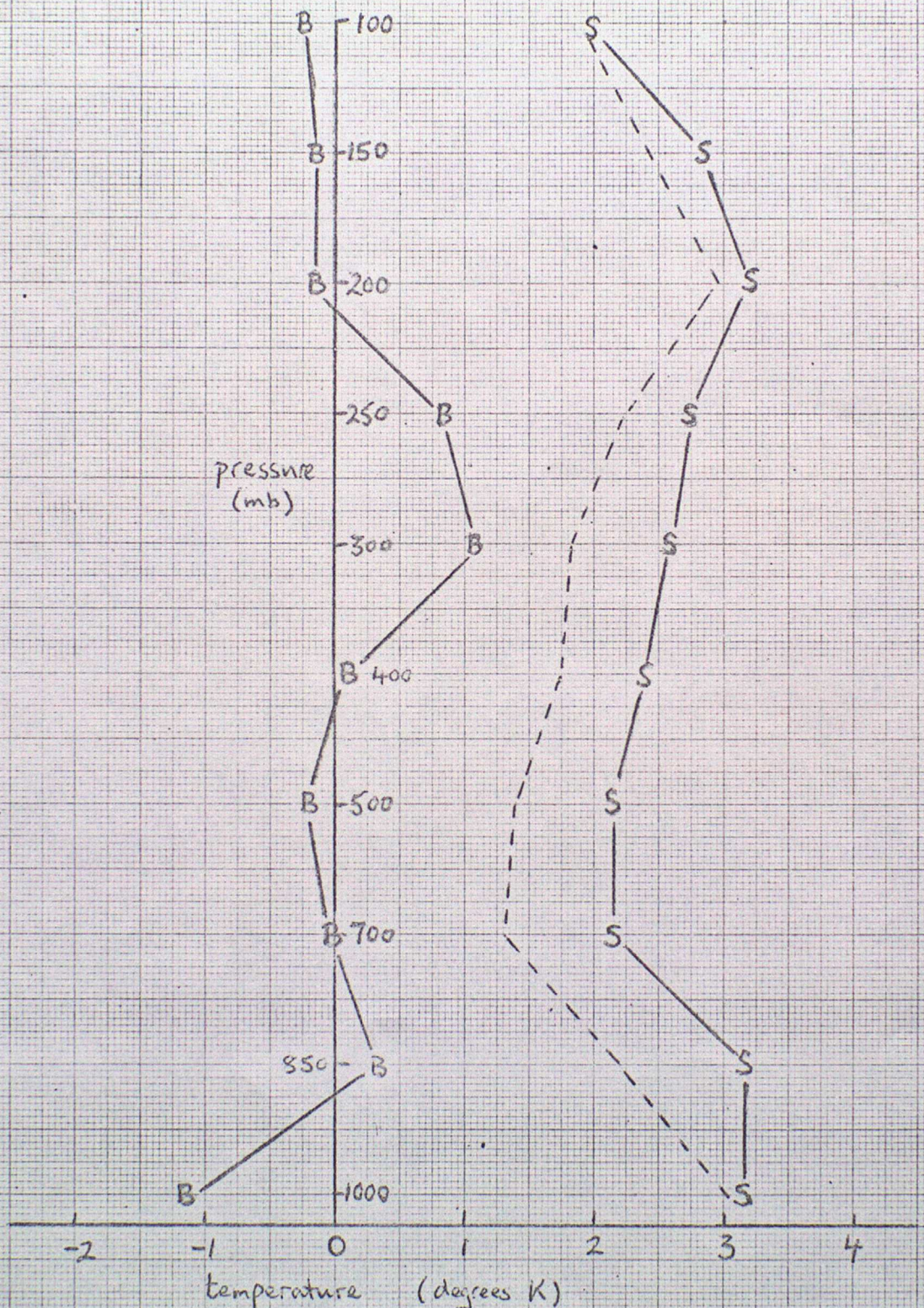

RETRIEVAL-RADIOSONDE DIFFERENCE STATISTICS: { B = BIAS; S = STANDARD DEVIATION

THEORETICAL RETRIEVAL ERRORS (REGRESSION RESIDUAL ERRORS) : \ \

SATELLITE METEOROLOGY

LECTURE 8 (Morgan)

QUANTITATIVE USES OF SATELLITE IMAGE DATA

1. Fundamentals

Most present day imaging systems consist basically of a radiometer with a very small field of view and an arrangement by which it can scan a much larger area. As it scans, the radiometer in effect views tiny elements of the total scene in rapid succession. It measures the radiance from each such element and images are constructed by displaying these radiance values as shades of grey in their correct relative positions, the tiny picture elements are known as pixels and their size determines the limiting spatial resolution of the imaging system. This is generally between about 1 km and 10 km. The grey level resolution of the imaging systems is typically between 6 and 10 bits giving from between 64 and 1024 grey levels for each pixel value. There are two preferred parts of the spectrum for imagery; visible wavelengths (VIS) between about 0.4 μm and 0.7 μm and the infra-red window channel (IR) at around 11 μm. Of the other channels used, the water vapour channel on METEOSAT, at 6.3 μm, is of particular interest. Their characteristics will be considered briefly in turn.

a. Visible (VIS) images

The VIS channels measure reflected radiation in the visible part of the spectrum, and the features which appear brightest in the image are those which reflect sunlight most strongly. They are not necessarily clouds. Snow cover, desert surfaces and smooth sea surfaces can all at times appear just as bright as clouds. The observed brightness depends upon illumination (sun angle), viewing geometry (angular position of the satellite in relation to the sun) and the reflectivity or albedo of the surface. The albedo of clouds can range from about 30% for fair weather cumulus over land up to 92% for large and deep cumulonimbus. Terrestrial features such as sand and snow have an albedo of about 60% whereas the oceans are very dark with albedos of around 7%. Cloud reflectivity depends on cloud thickness, particle size, distribution and composition and the character of the upper cloud surface. When using VIS pictures it is helpful to remember that, in general, increasing brightness is associated with thicker clouds, especially in cyclonic cloud systems. Under similar conditions of illumination, water clouds appear brighter than ice clouds of the same thickness. The shadows and highlights that are present in VIS imagery are often particularly valuable in revealing the structure and texture of cloud systems.

b. Infra-red (IR) images

IR images are derived from radiation emitted by cloud and terrestrial surfaces and provide essentially a representation of the temperature distribution. This is because at the wavelength used, emissivities are mostly close to unity (ie the surfaces can be considered to

radiate as black bodies) and the atmospheric attenuation is small. In quantitative uses of IR imagery, however, account has to be taken of both these parameters and their variations. Emissivity can be significantly less than unity for the cirrus clouds, while atmospheric attenuation becomes increasingly important as water vapour content increases. This attenuation causes a radiating surface viewed by a satellite born radiometer to appear colder than it actually is.

In order to have some similarity in the appearance of clouds in IR and VIS images the convention is to arrange the grey scale of the former so that warm surfaces (high radiance values) appear dark, and cold surfaces (low radiance values) appear light.

Extensive use is made of both VIS and IR imagery, one complementing the other in many applications. The IR image has the virtue of being available night and day, whereas the VIS image is particularly useful in distinguishing bright clouds from underlying dark sea surfaces.

c. Water vapour (WV) images

These METEOSAT images are derived from radiance measurements in the 5.7 μm to 7.1 μm water vapour absorption band in the infra-red, and are the only images in general use which do not view the surface of the earth. At these wavelengths radiation reaching the satellite is emitted by water vapour in the upper atmosphere, roughly between 600 mb to 300 mb, and by any high clouds present. The intensity of the radiance is dependent on the temperature of the layers from which it originates. With high humidities, the radiation to space comes from relatively high (cold) levels and with low humidities it is from the lower (warmer) levels. There is thus a relationship between radiance and humidity. The grey scale on WV imagery is normally arranged so that moist areas appear bright and dry areas dark. Tops of high clouds (especially vigorous Cb) show up as very bright features.

The TIROS-N AVHRR instrument has 5 channels, namely:-

1.	0.55 to 0.90 μm	VIS	
2.	0.72 to 1.10 μm	VIS/Near IR	
3.	3.55 to 3.93 μm	IR	
4.	10.5 to 11.5 μm	IR)	Split window
5.	11.5 to 12.5 μm	)	

2. Main uses of satellite imagery

Images from current operational satellites provide a wealth of information about atmospheric processes and phenomena on scales ranging between near global and mesoscale. Those of operational interest include:-

Cloud cover - type, extent, amount, height.
Surface temperature - land, sea, cloud tops.
Winds and flow patterns.
Precipitation extents and rates
Vertical motion, stability etc.
Synoptic systems and related features - depressions, fronts, etc.
Snow and ice cover.

Turbulence.
Aerosols - haze, volcanic dust, etc.
Humidity.

The list is not exhaustive, it is given simply to illustrate the diversity of information that imagery provides. It will be evident that some items listed can be obtained directly from the images while others have to be inferred. For example, the presence of sun glint (an area of strong solar reflection from the sea surface) implies an area of smooth sea, which in turn implies light surface winds. Using simultaneous images from two or more channels together often yields information that cannot be obtained from any other channels separately, and resolves uncertainties in the interpretation of data from the single channel. High cloud and sea fog may look virtually identical on a VIS image but are easily distinguished on an IR image.

An individual image can provide much information, but if sequences are available movement and development can be observed as well. Many operational users have some kind of rapid replay facility for sequences of geostationary images and this technique frequently shows interesting and important developments which are otherwise apt to pass un-noticed.

In addition to their use and application in operational meteorology the images are also widely used in other overlapping fields. These include:-

Climatology (for cloud cover, albedo and other radiation balance parameters, sea surface temperatures, snow and ice limits etc).

Oceanography (especially effects related to sea surface temperature).

Land use and vegetation cover studies.

Hydrology (soil moisture and evaporation mapping, rainfall monitoring).

3. Image enhancement and display

Images are essentially a large array of radiance values and when expressed in digital form they can be processed by computer to facilitate their interpretation or use in some other way, either qualitatively or quantitatively. A common type of processing is that termed enhancement in which the grey levels of an image are systematically adjusted so that information can be visually interpreted more easily. High quality digital images contain far more radiometric levels than the 16 or so which the human eye can distinguish, so that it is only by some kind of stretching of the scale that some of the finer points of the image will be seen at all. In the same way, enhancement is often of value in partially overcoming limitations of an image display device. The enhancement can be a simple linear one, in which a small range of the original radiance values is expanded to occupy a much larger range of levels on the output display, or it can be more complex such as modifying the histogram of radiance values to approximate to a Gaussian distribution and thus give better overall

contrast. By application of an appropriate enhancement curve the grey scale of an IR image can be made linear with respect to the temperatures it represents.

Although a specific enhancement can be performed regularly on all images from a particular source, maximum flexibility in enhancement and other forms of processing is achieved through use of interactive techniques on a video display system. Such techniques are being used increasingly and various sophisticated image processors are now in general use. The Office has powerful systems available in Met O 19 and at RRL, and dramatic cost reductions in the systems will increasingly make them more readily available. These systems can be used to extract quantitative parameters from the image if this has been suitably calibrated. For example the user can determine the grey level counts for particular cloud top values and through use of a calibration table determine the cloud top temperature. Very sophisticated systems have been developed including those in which the operator can systematically use the image data to determine which areas are suitable for use of atmospheric sounding channels to determine atmospheric profiles in cloud free regions. The display device can also be used to determine cloud motion vectors with an operator interactively examining successive pairs of images to determine the movement of cloud from image to image. Generally speaking these interactive systems for extraction of quantitative information are backed by the automatic processing systems which will be described in the following paragraphs.

4. Automatic image analysis

Automatic systems for image analysis are a cost effective way of generating large numbers of quantitative products. The usual starting point is a histogram analysis of the pixel values. Arrays of size 32 x 32 pixels are often used, as the 1024 values provide a suitable statistical basis for analysis.

The one dimensional, single channel, histogram of Figure 1 illustrates the basic principles involved. Each source of radiation is assumed to have a characteristic radiative value, or signature, so that the sea might present a warm peak, in the histogram, and cloud at a particular level a cold peak. Of course no source will radiate a single value, for example the sea surface temperature will vary over the array area and clouds will have varying transparency as well as varying temperature. It is usually assumed that the radiative values are distributed normally about the source mean, so that the histogram can be considered to represent the sum of a number of Gaussian distributions, each associated with one source. The maximum value of the largest peak can be used to estimate the Gaussian variance and hence the total contribution of one source. This now allows the programme to associate a number of pixels with this source. They are removed from the array and the process repeated with a reduced number of pixels until all pixels have been associated with one of the histogram peaks. Each group of pixels is often described as a cluster, for which the mean value, variance, and number of pixels can be determined.

Of course a one-dimensional histogram cannot uniquely describe the radiative scene. In the visible image snow, cloud and desert may all have the same signature. In the thermal infra-red window channel at certain times of the day the sea may have the same temperature as the adjacent

land, and low clouds may also have the same temperature and hence the same radiative signature. For this reason extensive use is made of multidimensional histograms. Figure 2 illustrates a classical example of a VIS/IR histogram. Areas on the surface now correspond to particular sources of radiation. For example a dark warm peak could correspond to the sea, but a warm bright surface would be land or desert. Two-dimensional analysis still leads to some ambiguities, and the concept has been extended to include the use of 3 channels. The METEOSAT 6.3 μm channel is used to help resolve ambiguities in the identification of high clouds, the TIROS-N 3.7 μm channel helps to distinguish low cloud and fog from the surface, and some research is in progress on use of that channel in 3 channel histograms (Figure 3).

The histogram analysis generates a radiative signature in 2 or more channels for each cluster. The next stage in an automatic process is to assign each cluster to a physical source of radiation. This can be done by comparing the cluster means with predetermined values from known sources of radiation. For example it is easy to predict thermal radiances from the surface of the sea with sufficient accuracy from climatology to identify the infra-red sea cluster on most occasions. It is more difficult to predict the radiances from clouds because of their variable heights, and from land surfaces because of the diurnal variations, but the more advanced systems for image analysis use results of one analysis to help predict the radiance to be expected in the next image. The model therefore learns about diurnal variations and climatic effects as it works, provided that it is run sufficiently frequently and that it is not reinitialised for each run. The clusters have now all been associated with a physical source, and it is easy to see that a systematic analysis of this type can yield information on surface temperatures, cloud amount and the cloud top temperatures of several layers. However each radiative signature is not the radiation from the source, but the radiation reaching the satellite from that source. Therefore it is necessary to correct the radiance to account for atmospheric absorption before it can be used as a measure of source temperature. Several techniques are used for this correction. If the atmospheric temperature and humidity profile is known then the correction can be calculated, although this calculation can be subject to large errors if the water vapour content of the lower atmosphere is not known with high accuracy. Some systems use forecasts to predict the atmospheric conditions, and the forecast errors add to the uncertainty in the correction. The forecasts may be used indirectly, via a set of pre-computed look-up tables to save computing time, and this also introduces another error.

For these reasons alternative methods have been introduced to eliminate the atmospheric problem by instrumental means. The split IR channel on the AVHRR instrument is used for this purpose. The Along Track Scanning Radiometer (ATSR) instrument which the RAL hope to fly on the ERS-1 satellite allows two looks at a particular target from two different angles (through two different atmospheric paths) by an instrument which also has a split IR window channel. Use of such an instrument identifies the atmospheric contribution thus giving information both about the underlying surface and the atmosphere itself (for example precipitable water).

Another correction is needed for the transparency of clouds. Figure 4 illustrates the problem, and Figure 5 illustrates one solution. When cloud is semi-transparent the radiation reaching the spacecraft comes in part from cloud and in part from the underlying surface. This makes clouds appear too warm. One technique is to use the VIS channel to identify optically thick clouds and assume that these are not transparent, or to use the VIS channel to apply a correction to the IR data. Of course this is only possible during daylight. The METEOSAT 6.3 μm channel can be used at all times. The solid curve on Figure 5 shows the relationship between the 6.3 μm radiances and the 11 μm radiances for optically thick clouds. The curve can be obtained empirically or by theoretical analysis. The bi-spectral signature of a thick cloud will lie on this curve. Thin clouds will give a value which is warmer, that is below the curve. The value is assumed to lie on the straight line which connects the corrected radiance with that of the warmest cluster in the histogram (which is assumed to be non-transparent), hence the corrected radiance can easily be determined.

5. Cloud motion vectors (satellite winds)

5.1 A number of different satellite techniques for measuring winds have been tried in the past, but the only one to have been used operationally for any length of time is that in which the winds are derived from measurements of cloud displacements. The high repetition rate of images from geostationary satellites makes them well suited to this technique and so all 3 operators of geostationary satellites regularly compute and disseminate winds. The basis of the method is simple, identifiable cloud features are tracked from one image to the next and on the assumption that they move with the wind their displacements over a known period of time can be converted to wind speed and direction. This assumption is not always valid. For instance, development or decay of clouds may give the illusion of motion, movement of clouds may reflect the motion of synoptic systems rather than winds, orographic clouds may be stationary while a strong wind blows through them, and so on. Steps must therefore be taken, either in initial selection of the clouds to be tracked or in subsequent quality control procedures, to exclude all meteorologically unacceptable tracers. Another major difficulty concerns the relationship between the movement of cloud having significant vertical extent and the wind at a particular level. The clouds are viewed from above and their measurements relate essentially to the cloud top, but the movement of the cloud may be largely determined by the wind at some lower level. Various studies have been made of this problem, for example using an aircraft at the same time as detailed wind observations. These have determined that the oceanic trade wind cumulus generally move with the winds near the base of the cloud, whereas deeper clouds and higher level clouds generally move with the wind at some intermediate height between the top and base of the cloud.

Despite the unsuitability for wind determination of clouds that are developing or dissipating, it should be noted that indivdual small cumulus clouds could hardly be tracked anyway because the spatial resolution is not good enough. This does not mean that winds cannot be determined in areas of cumulus, sequences of pictures reveal a high degree of persistence, over periods of the order of an hour, in

the mesoscale patterns of trade wind cumuli, cumuli congestus etc. It is these patterns, and not the individual cloud cells, that are tracked as they are carried along with the wind.

Because of the uncertainties in interpretation of cloud displacements in terms of winds, the velocities derived from the displacements should strictly be termed cloud motion vectors (CMV) rather than winds.

There are three basic stages in the determination of CNV:

- Measurement of cloud displacement.

- Assignment of height.

- Quality control.

The details of implementation of the 3 stages differ between operators, although there is a good deal of common ground. The system used by ESA (European Space Agency) for METEOSAT is outlined below.

5.2 The ESA automatic method

The starting point is a sequence of 3 consecutive full disk infra-red images, the images being at 30 minute intervals. Steps in the process can be summarised as

- Image referencing

- Segment processing and tracer selection

- Wind vector determination

- Height attribution

- Manual quality control

- Final processing and dissemination.

These will be considered briefly in turn.

a. Image referencing

It is essential for accurate CMV determinations that there should be a high degree of precision in the relative registration of successive images. An error of only 1 IR pixel (ie approximately 5 km near the sub-satellite point) in the relative registration of two images one hour apart will produce an error of 1.4 m/s in the derived wind.

Image referencing is achieved by software which relates the actual image to the reference image (ie the image that would be obtained if the spacecraft was in its nominal position and orbit with no irregularities in its motion). This process is generally

called rectification, and uses a model the spacecraft dynamical characteristics and recent measurements of orbital parameters, together with measurements of the earth's horizon in each image.

b. Segment processing

This part of the processing programme essentially carries out the image analysis work described in paragraph 4 above in each of some 3,000 segments within 50° great circle arc of the sub-satellite point. Each segment is an array of 32 x 32 pixels. The process determines the availability of suitable cloud in each of the segments, together with the cloud top temperature and number of pixels associated with that cloud layer.

c. Wind vector determination

This is the heart of the process. Three consecutive IR images are used. A target segment is cut from the central image of the three (time T Hours) and a matching cloud pattern is sought in the image for T + $^1/_2$ hour. This is done mathematically using a cross correlation technique. The search area is made up of an array of 3 x 3 segments centred at the same position as the target segment (Figure 6). A strategy system is used to determine the highest correlation peak of the target segment in the search area. The same process is repeated for the image half an hour before the target image and the two correlation peaks compared to ensure that there is a mirror symmetry. A pair of peaks which exhibit suitable symmetry are then assumed to be the end point of the 1 hour wind vector which is computed by measuring the separation of the two correlation peaks. The wind thus computed has to be associated with the appropriate cloud layer and this is done by repeating the correlation process with enhanced images taking in turn radiance values close to all of the cloud layers which are present, to determine the maximum correlation peaks.

d. Height attribution

The techniques described in Section 4 of this Lecture indicate the corrections which are needed to compensate for atmospheric attenuation and for cloud transparency. These corrections are applied at this stage to give a corrected temperature for the cloud top. The next problem is to associate this temperature with an atmospheric height. In the case of METEOSAT winds this is done through use of forecast atmospheric profiles supplied by the ECMWF. Forecasts are used, rather than analyses, to ensure minimum time delay in the production of the final cloud motion vectors. Of course further errors can be introduced at this stage, not only are there errors in the corrected temperature itself, and in the forecast, but the forecast may not give a unique relationship between temperature and pressure. In particular, near the tropopause, small temperature errors can give rise to large height errors. For this reason the METEOSAT

winds are distributed with associated temperature and pressure values so that the user can choose to use the temperature as an indication of height rather than the pressure value.

e. Manual quality control

At the end of this process ESA, in common with all the other satellite operators, applies a manual quality control stage. This is achieved through use of an interactive display device in which a meteorologist can see the wind vectors superimposed on animated sequences of the images used in their generation. This allows him to determine which of the winds is associated with developing systems, or stationary clouds and he can delete such spurious wind vectors before distribution.

6. Measurement of sea surface temperatures

Measurements of sea surface temperatures are normally made on a routine basis by weather ships and by buoys. The disadvantage of these in situ measurements is that they are only representative of one particular point at one particular time. The expense of operating many ships or buoys deployed over a wide area to get good global coverage becomes prohibitive. Additional measurements are obtained by commercial "ships of opportunity", on passage. These are restricted to normal shipping routes and exhibit wide variations in observational techniques. One satellite in a sun-synchronous orbit can sample almost the entire globe twice a day with a scanning radiometer, permitting good spatial coverage to be obtained. The problem with satellite measurements is retrieving the sea surface temperature accurately enough to be of use. Uncertainties are introduced from many sources such as variable atmospheric absorption and scattering, clouds, sun glint, sea state and variable viewing geometry.

The 3 parameters which are most important when inferring a surface temperature from a radiative temperature measured at the top of the atmosphere are surface emissivity, absorption/emission of the intervening atmosphere and whether the measurement is contaminated by cloud. The emissivity of the sea surface is approximately 0.99 and varies only slightly with surface state and viewing angle. The estimation of atmospheric correction (the difference between the measured radiative temperature and that which would have been measured had there been no atmosphere) is a major problem in the retrieval of accurate SST. In the spectral window channels used the most important absorber is water vapour (in its monomer and dimer forms). The size of the correction therefore varies according to the amount of water vapour in the atmospheric column between the satellite and the surface, particularly in the lower layers where the absolute humidity is highest. At 11 μm the correction varies from a few tenths of a degree in very cold, dry atmospheres to values of around 5 K (but exceptionally up to 10 K) in the tropics. The corrections are smaller in the 3.7 μm window but the problems associated with reflected sunlight are such that this wavelength band is less reliable in the daytime. At 11 μm solar reflection is only a problem in a small area of the image close to the specular reflection point. The calculation of atmospheric correction is obtained by integrating the radiative transfer equation from the surface to space to determine the amount of radiation absorbed and emitted by the atmosphere. This requires a knowledge of the

temperature and humidity profiles. They can be obtained from climatology, a forecast model (as described for METEOSAT in the previous section) or preferably from a simultaneous retrieval using a sounding instrument (for example NOAA's Global Operational SST Computation or GOSSTCOMP system - see Brower et al, 1976). However, even with accurate profile information, the uncertainties in the atmospheric absorption still leads to a major part of the error in the retrieved SST. The absorption co-efficients in the window regions have some uncertainty because the absorption is mainly caused by the far wings of water vapour bands centred at distant wavelengths or by complex water vapour dimer spectra. (Imbault et al, 1981).

The third major source of uncertainty is contamination of the emitted surface radiances by clouds. At any one time approximately 50% of the sea surface is obscured by cloud. An effective cloud detection scheme must be employed in order to remove or correct cloud contaminated radiances. Various methods have been devised to detect cloud. During the day reflected visible radiances can be used to discriminate between clouds and cloud free areas. Bi-spectral methods as described in the previous sections have been used operationally for METEOSAT, which can also make use of the water vapour channels at night. Another technique recently developed is the spatial coherence method (Coakley and Bretherton, 1982), which use the small scale variability of the measured radiances to detect cloud.

An SST data set (GOSSTCOMP) is produced operationally by NOAA and is derived from the calibrated AVHRR brightness temperatures at 3.7, 11 and 12 μm wavelength. Regression relationships have been derived which allow the surface temperature to be inferred from the multispectral data at the top of the atmosphere. The difference in brightness temperature between the different channels is a measure of the atmospheric absorption/emission. An example of a typical GOSSTCOMP product is given in Figure 7 which shows a plot of the monthly mean SST between 55 W and 180 W over the northern hemisphere for the month of March 1982.

An operational SST product is also derived from METEOSAT data, currently within 50° of the sub-satellite point, which is disseminated over the GTS twice a day after quality control. An example of this product is shown in Figure 8.

Estimation of the accuracy of satellite measured SST is difficult. When comparing against ship measurements it must be remembered that:

- Ship observations have their own errors,

- Ship observations are point measurements whereas satellite data are area averages,

- Ships measure the bulk temperature from a depth in a mixed layer at a depth of from between 3 to 9 metres, whereas satellite data refer to the uppermost fraction of a millimetre (the skin). This occasionally gives a difference of up to 3° K in areas of low surface wind, but in a well mixed boundary layer errors in the satellite SST from other sources are larger than the bulk-skin differences.

At present, under the best conditions, the root mean squared differences between ship and satellite data is around 1.5 K RMS. A comparison of the NOAA multichannel satellite SST against buoy measurements over a 6 month period is shown in Figure 9, which shows significantly reduced root mean squared differences during the day due to better cloud detection algorithms. The RMSD over this longer time period are reduced to 0.6 K.

Recent studies have been made into making near coincident measurements of the sea surface temperature from Nadir view and a few minutes later from an oblique view through the atmosphere. The atmospheric correction can then be inferred from the different brightness temperatures from each viewing angle. The Along Track Scanning Radiometer (ATSR) is currently being developed to try out this double view concept on the ERS-1 satellite. It will make two measurements in each of the 3 infra-red channels at similar frequencies to AVHRR. The predicted standard deviations for ATSR are 0.36 K during the day and as low as 0.10 K at night (Harries et al, 1983) so a further improvement over existing multichannel methods now seems likely.

The problems described above have been concerned with deriving an accurate absolute value of SST. For some purposes the relative distribution in sea surface temperature is more interesting than the absolute value. Figure 9 shows an AVHRR 11 μm image in the region of the British Isles on 12 July 1979 enhanced to show small changes in SST. Areas of sudden transitions in SST are termed fronts and the position of some of the more intense fronts are marked in Figure 9. Oceanographers make much use of these enhanced IR images to study the development and dissipation of these fronts (Simpson and Bowers, 1979).

Finally, measurements of land surface temperatures can also be made (Browning, 1982) but a good knowledge of the surface emissivity has to be known in order to determine absolute measurements. Land surface temperature varies rapidly with time, so that the infra-red data from geostationary satellites is more useful here, allowing measurements at the time of maximum and minimum surface temperatures.

Values of thermal inertia can be determined from the rate of change of surface temperatures, and are useful for inferring soil moisture quantities, surface vegetation, and surface insolation values.

7. Other products

Although cloud motion vectors and sea surface temperature data are the most familiar operational products, there are many other parmeters being produced on a routine basis by some or all of the satellite operators. Some examples include:

a. Cloud analyses. For example the METEOSAT product, which is a set of GTS bulletins, describes the cloud amount and cloud top temperatures in each 150 km segment. A similar product is being developed on a global basis as part of the International Satellite Cloud Climatology Programme (ISCCP). Calibrated maps of cloud top height are also transmitted by METEOSAT as pseudo images. Manual and objective nephanalyses are also available from a number of sources.

b. Precipitation Indices. Cloud imagery contains some information regarding the occurrence and intensity of precipitation. The absence of cloud over long period is an obvious indicator of the absence of precipitation, and there are various techniques (Barrett and Martin 1981) for more positive measurements. The simplest technique is to correlate the cloud top temperature with rainfall rates, and precipitation indices based on this method achieve correlations of around 0.7 with six hourly rainfall averages in the tropics. Higher 'scores' can be achieved by use of the visible channel as an aid to the identification of thick (ie precipitating) clouds, but of course this is only possible during daylight. Other algorithms incorporate information about the rate of growth of clouds, their movement and structure. These techniques are well suited to small scale events which could lead to local flash floods, but the coefficients used are affected by topography and other local conditions and these more sophisticated techniques have not been used globally.

8. Conclusion

This lecture has introduced the range of products which can be derived from satellite imagery. Cloud motion vectors and sea surface temperatures have gained operational acceptance, other products are coming into use and the possibilities have by no means been exhausted, so that further developments and increasesd accuracy can be expected.

The accuracy of current operational products have been reviewed in Lecture 6.

J Morgan
AD Met O(SM)

February 1984

References

Barrett, E C and Martin D W 1981. The use of satellite data in rainfall monitoring.

Brower R L, Gohrband H S, Pichel W G, Sigmore T L, Walton C C 1976. NOAA Tech. Memo. NESS 78. Satellite derived sea surface temperatures from NOAA spacecraft.

Browning K A 1982. Extremely low temperatures over England and Wales observed by METEOSAT 2. Weather 37 p 79.

Coakley J R and Bretherton F P 1982. Cloud cover from high resolution scanner data. Detecting and allowing for partially filled fields of view. J. G. Res. 87 C7 p 4917-4932.

Desbois M, Seze G and Szejwach G 1982. Automatic classification of clouds on METEOSAT imagery Application to high level clouds. J. Appl. Met. 21 p 401-412.

Harnes J E, Llewellyn Jones D T, Minnett P J, Saunders R W and Zavody A M 1983. Phil. Trans. R. Soc. Lond. A309 p 381-395.

Imbault D, Scott N A, Chedin A 1981. Multichannel radiometric determination of sea surface temperature: Parametrization of the Atmospheric Correlation. J. Appl. Met. 20 556-564.

McClain E P, Pichel W G, Walton C C, Ahmad Z, and Sutton J 1983. Multichannel improvements to satellite derived global sea surface temperatures. Adv. Space Res. 2 p 43-47.

METEOSAT System Guide 1980 ESA publication (ESOC/MDMD).

Simpson J H and Bowers D 1979. Shelf sea fronts. Adjustments revealed by satellite IR imagery. Nature 280 p 648-651.

Idealised schematic of the one dimensional histogram analysis concept. The segment description gives the predicted radiances at the top of the diagram. The real segment yields an observed histogram which is processed to produce the underlying Gaussians. These are then matched with the predicted values and hence with the physical source.

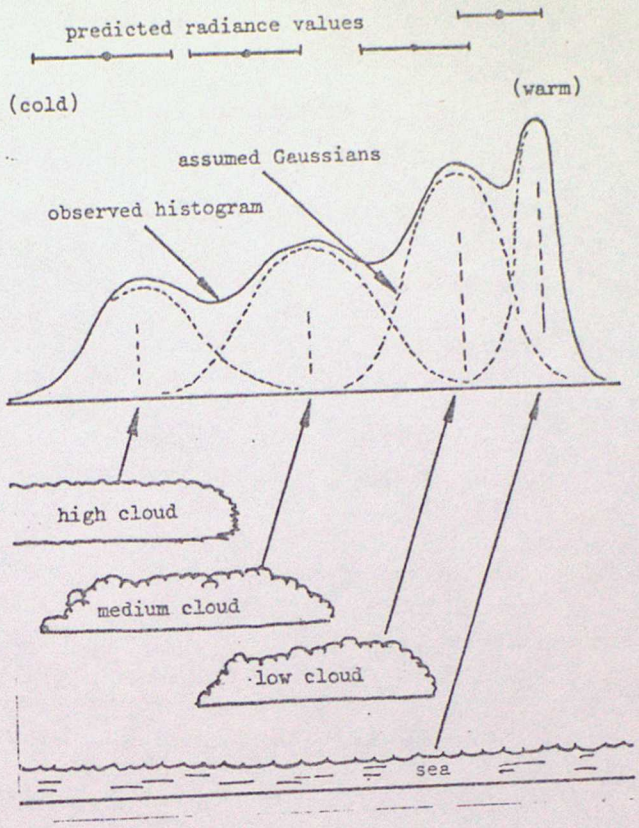

Each predicted radiance value is compared with each of the cluster values, and identified with one of them by reference to both measured and predicted means and to the standard deviation of the predicted radiance.

The program also stores the differences between the predicted and observed values. These differences are used to refine the prediction for the next run, and thus the algorithm learns by experience.

Figure 1.

One dimensional histogram analysis

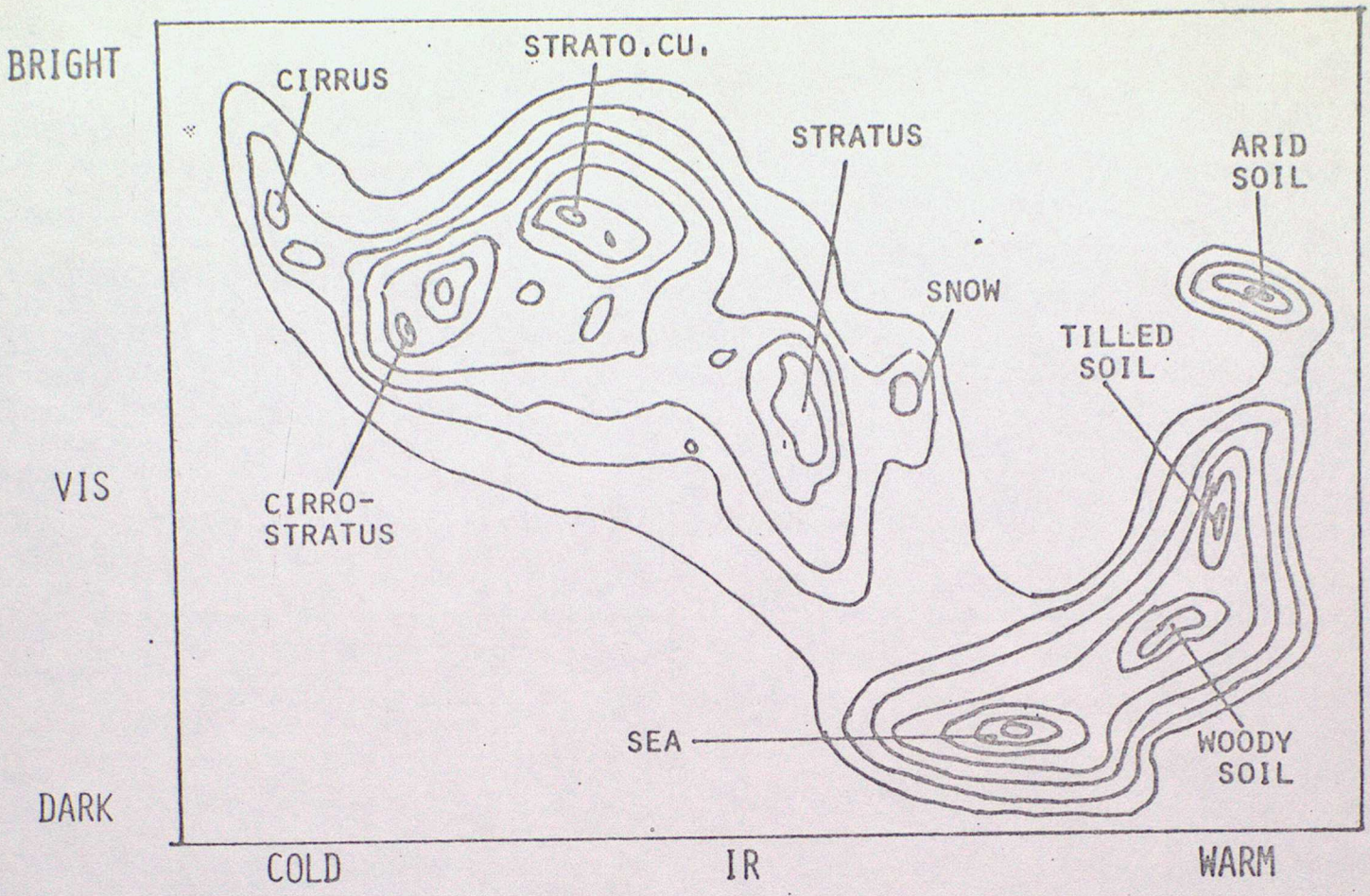

Figure 2: Two dimensional histogram

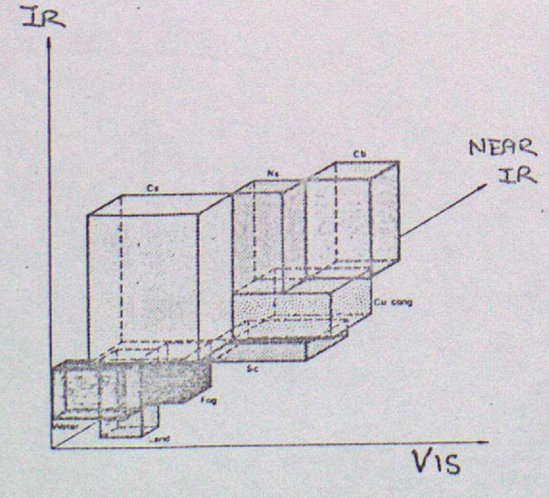

Figure 3:
Three dimensional histogram

Figure 4 : The transparency problem.

Radiation from thick cloud (a) gives a low radiance value corresponding closely to the cloud top temperature. Pixel (b) has a high radiance value associated with the warmer sea surface. The thin cloud (c) and (d) is semi-transparent, and hence the radiation reaching the spacecraft is composed partly of high and low radiances. The net radiation in pixel (c) or (d) is therefore over estimated - it is too warm. This could lead to serious errors of height attribution, in the case of thin cirrus cloud, but is corrected by use of the WV (6 μ) channel.

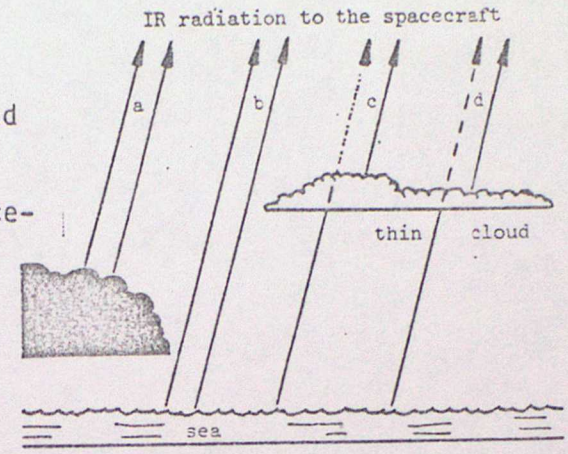

FIGURE 5 : THE SEMI-TRANSPARENCY CORRECTION

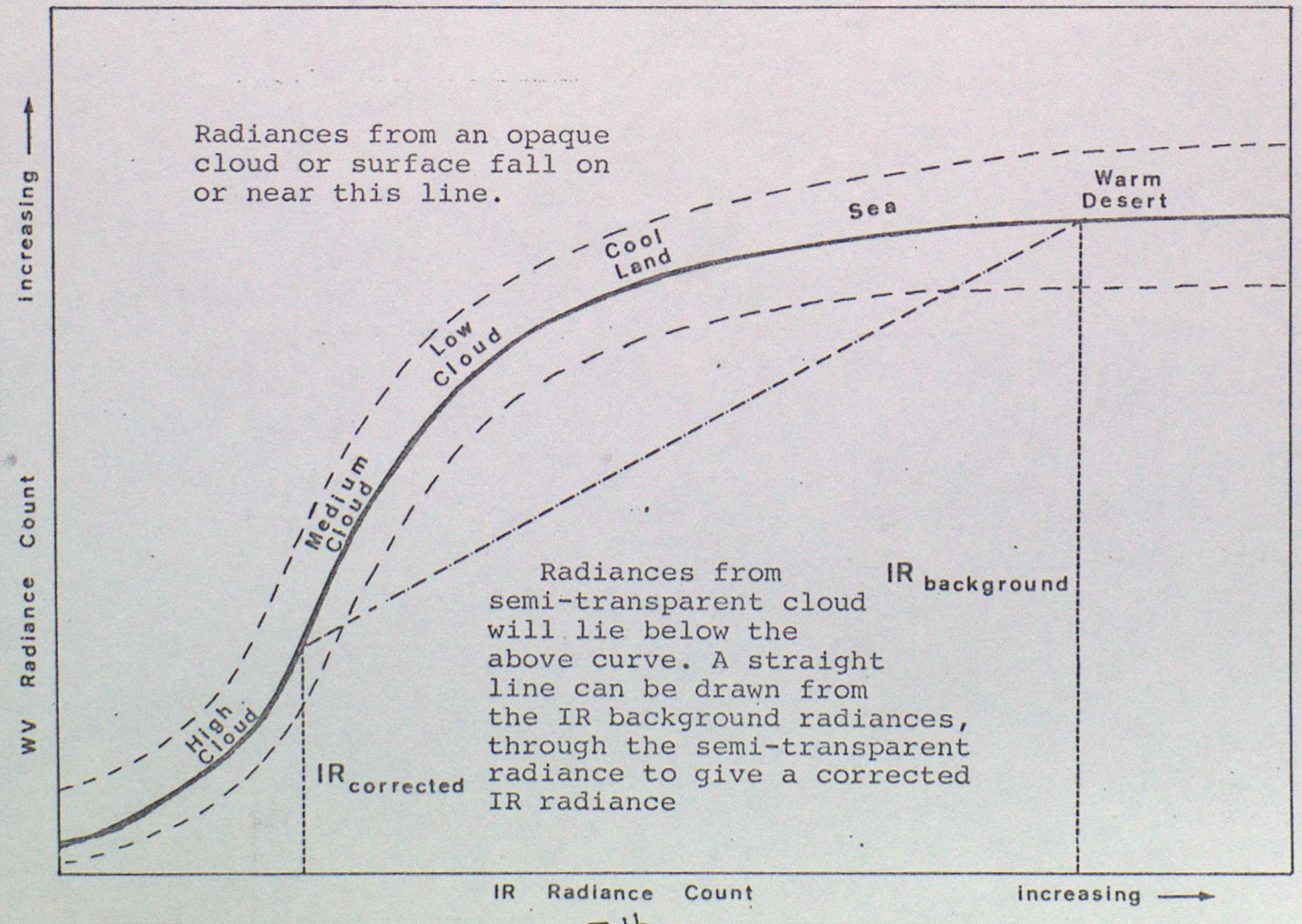

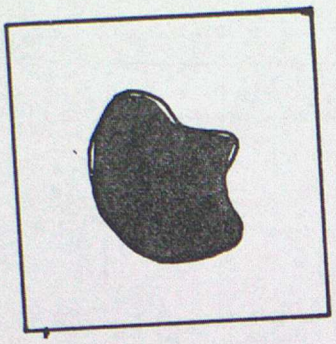

SEGMENT CUT FROM
CENTRAL IMAGE (T_o)

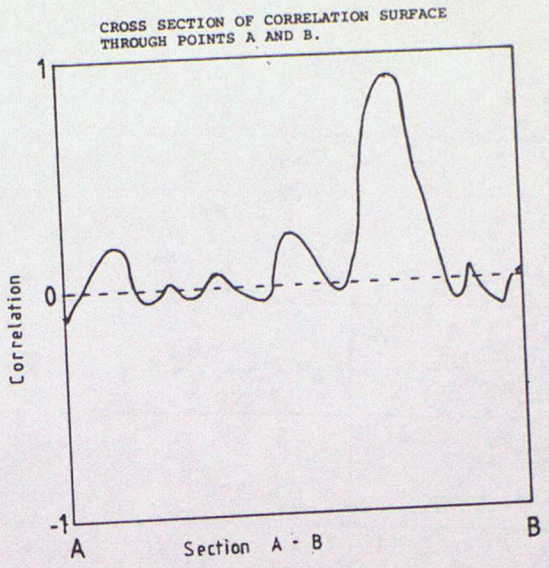

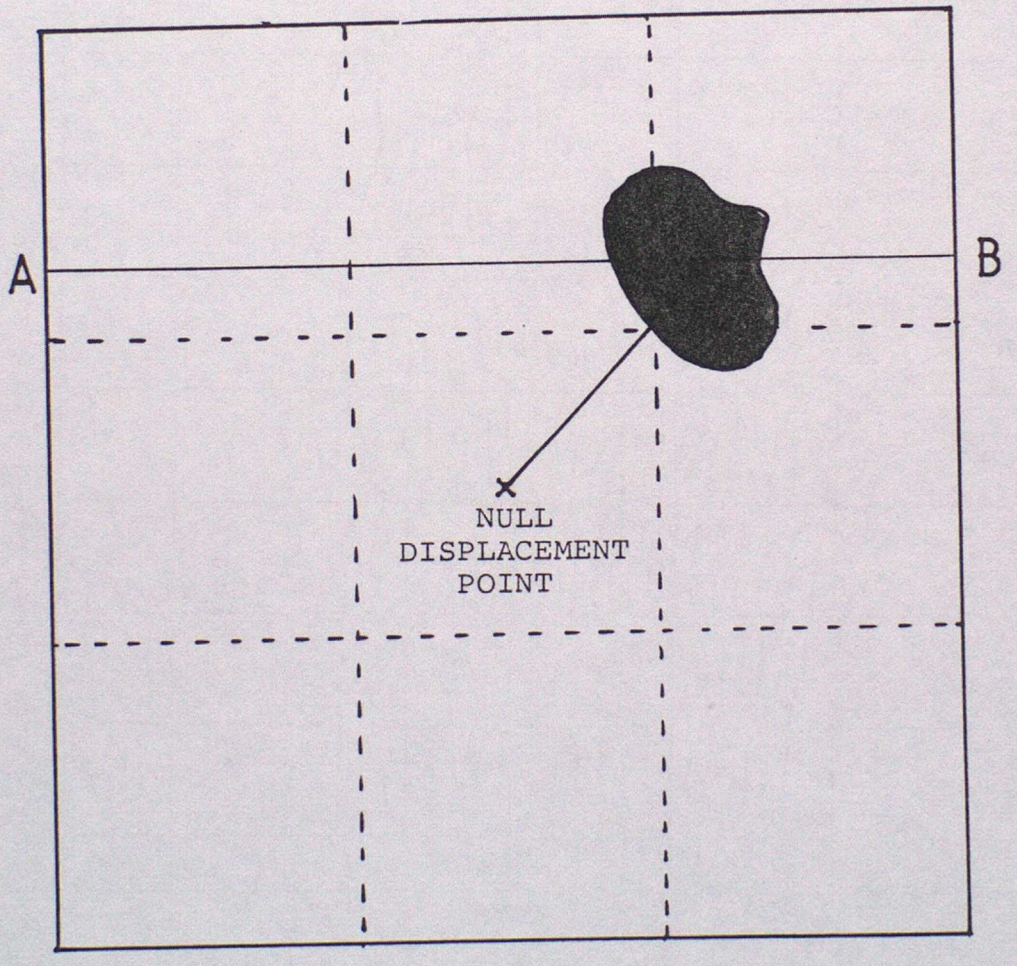

3 X 3 SEGMENT WINDOW FROM IMAGE
(T_o + 30 MINUTES)

Figure 6 : Correlation displacement of cloud element

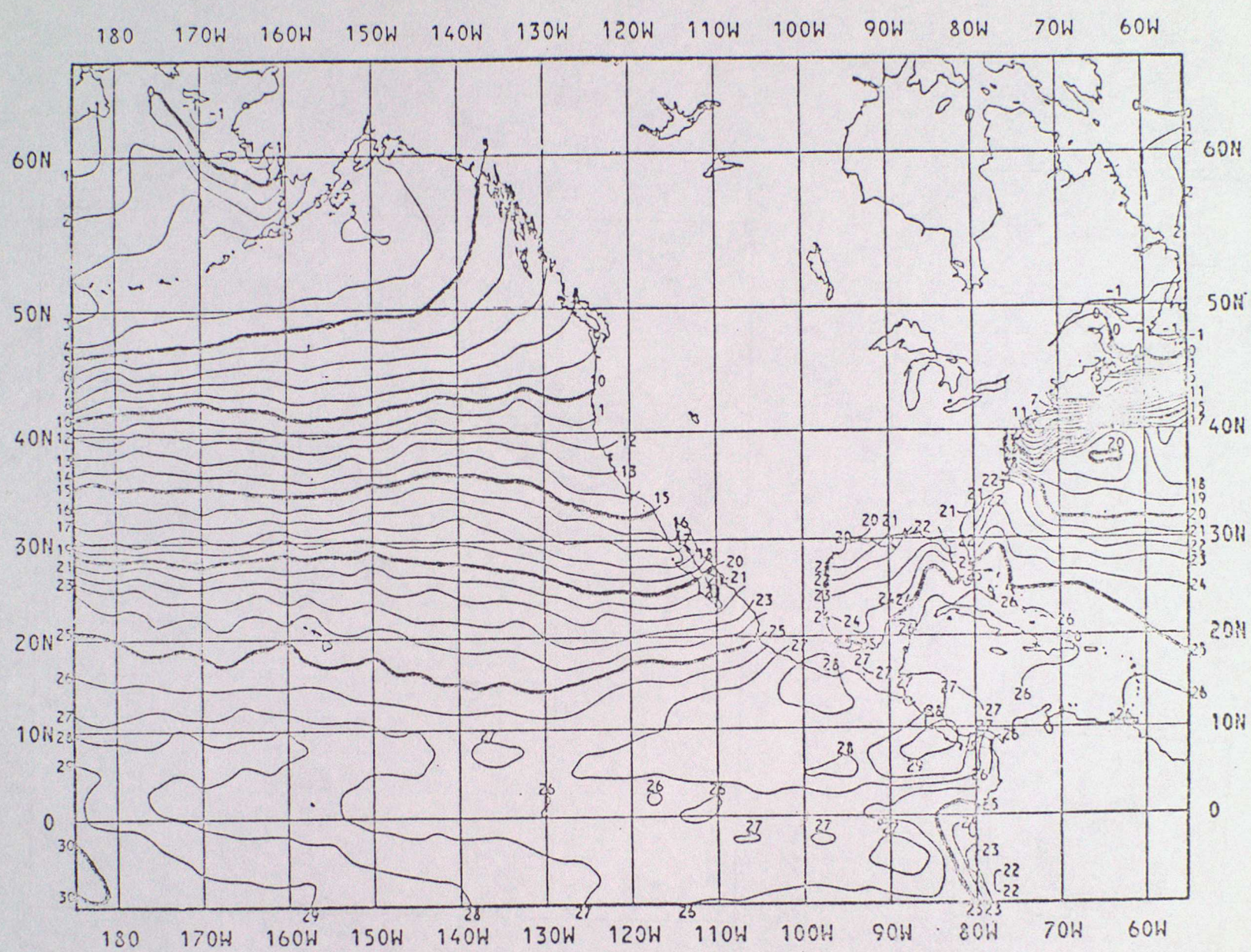

Contours of 1°C satellite monthly mean SST for March 1982.

Figure 7: Example of GOSSTCOMP product

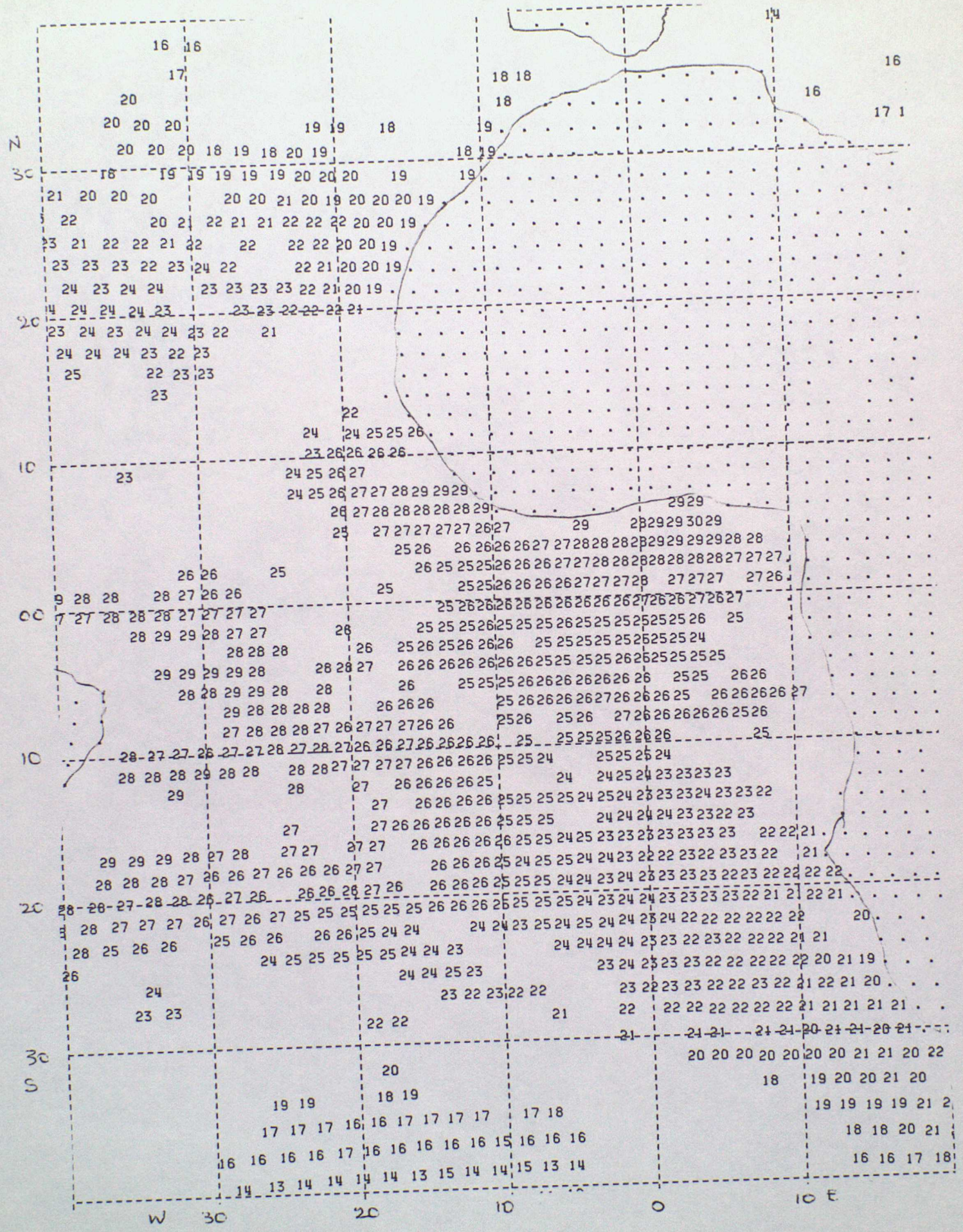

Figure 8: Example of METEOSAT SST product
(13 Jan 1984)

Figure 9 TIROS-N AVHRR 11μm infrared image of the British Isles at 1424 GMT on 12th July 1979. The image has been enhanced to show up small changes in sea surface temperature; (black-warm, white-cold). Two prominent fronts are indicated.

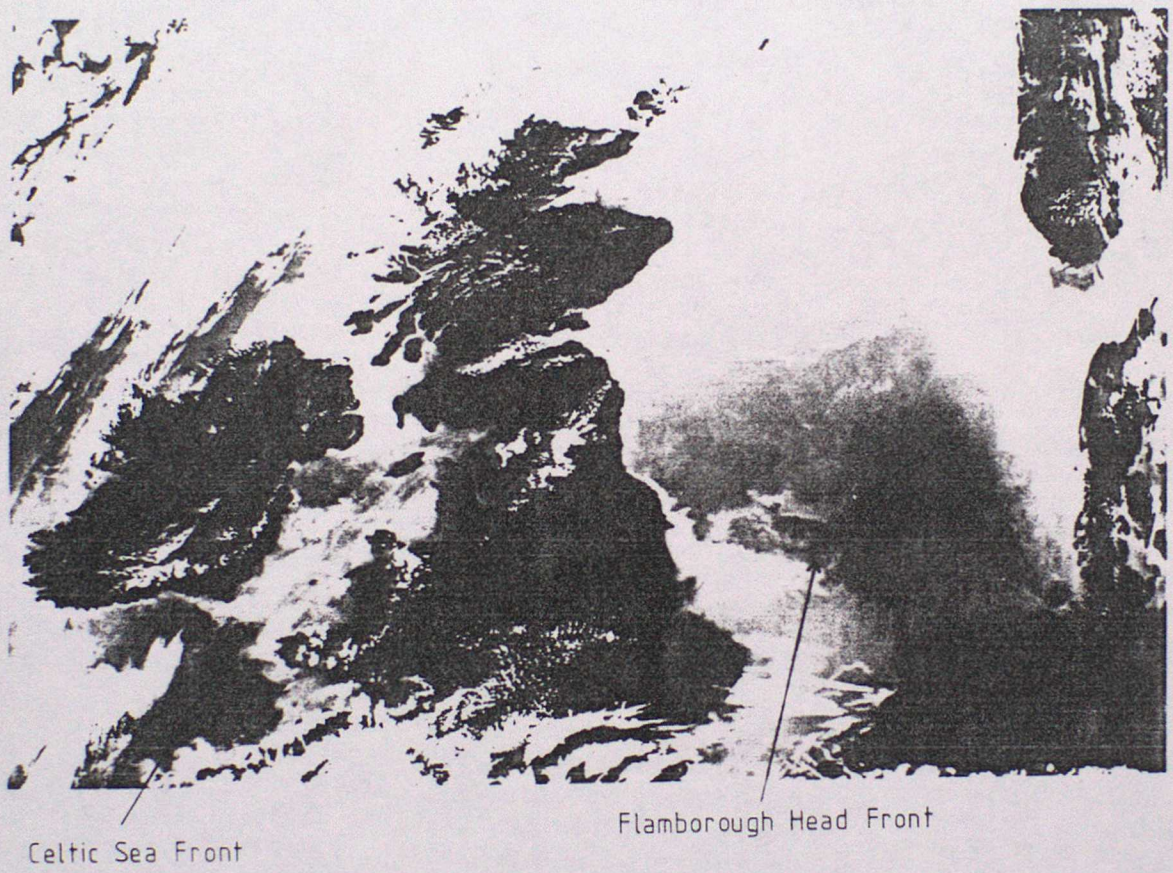

S.O. COURSE ADVANCED LECTURES, 1984.
SATELLITE METEOROLOGY.

THE ACTIVE MICROWAVE INSTURUMENT ON ERS-1.

D. Offiler, Met O 19.

1. Introduction.

This lecture will describe the Active Microwave Instrument (AMI), which is to be flown on the first European remote sensing satellite ERS-1. This instrument has three modes of operation: as a wind scatterometer, (wind vector measurements), wave scatterometer (wave spectrum measurements) and a synthetic aperture radar (SAR - a high resolution imaging radar).

Since the wind measurement mode will be of most interest to the Office, this aspect of the instrument will be described in most detail. The background to the "scatterometry" technique will be given, and reference will be made to the predecessor to the AMI, the SEASAT-A Satellite Scatterometer (SASS) instrument. The quality and usefulness of such wind measurements will be reviewed by showing the results from an analysis of SASS measurements and conventional observations taken during the Joint Air-sea Interaction (JASIN) experiment.

2. The theoretical and experimental background to scatterometry.

As soon as microwave radar became widely used in the 1940's, it was found that at low elevations, surrounding objects and terrain caused large echos, obliterating the signals from targets of interest. There is a similar effect at sea, caused by reflections from waves, and this unwanted signal became known as sea (or ground) "clutter". Ever since, designers and users of radar equipment have sought to reduce this noise [1]. However, researchers investigating this effect found that the backscattered signal from the sea became larger with increasing wind speed, opening the possibility of remotely measuring the wind and so encouraging further investigation [2,3,4].

The backscattering is due to resonant reflections from a rough surface: for incidence angles of more than about 20 deg. from the vertical, this occurs when the Bragg condition is met:

$$\Lambda \sin \theta_i = n \lambda / 2$$

where Λ is the surface roughness wavelength, λ is the radar wavelength, θ_i the incidence angle and n=1,2,3.... First order Bragg scattering (n=1) at microwave frequencies ($\lambda \sim$ 2cm) arises from small capillary waves superimposed on the larger gravity waves. These capillary waves are generated by the instantaneous surface wind stress.

The level of backscatter from an object is usually expressed as the Radar Cross-section (RCS or σ) which is defined as "the area intercepting that amount of power which, when scattered isotropically, produces an echo equal to that of the object" [5]. For extended targets, such as the sea surface, the backscatter is expressed as the Normalised Radar Cross-section (NRCS or sigma-zero - σ°), which is the RCS per unit area. In terms of other known or measureable radar parameters,

$$\sigma^\circ = \frac{64\,\pi^3 R^4}{\lambda^2 L_s G_o^2 (G/G_o)^2 A} \cdot \frac{P_R}{P_T}$$

where R is the slant range to the target of area A, λ is the radar wavelength, L_s includes atmospheric attenuation and other system losses, G_o is the peak antenna gain with G/G_o the relative gain in the target direction. P_T is the transmitted power and P_R the received power. This is often referred to as the Radar Equation. (Sigma-zero is usually measured in decibels - i.e. σ° (dB) = 10 $\log_{10}$ σ°)

Experimental evidence from wind-wave tanks and scatterometers on static platforms, aircraft and satellites operating over the ocean show that sigma-zero increases with surface wind speed, decreases with incidence angle and is dependent on the beam azimuth angle relative to the wind direction [6]. It is generally lower for horizontal polarisation than for vertical, and the dependence of sigma-zero on radar frequency appears to be small over the range 5-20GHz. It has also been suggested that sigma-zero may be affected by surface temperature (surface tension and/or viscosity effects) and low level atmospheric stablity, though these effects are probably small and have not yet been experimentally verified.

Figure 1 is a smoothed plot of combined Skylab and aircraft scatterometer sigma-zero (for vertical polarisation, at 30 deg. incidence angle and at Ku-band - around 14GHz.) against relative wind direction for various wind speeds. Direction 0 deg. corresponds to looking upwind, 90 deg. crosswind and 180 deg. downwind. As yet, no theoretical basis exists which completely explains the sigma-zero signature with wind speed, direction, incidence angle, polarisation and radar frequency. Empirical sigma-zero model functions can be fitted to these curves of the form:

$$\sigma^\circ = a_o(U,\theta_i,P) + a_1(U,P)\cos\phi + a_2(U,P)\cos 2\phi \quad \text{dB}$$

or:

$$\sigma^\circ = G(\phi,\theta_i,P) + H(\phi,\theta_i,P)\log_{10} U \quad \text{dB}$$

where the coefficients a_o, a_1 and a_2 are proportional to $\log_{10}$ U, and they (or G and H) are derived by regression from measured backscatters in areas where the wind vector is known. U is the wind speed, ϕ the relative wind direction, θ_i the incidence angle and P is vertical or horizontal polarisation.

Originally, the values of these coefficients were based on aircraft measurements, with the conventionally measured wind speeds referenced to a common height of 19.5m (although sigma-zero is more closely related physically to the surface friction velocity, u*). These measurements were made at Ku-band, in support of the SEASAT SASS instrument which operated at that frequency, and new data from the SASS itself has enabled the SASS model coefficients to be optimised [6]. The ERS-1 AMI will operate at C-band (around 5GHz), and the SASS coefficients will not be correct at that frequency. An ESA sponsored campaign has just been conducted during January and February 1984 to allow C-band coefficients to be determined. This has involved several scatterometers from different countries being flown over the North Sea and off Brittany with conventional meteorological data being observed from nearby towers and ships.

Since sigma-zero shows anisotropy with wind direction, measuring sigma-zero at two or more different azimuth angles in principle allows both speed and direction to be retrieved. This is the method used by the SEASAT SASS, the ERS-1 AMI and other designs of wind measuring scatterometer.

3. The SASS instrument.

The SEASAT scatterometer used two fore and two aft radar beams, directed 45 deg. either side of the sub-satellite track, to form a cross-shaped pattern of illumination on the ground, as shown in Figure 2. The beam widths (half-power) were 0.5 deg. in the horizontal plane and about 25 deg. in the vertical, forming a swath 500km wide on each side. (There were actually two extensions to this "primary" swath: an inner one of 0-8 deg. incidence angle, not direction sensitive, and one 55-65 deg., expected to be sensitive only to high wind speeds.)

Using the motion of the spacecraft, Doppler filtering of the return signal was employed to divide the swath into 12 cells. For each measurement period (~2s), 61 RF pulses at 14.6GHz were integrated for ~300ms, with a further 500ms noise integration measurement. The value P_R in the Radar Equation is then:

$$P_R = P(\text{signal+noise}) - P(\text{noise only})$$

Several modes of antenna/polarisation switching were possible, for example, mode 1 sequence was antenna no. 4 V-pol, then 1V,3V,2V. In all cases, a backscatter made in a particular cell by a forward beam would be followed a few minutes later by one from the rearward beam on the same side at (almost) the same geographical location. The registration is not exact due to the Earth's rotation in the time between the two orthogonal measurements [7,8].

4. Retrieval of wind vector.

The derivation of wind vectors from the raw instrument telemetry involves a series of complex algorithms. In general terms, these perform the tasks of:

* Earth locating each cell from the orbital data and Doppler filter frequencies, and determining the cell area and slant range.

* calculating the ratio of received power to transmitted power, after calibrating both.

* determining the values of system losses and antennae gain for the cell from pre-flight and in-flight calibrations.

* calculating sigma-zero from the Radar Equation and correcting this for atmospheric attenuation derived from the passive microwave radiometer (SMMR) also on SEASAT [9,10] and for other instrumental biases.

* match fore and aft cells to form sigma-zero orthogonal pairs.

* fit the two backscatter measurements to the model to derive a wind vector.

Due to the harmonic nature of backscatter with wind direction, there can be up to four 'solutions' of wind speed and direction for each cell. Each solution has a similar wind speed value, but can have widely different wind direction values. Often, these occur in pairs separated by about 180 deg.

5. Assesments of the SASS accuracy.

The SASS was designed to measure the surface wind vector over the ocean to an accuracy of 2m/s (or 10%, whichever is greater) in speed and 20 degrees in direction, over the range 4-25m/s and for all directions. In order to validate the actual accuracies achieved by each instrument, a special exercise, the Gulf of Alaska SEASAT Experiment (GOASEX) was undertaken, involving several oceanographic ships and buoys and an aircraft carrying a similar scatterometer [11,12]. Comparisons with this surface data showed that the SASS generally measured the winds to the required accuracy, but some large biases remained. These results were used to update the processing algorithms and coefficients [6].

Coincidentally, the Joint Air-Sea Interaction (JASIN) project took place in the North Atlantic (between Scotland and Iceland) [13], within the three-month lifetime of SEASAT, and while all of its instruments were operating correctly. This set of surface observations had a high spatial and temporal resolution, was of a sufficiently high quality and included a

reasonable range of meteorological conditions to properly assess the SASS performance. Results from a small number of orbits passing over the JASIN area showed the SASS accuracy to be around 1.6m/s and 18 deg., and with much smaller biases than with GOASEX. [14,15]. After the SASS-JASIN Workshop which produced these results, the sigma-zero/wind vector model coefficients were again refined. The Jet Propulsion Laboratory (JPL), who were responsible for SEASAT data, have processed the complete set of scatterometer winds using this latest "SASS-1" algorithm, including atmospheric corrections from the SMMR where the swaths overlap.

Met O 19 have made a thorough investigation of the SASS winds [16], using all the SEASAT orbits which passed through the JASIN area during the two months of that experiment; a short description of our study is given below.

The Institute of Oceanographic Sciences (IOS) have collated much of the JASIN data and quality controled it as far as possible, but the winds still refer to the height of each anemometer - from 2.5m to 23m asl with the platforms used. In order to be compatible with the SASS data, all wind speeds were first adjusted, assuming neutral stability, to a common height of 19.5m, following the procedure in [17]. Each SASS wind was then paired, if possible, with a JASIN observation within 60km and 30 minutes; there were a total of 2724 such pairs from 132 SEASAT orbits. As mentioned earlier, each SASS measurement may produce up to four solutions for wind direction; for the purposes of this study, the one closest in direction to the JASIN observation was taken.

From each "colocated" pair of wind estimates, the standard deviation of the SASS minus JASIN differences ("SDD") in speed, direction and vector differences were calculated. Figure 3 shows scatter plots of SASS vs. JASIN wind speed (a) and direction (b) for the whole colocation set. Overall, the SASS agrees with the surface observations to 1.7m/s and 17 deg., well within the SASS design goals. The mean differences were also small, being less than 0.1m/s and 3 deg.

Further analyses have been performed, dividing the data according to the values of various parameters such as swath position or wind speed. Figures 4, 5 and 6 show the variation in SDD with incidence angle (inner to outer edge of the swath), wind speed and wind quadrant, respectively. A similar analysis with respect to the radar polarisation used for each measurement (both beams horizontal polarisation, vertical or mixed) showed very little difference between these modes. Except in the speed range 12-16m/s (Figure 4 - due particularly to one anemometer having a short averaging period and also overspeeding) and in one quadrant (Figure 5), the 2m/s and 20 deg. design criteria were met in all these sub-categories.

6. Synoptic examples.

6.1 4 August: thunderstorm case.

There was only one occasion during JASIN when the wind speeds measured from the SASS were clearly in error by more than 10m/s. This occured during orbit 557 at 2315 GMT on 4 August 1978, near the southern vertex of the JASIN triangle. This swath for horizontal polarisation is shown in Figure 7, together with the nearby JASIN observations for 2300 GMT and other surface measurements taken at midnight. The analysis is based on the midnight CFO subjective analysis. SASS values ranged from 6 to 22m/s, while the JASIN measured wind speeds were about 4m/s, with little variation before and after the satellite pass. At 2300 GMT, ship Meteor reported light drizzle with thunder during the previous hour.

An investigation by IOS and JPL [18] shows that other nearby JASIN ships Discovery and Shackleton also reported thunderstorm activity, with Discovery logging heavy rain just after the pass. Their analysis of the SASS backscatters showed that during the previous pass 100 minutes earlier, there were high values in this area, coincident with deep convective clouds on the SEASAT VIRR imagery. Radiosonde profiles indicated potentially unstable air behind the surface occlusion. It seems likely, therefore, that the SASS measurements were affected by a thunderstorm associated with deep convection on the occlusion, and may have had several causes:

* SASS was operating correctly and measuring locally high winds, such as a gust front or downdraughts from the convecting cell(s).

* Large raindrops or hail stones caused increased sea-surface roughness, invalidating the backscatter/wind relationship.

* Raindrops, normally considered to attenuate microwaves, were large enough to cause additional backscatter, with possibly some contribution from a "bright band".

Since none of the many ships and buoys in the area (some sampling every minute) recorded any strong winds or gusts, the first possiblity mentioned is unlikely. Considering the possible rainfall rates and convection cell dimentions, either of the two other causes - or both - could have been responsible for these anomalous SASS winds.

6.2 31 August: cold front case.

This case serves to illustrate the usefulness of satellite-derived winds because of their density of observations over a swath. Figure 8 shows the synoptic situation at midnight GMT on 31 August 1978 (a) and the wind field (b), both from the old 10-level model objective analysis on a 100km grid. Fronts have been added manually according to the CFO subjective

analysis for the same time. The low pressure over Iceland had been moving north-eastwards, bringing its associated fronts over the JASIN area by midnight.

SEASAT orbit 930 passed just south of Iceland at 0050 GMT, enabling the port swath to measure winds across JASIN, as shown in Figure 9. Also marked are the JASIN observations (at 0100 GMT) and analysis. Ship Meteor's winds had veered by 30 deg. during the previous hour and Tydeman's by 50 deg. in the following hour, showing the cold front to be between them. In this case, the surface frontal zone shows clearly in the SASS winds as a line of cells with only two solutions, marking the transition between the wind directions on either side of the front.

With experience, synoptic features such as fronts, and especially low pressure centres can be accurately positioned, even with the present level of ambiguity. Subjective analysis of the wind field has been successfully demonstrated by meteorologists working experimentally on SASS data alone, in the United States [14,19].

7. The AMI instrument.

The European Space Agency's first remote sensing satellite, ERS-1, is expected to carry the Active Microwave Instrument (AMI), a radar altimeter and an Along-Track Scanning Radiometer (ATSR). This spacecraft is due to be launched in 1988, and is to be an "operational demonstration" mission. That is, while not operational in the Met O 2 sense, it is intended to process the data as accurately as possible and deliver it to the user within 3hrs of being observed. An impression of the spacecraft is shown in Figure 10.

The AMI is a combined wind scatterometer and synthetic aperture radar (SAR), with a special SAR mode operating as a "wave scatterometer", that is 2-dimensional wave spectra can be deduced. The three modes of operation are briefly described below.

7.1 Wind scatterometer.

The wind scatterometer part of the AMI is very similar to the SEASAT SASS instrument in concept. However, instead of having only two beams per measurement cell, AMI will have three, the extra one being at 90 deg. to the sub-satellite track. The swath is divided into 50km cells by range-gating, rather than Doppler filtering, and there is only a single sided swath, 400km wide, as shown in Figure 11. The three cells will be accurately registered on the Earth's surface by contantly steering the satellite about its yaw axis. The design accuracy of the wind scatterometer is similar to that of the SASS, i.e. wind speed to 2m/s and direction to 20 deg. over the range 4-24m/s and all angles. (The swath will actually have a 500km width, but this level of accuracy is not guaranteed for the extra 4 cells.)

The third beam will allow the level of ambiguous wind "solutions" to be greatly reduced. While SASS mostly produced four solutions, simulations show that the AMI can be expected to have up to 80% of its measurement cells with no more than two solutions, and that where there are two solutions, these will be close to 180 deg. apart. Depending on the detail of the C-band model resulting from the measurement campaign mentioned earlier, 40-60% of all measurements may have unique solutions.

Figure 12 shows the likely wind-scatterometer coverage for one day (a), and for comparison, the actual positions of all marine wind observations for one day (b). The orbit shown is one that will repeat its ground track exactly every 3 days, and is the nominal mission orbit. Figure 13 shows how this orbit tracks over the North Sea, together with an extreme one with a 35-day repeat - i.e. it would take 35 days to complete the coverage shown. This type of orbit is to favour the radar altimeter which is a narrow-swath, nadir-only instrument.

7.2 The SAR.

The SAR is a very high resolution imaging radar, having a pixel size of around 25x25 metres, over a swath of 80km. This resolution is relatively easy to achieve in range - normal time-slicing of a short pulse is used - but to get that resolution in azimuth would require a very large antenna, several kilometers in length. In a SAR, this large size is simulated by illuminating the target for several seconds while the satellite moves across it (the spacecraft ground speed is nearly 7km/s). A point target in the field of view can be tracked by the phase changes (equivalent to a Doppler shift) in the return echo. Very complicated algorithms are needed to invert the complex signal to an image. To do this digitally within a realistic time requires large computing power. For instance, to process 10 minutes'-worth of raw SAR data into an image within 3 hrs. would require a computer equivalent to the Cyber or Cray.

As with wind scatterometry, the primary scattering is from the small capillary waves, but the measured sigma-zero is modulated by the larger gravity waves. The large cell size of the wind scatteromter averages out this modulation, whereas the very small resolution of the SAR allows waves to be "imaged". Internal waves and under-water sand banks can also be seen in SAR images, since they can affect the surface modulation.

Of course, with such a small resolution, the SAR data rate is very high, about 100Mbits/s, far too high to be recorded on-board. The power consumption is also high, so this instrument can only be operated for a short time (~10 mins. per orbit), and in sight of a receiving station.

7.3 The wave scatterometer.

If a SAR image is Fourier transformed, the result is a 2-D image spectrum of the waves in the spatial image. Peaks are seen which show the dominant wavelength and its direction (with

180 deg. ambiguity). The wave scatterometer is a "cut-down" operating mode of the full SAR, in which small samples of the ocean, 5x5km, are taken every 100km. In this way, the average power used and data rates are much lower. The wave mode can be operated continuously with the wind mode, and can be recorded on-board. The "image" and Fourier transform could be also calculated on-board (though it is more flexible to do this on the ground), and the resulting product will be a wave spectrum from 100m to 1km wavelength (in 12 logarithmically-spaced steps) with 20 deg. angular resolution. The spectrum energy density is expected to be accurate to 25%.

REFERENCES

1. Harrold, TW, 1974. Ground clutter observed in the Dee weather radar project. Met. Mag., 103, p.140.

2. Jones, WL and Schroeder, LC, 1978. Radar backscatter from the ocean: dependence on surface friction velocity. Boundary Layer Met., 13, p.133.

3. Krishen, K, 1971. Correlation of radar backscattering cross sections with ocean wave height and wind velocity. J. Geophs. Res., 76, p.6528.

4. Ross, D and Jones, WL, 1978. On the relationship of radar backscatter to wind speed and fetch. Boundary Layer Met., 13, p.151.

5. Long, MW, 1975. Radar reflectivity of land and sea. Lexington Books, Lexington, Mass., USA.

6. Schroeder, LC, Boggs, DH, Dome, G, Halberstam, IM, Jones, WL, Pierson, WJ and Wentz, FJ, 1982. The relationship between wind vector and normalised radar cross section used to derive SEASAT-A satellite scatterometer winds. J. Geophys. Res., 87(C5), p.3318.

7. Grantham, WL, Bracalente, EM, Jones, WL, Schrader, JH, Schroeder, LC and Mitchell, JL, 1975. An operational satellite scatterometer for wind vector measurements over the ocean. NASA Technical Memorandum X72672, NASA Langley Research Center, Hampton, Vir., USA.

8. Johnson, JW, Williams, LA, Bracalente, EM, Beck, FB, Grantham, WL, 1980. SEASAT-A Satellite Scatterometer instrument evaluation. J. Ocean. Eng., OE-5, p.138.

9. Bracalente, EM, Boggs, DH, Grantham, WL and Sweet, JL, 1980. The SASS scattering coefficient o algorithm. J. Ocean. Eng., OE-5, p.145.

10. Moore, RK, Birrer, IJ, Bracalente, EM, Dome, GJ, and Wentz, FJ, 1982. Evaluation of atmospheric attenuation from SMMR brightness temperatures for the SEASAT satellite scatterometer. J. Geophys. Res., 87(C5), p.3337.

11. Jones, WL, Black, PG, Boggs, DH, Bracalente, EM, Brown, RA, Dome, G, Ernst, JA, Halberstam, IM, Overland, JE, Peteherych, S, Pierson, WJ, Wentz, FJ, Woiceshyn, PM and Wurtele, MG, 1979. SEASAT scatterometer: results of the Gulf of Alaska Workshop. Science, 204, p.1413.

12. NASA, 1980. SEASAT Gulf of Alaska Workshop II report. Report No. 622-107, Jet Propulsion Laboratory, Pasadena, Cal., USA.

13. Royal Society, 1979. Air-sea Interaction project: summary of the 1978 field experiment. London.

14. NASA, 1980. SEASAT JASIN Workshop report: Vol 1, Findings and conclusions. Report No. 80-62, Jet Propulsion Laboratory, Pasadena, Cal., USA.

15. Jones, WL, Boggs, DH, Bracalente, EM, Brown, RA, Guymer, TH, Shelton, D, and Schroeder, LC, 1981. Evaluation of the SEASAT wind scatterometer. Nature, 294, p.704.

16. Offiler, D., 1982. Surface wind measurements from satellites - a comparison of SEASAT scatterometer data with JASIN surface winds. Met. O. 19 Branch Memorandum No. 64, Meteorological Office (unpublished manuscript - copy available in the National Meteorological Library, Bracknell).

17. Pierson, WJ, 1978. Verification procedures for the SEASAT measurements of the wind vector with the SASS. Report to JPL contract 954411, Cuny Institute of Marine and Atmospheric Sciences, City College, New York, USA.

18. Guymer, TH, Businger, JA, Jones, WL and Stewart, RH, 1981. Anomalous wind estimates from the SEASAT scatterometer. Nature, 294, p.735

19. Wurtele, MG, Woiceshyn, PM, Peteherych, S, Borowski, M and Appleby, WS, 1982. Wind direction alias removal studies of SEASAT scatterometer-derived wind fields. J. Geophys. Res., 87(C5), p.3365.

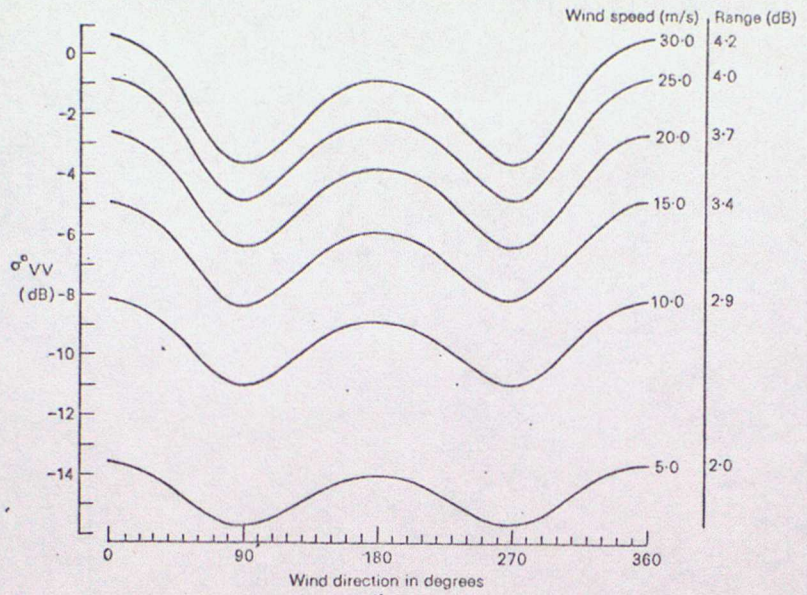

Figure 1. Backscatter cross-section, σ° against relative wind direction for various wind speeds. Vertical polarisation at 30 deg. incidence angle.

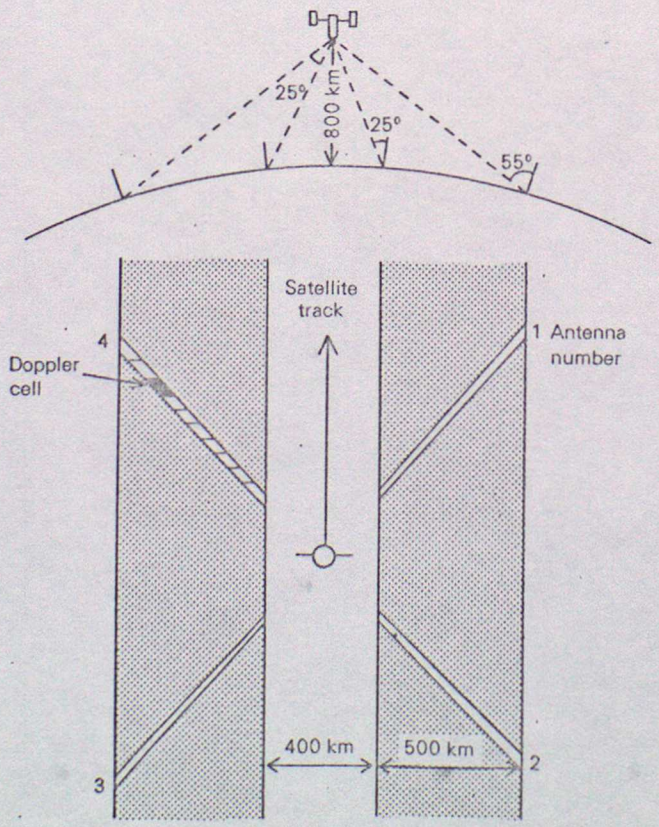

Figure 2. The SASS viewing geometry: section in the plane of beams 1 and 3 (top diagram); beam illumination pattern and ground swath (bottom diagram). SASS operated at 14.6GHz (Ku-band) and a set of Doppler filters defined 15 cells in each antenna beam. Either horizontal or vertical polarisation measurements of backscatter could be made.

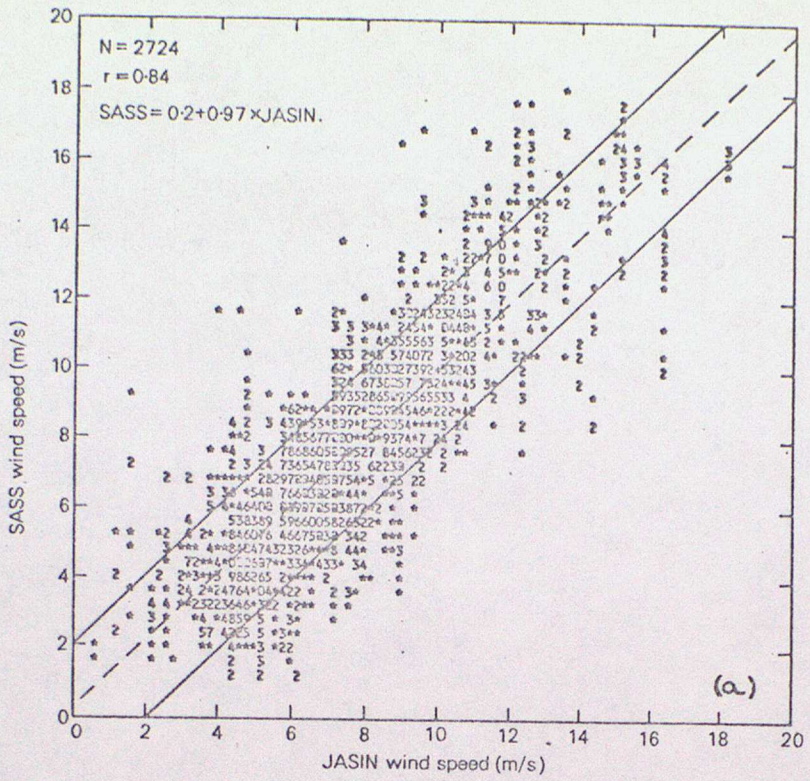

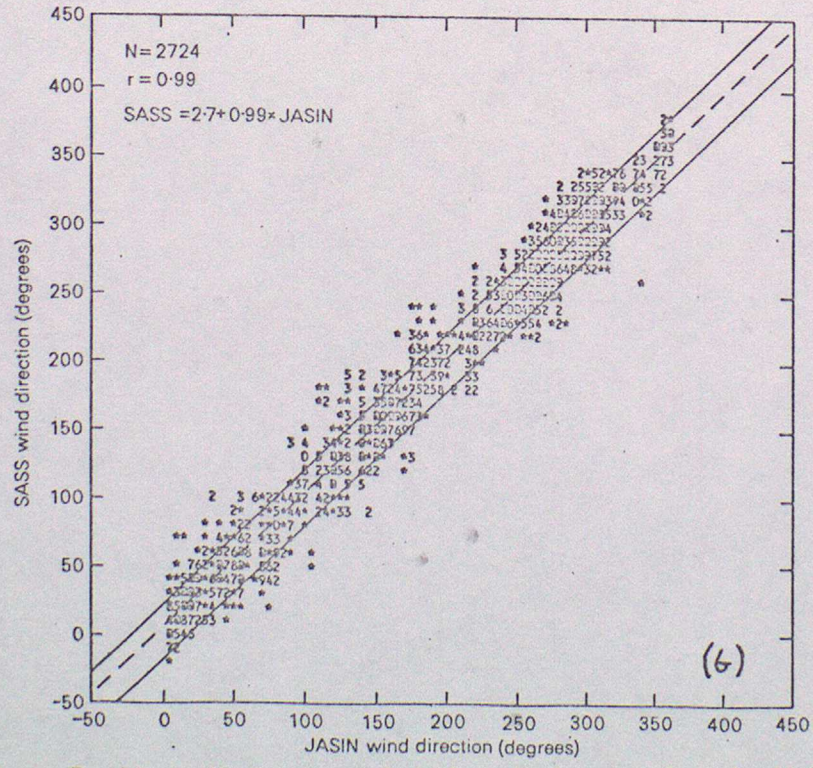

Figure 3. Scatter diagrams of (a) wind speed and (b) wind direction measurements made by SASS against colocated JASIN observations. The design rms limits of 2m/s and 20 deg. are indicated by the solid parallel lines and the least-squares regression fit by the dashed line. KEY: '*' = 1 observation pair, '2' = 2 coincident observations, etc., '0' = 10, '@' = more than 10.

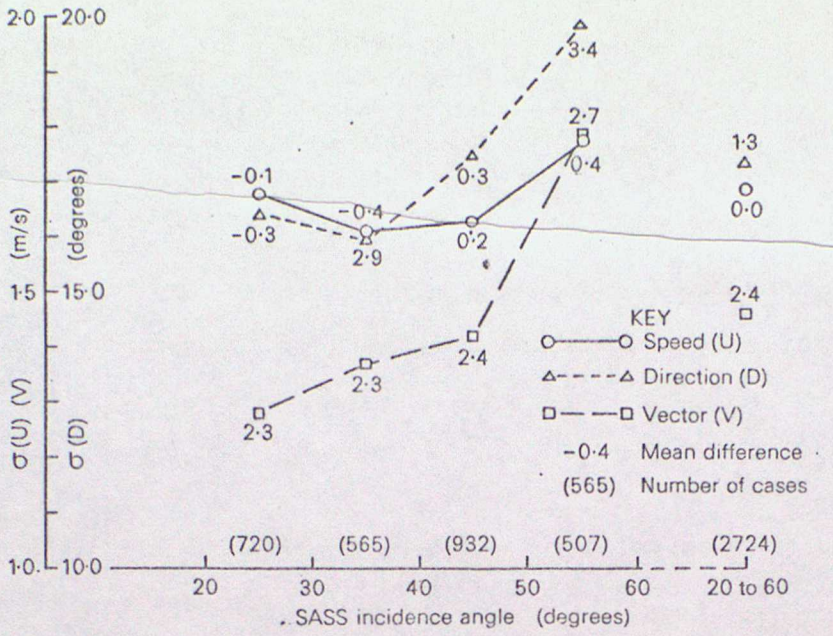

Figure 4. Standard deviations of SASS-JASIN wind speeds, directions and vector differences against bands of SASS incidence angles.

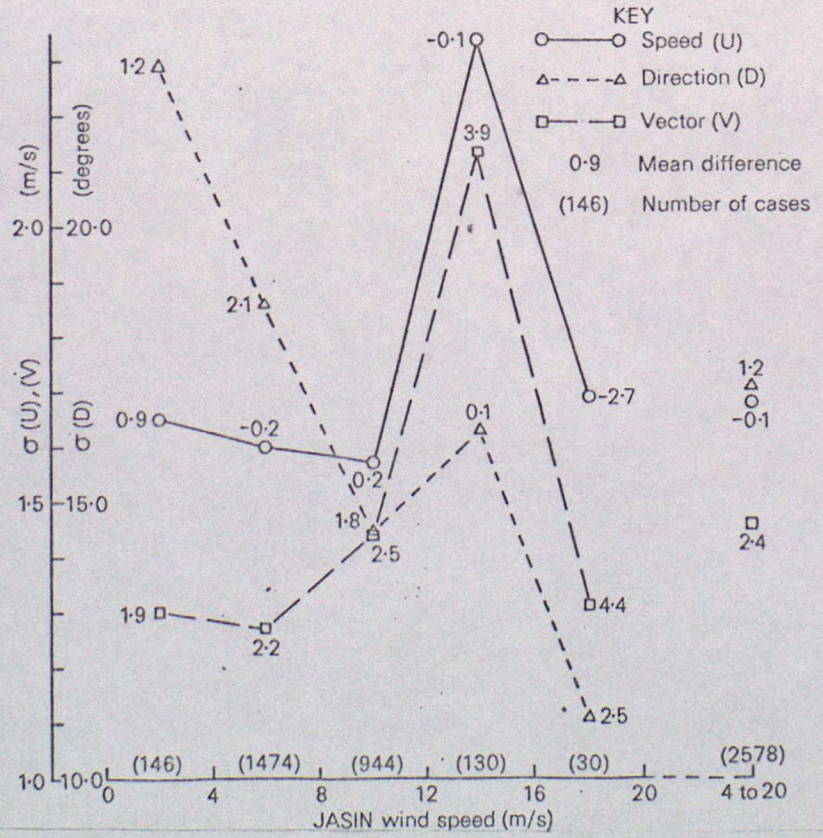

Figure 5. As Figure 4, against bands of JASIN wind speed.

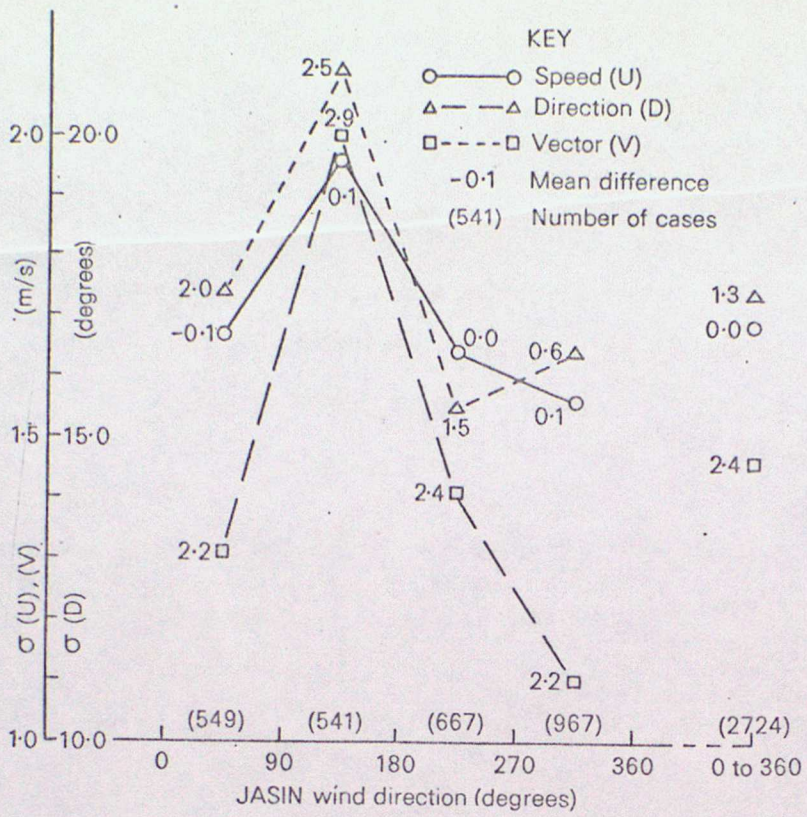

Figure 6. As Figure 4, against JASIN wind quadrant.

FIGURE 7. SASS ANOMALY 4TH AUGUST 1978. (H POL)

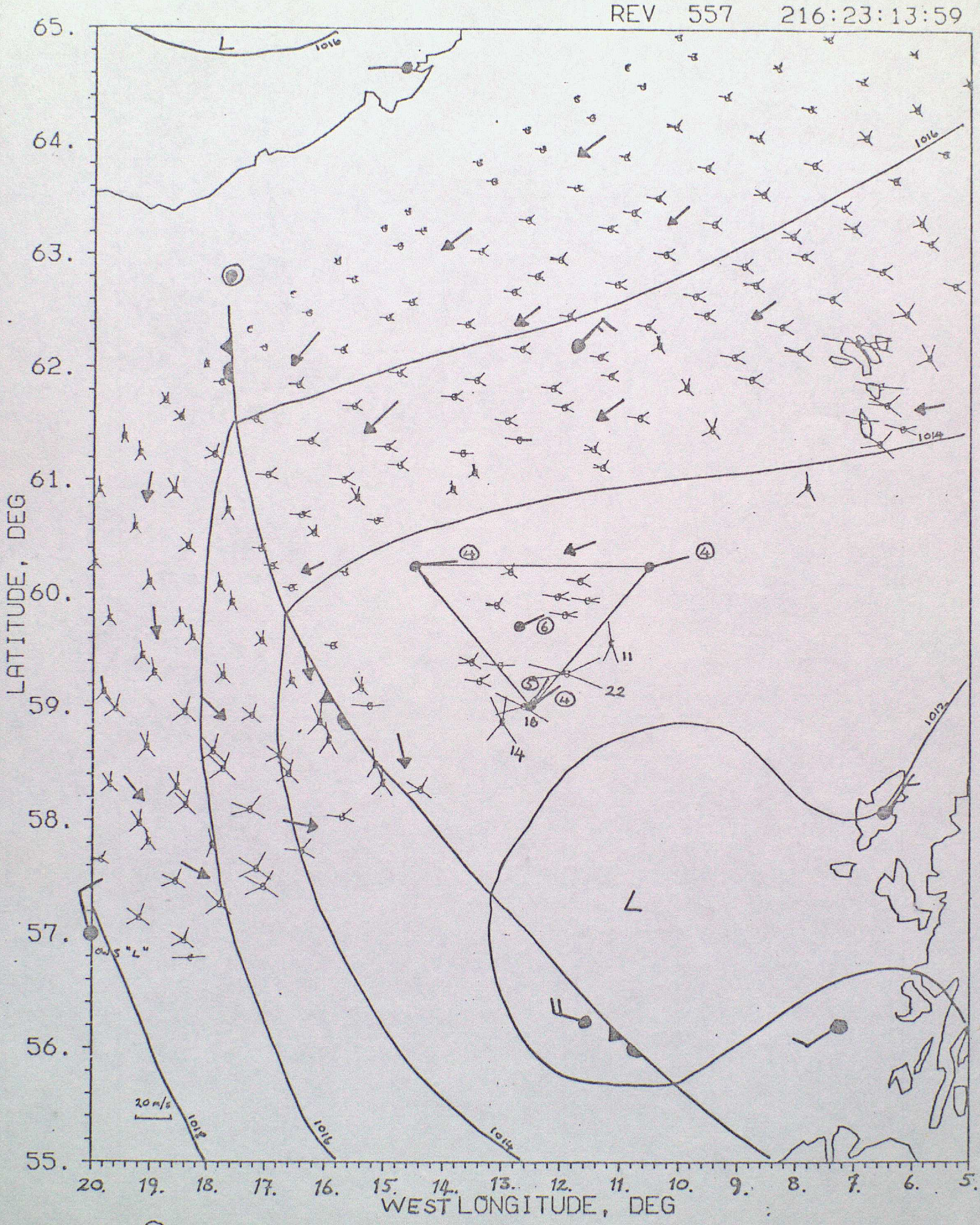

④ - JASIN wind direction and speed in m/s at 23Z : ⌐ - other obs. at 00Z 5th.

← - General wind flow at the surface : 22 - SASS wind speed in m/s

Figure 8(a)

MSL PRESSURE

00Z 31/8/78

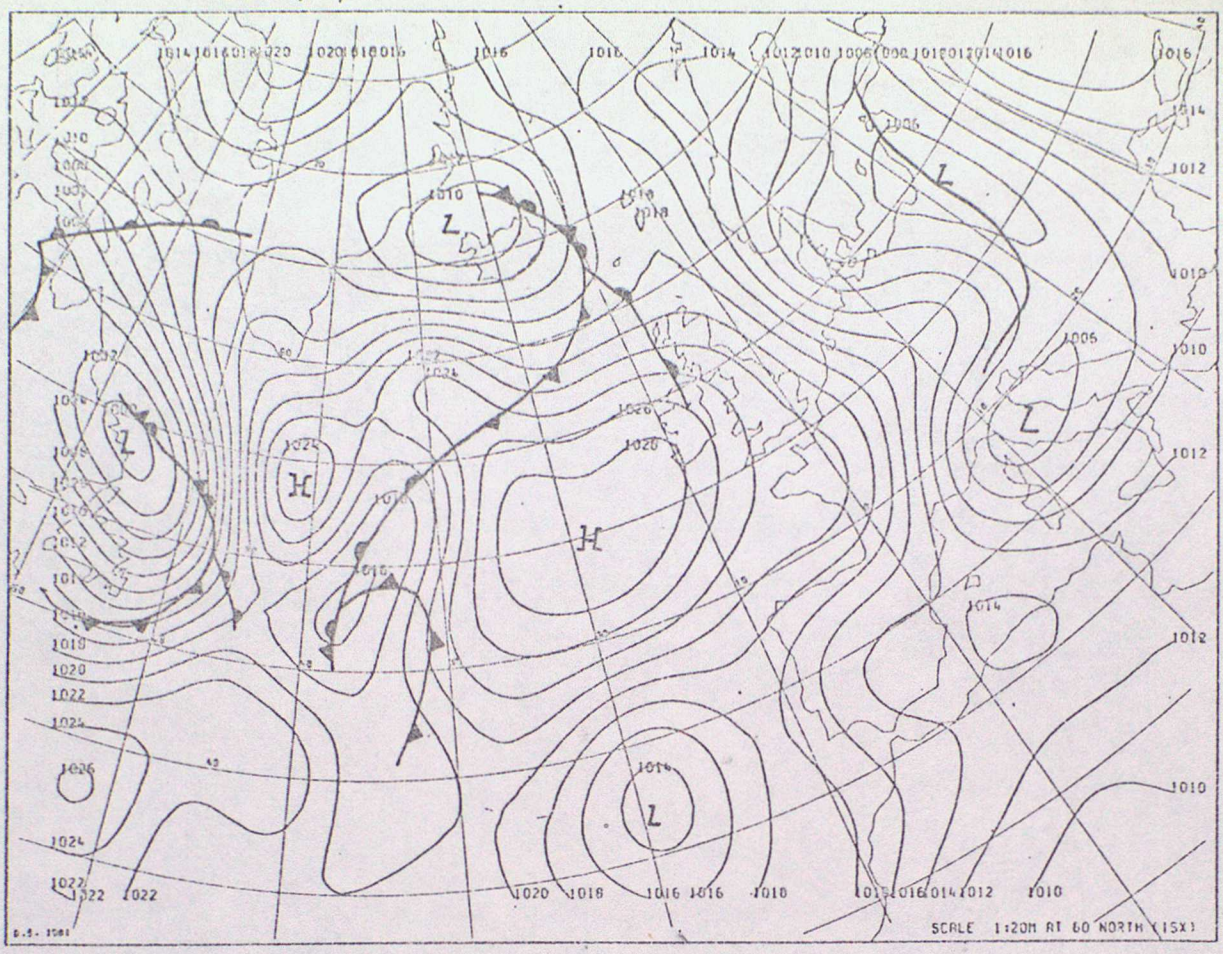

Figure 8(b)

1000MB VECTOR WIND

00Z 31/8/78

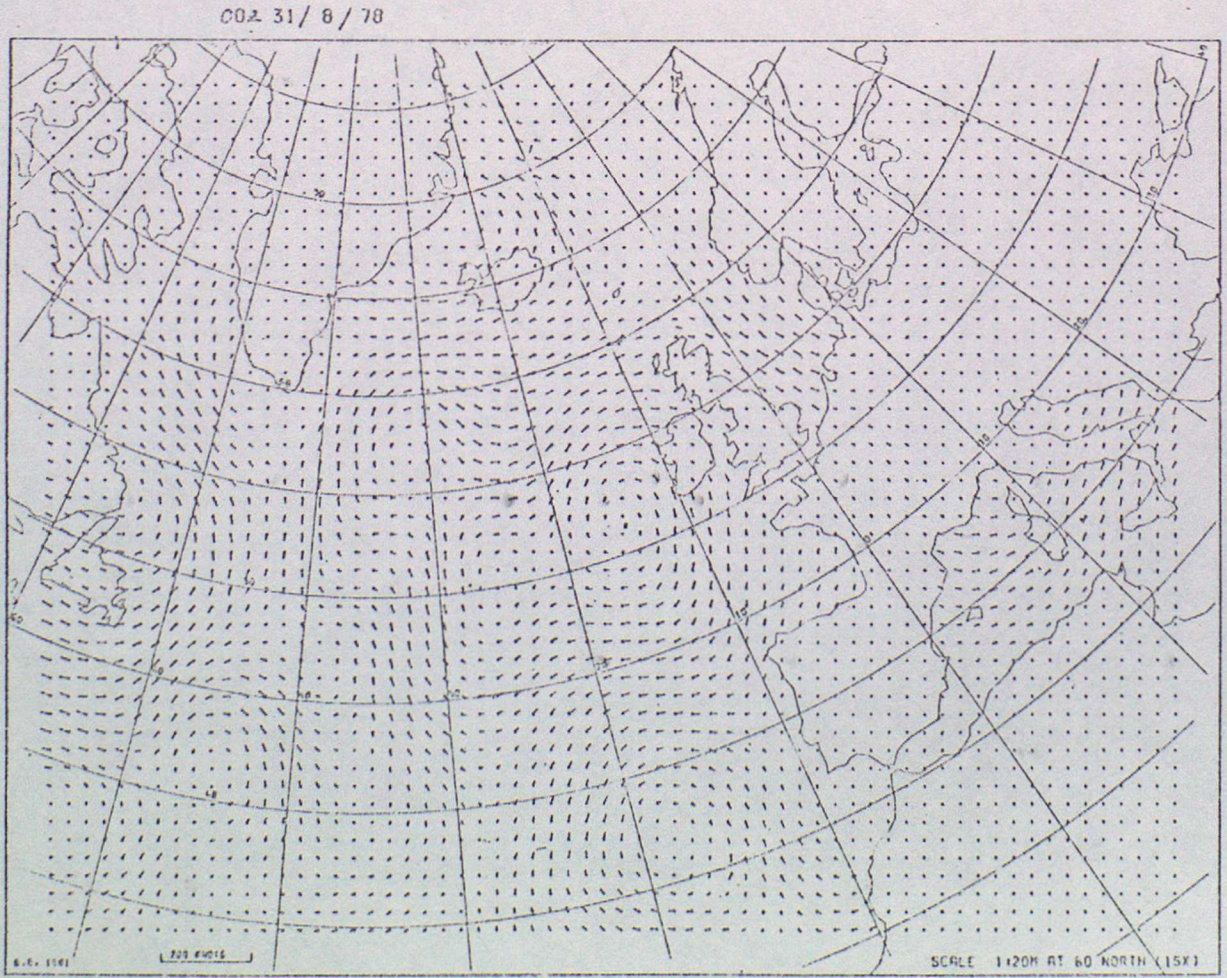

FIGURE 9. COLD FRONT 31ST AUGUST 1978 (V POL)

REV 930 243: 0:49:43

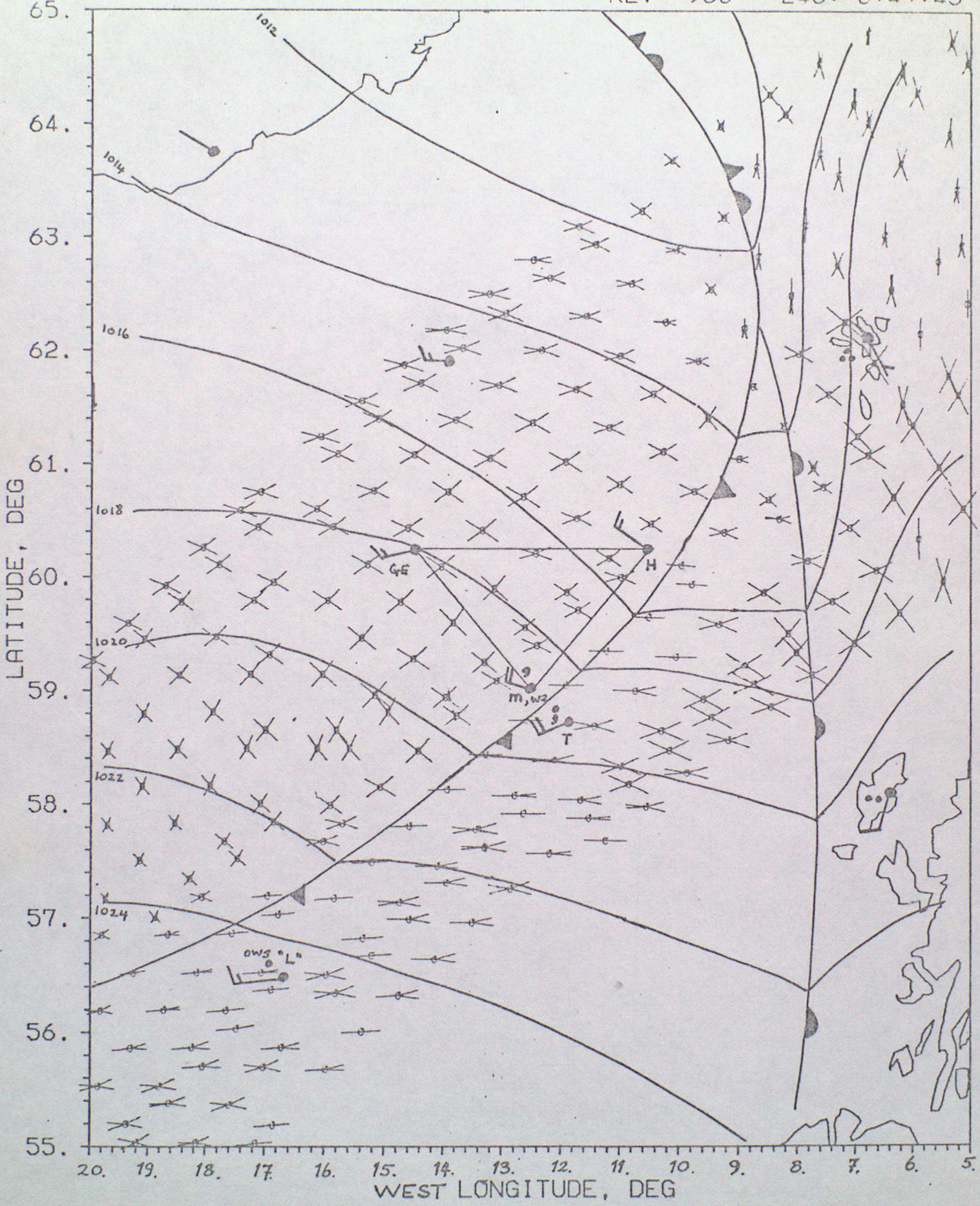

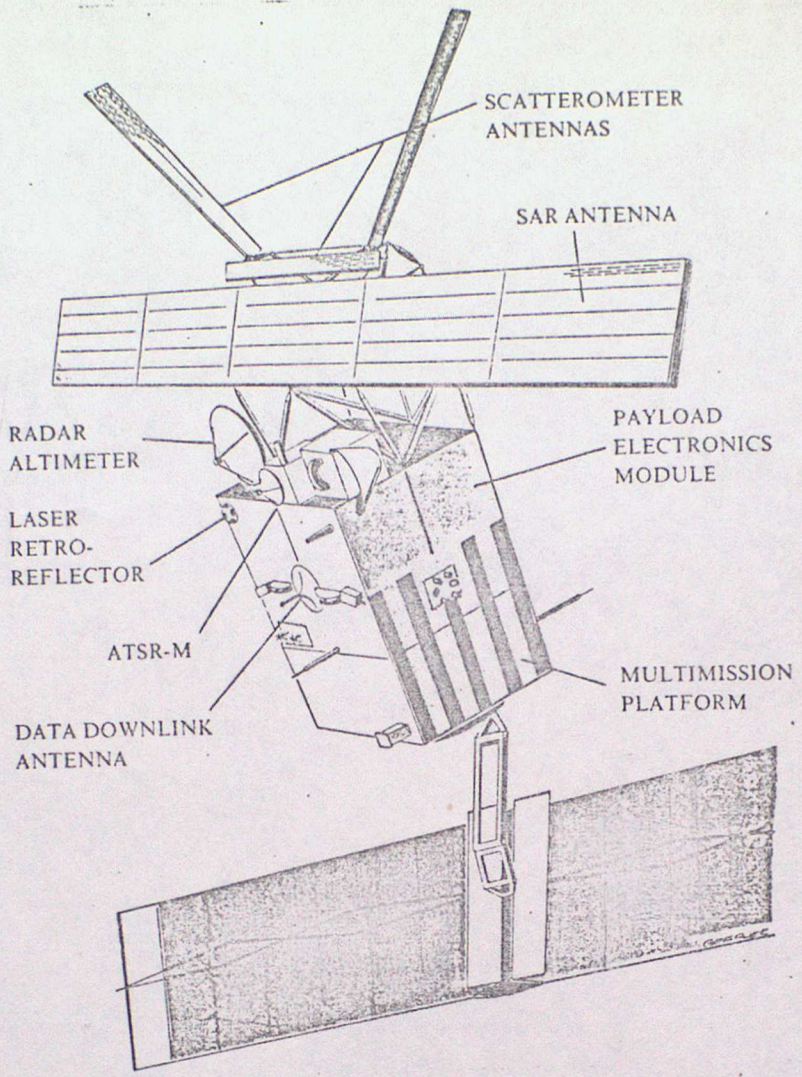

Figure 10. The ERS-1 satellite

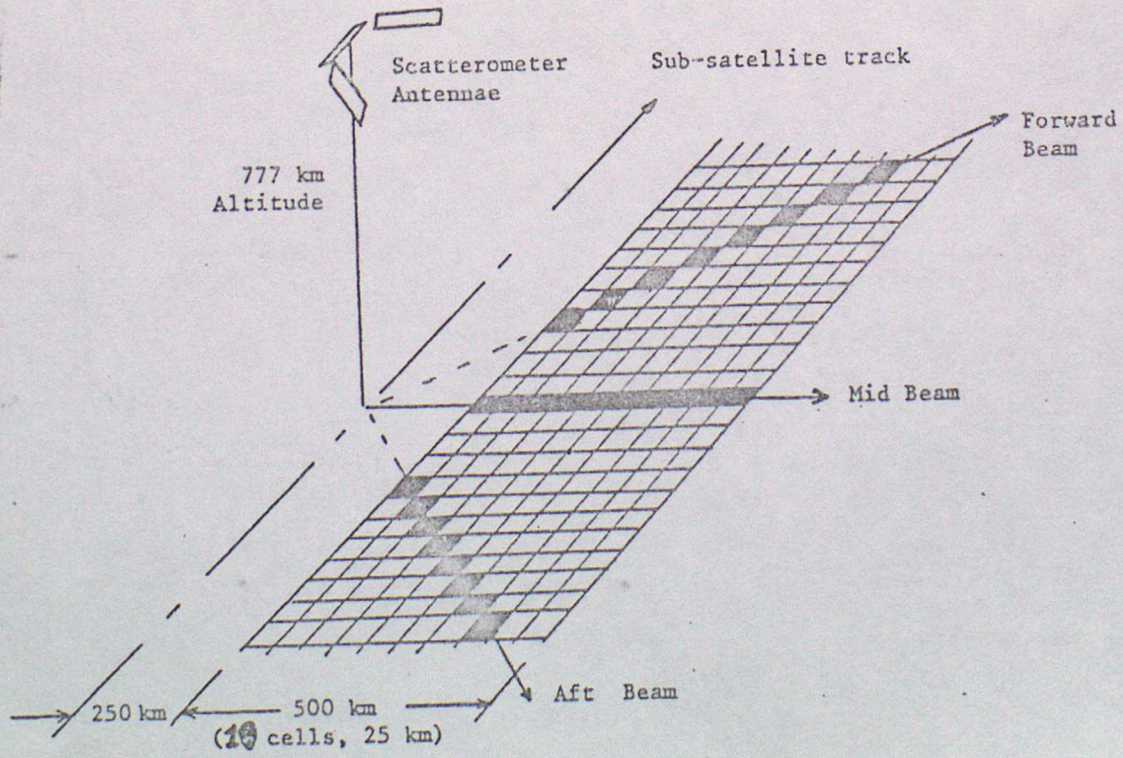

Figure 11. The AMI. Wind Scatterometer swath.

ERS-1 GROUND TRACK & WIND SCAT. SWATH FOR DAY 2
(MID BEAM POSITION EVERY MINUTE)

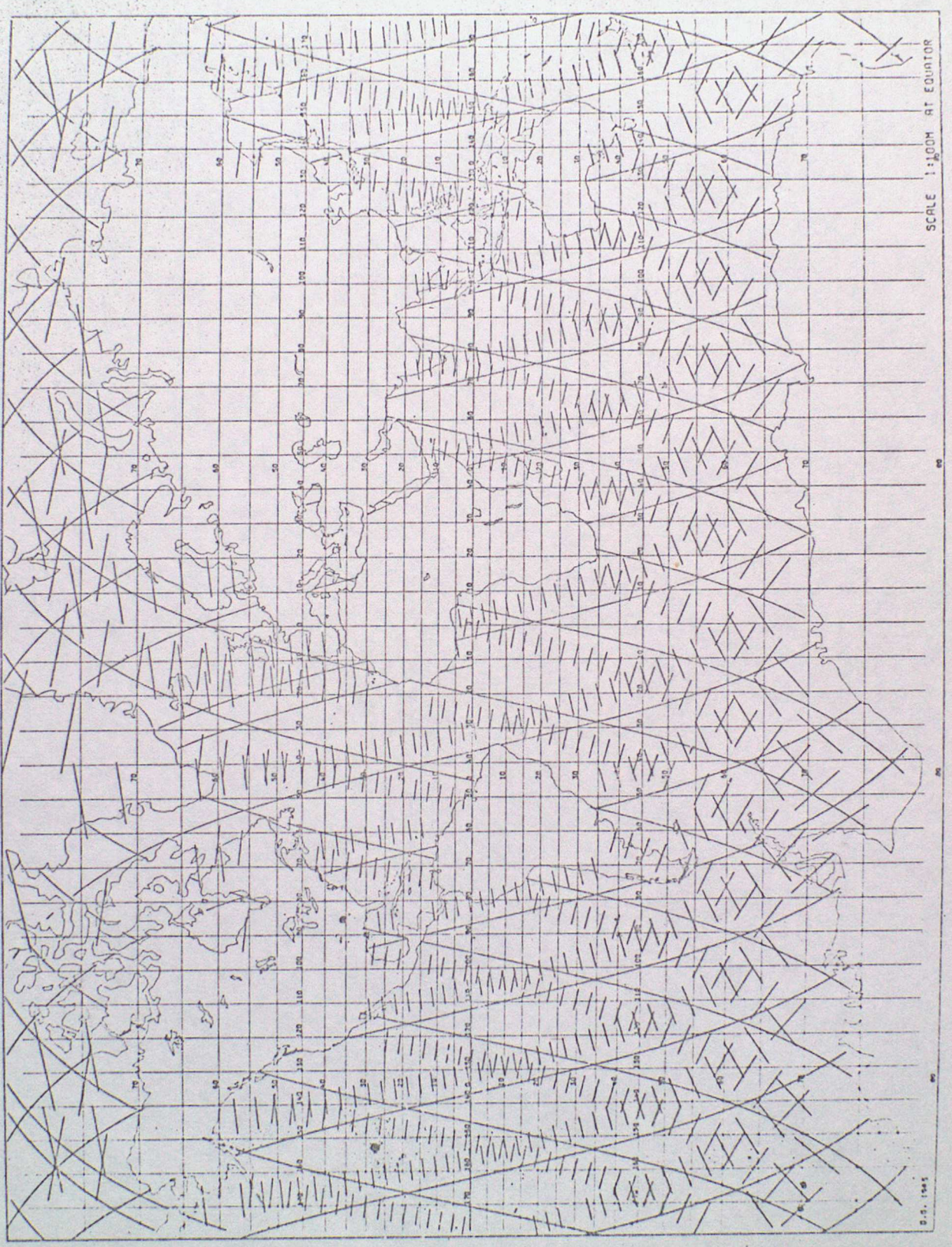

Figure 12 (a)

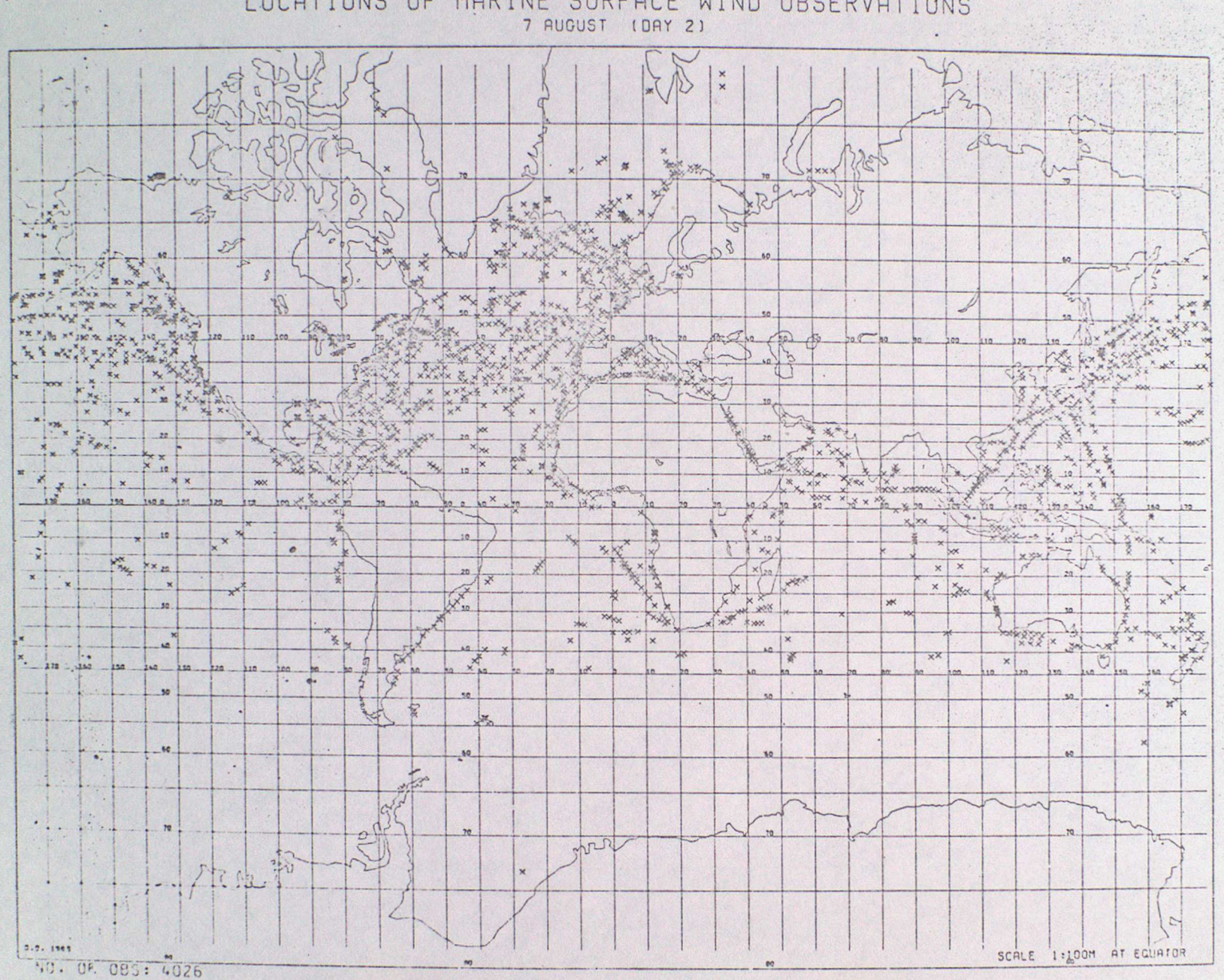
LOCATIONS OF MARINE SURFACE WIND OBSERVATIONS
7 AUGUST (DAY 2)
SCALE 1:100M AT EQUATOR
NO. OF OBS: 4026

Figure 12 (b).

The modification of orbit parameters can have a great impact on the coverages over a zone. In the case where statistical data or monitoring at a particular point is required, the coverage could be adapted. In the example below, coverages of the sub-satellite track is shown only for a part of the North sea.

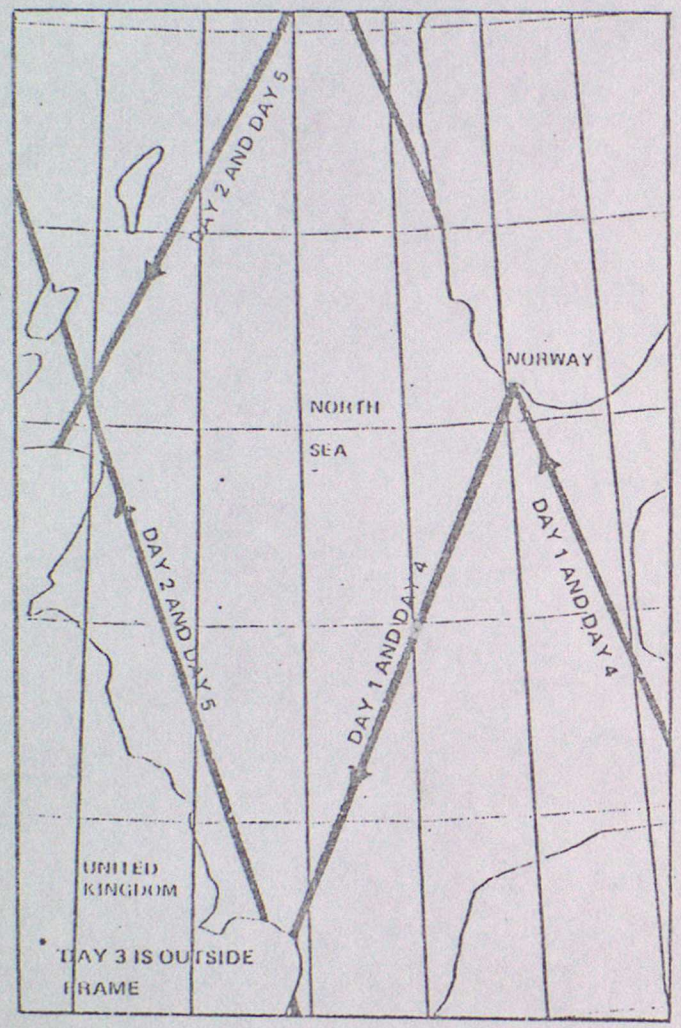

3 DAY CYCLE

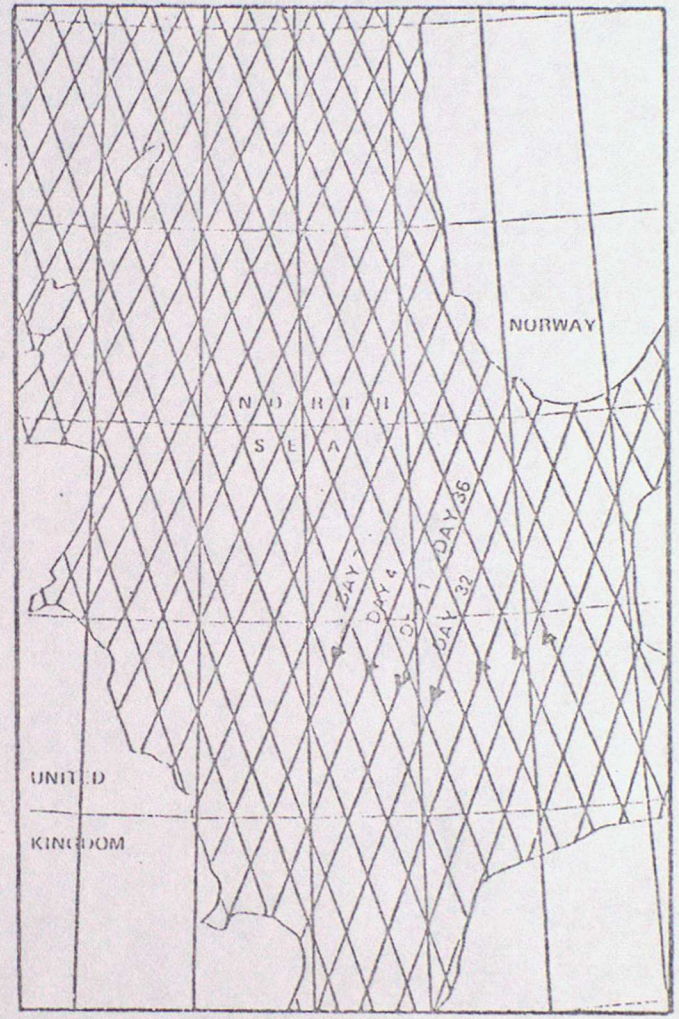

35 DAY CYCLE

Figure 13.